ministerie van verkeer en waterstaat

koninklijk nederlands meteorologisch instituut

Instability mechanisms in a barotropic atmosphere

R. J. Haarsma

Scientific reports WR-nr 89-01

wetenschappelijke rapporten WR-nr 89-01

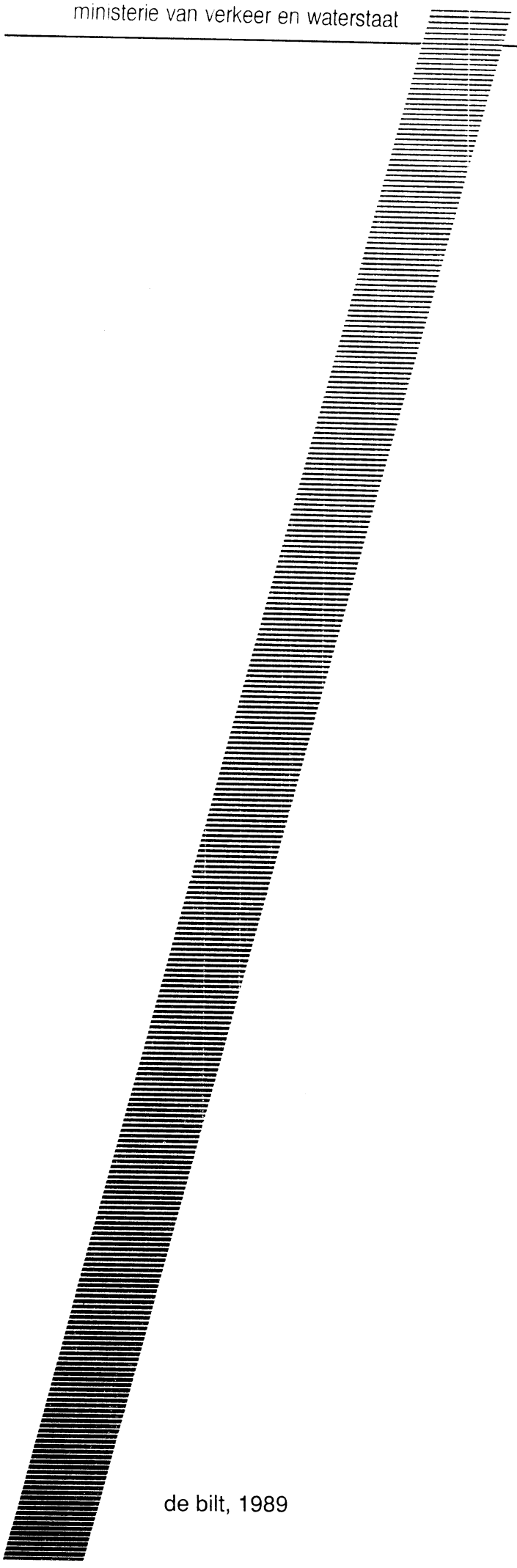

de bilt, 1989

de bilt 1989 publikatienummer: Scientific reports = wetenschappelijke rapporten ; WR-89-01 (DM)

postbus 201
3730 AE de bilt
wilhelminalaan 10
(0)30 - 206911
telex 47096

Dynamical Meteorology Department

Also published as a Ph.D.Thesis Free University (Vrije Universiteit) Amsterdam

U.D.C.: 551.511.12
551.511.32

ISSN: 0169-1651

ministerie van verkeer en waterstaat

koninklijk nederlands meteorologisch instituut

Instability mechanisms in a barotropic atmosphere

R. J. Haarsma

Scientific reports WR-nr 89-01

wetenschappelijke rapporten WR-nr 89-01

de bilt, 1989

KNMI

CONTENTS

CONTENTS (continued) Page

VOORWOORD

Ik wil hier graag iedereen bedanken die heeft meegeholpen bij de totstandkoming van dit proefschrift. Een aantal van hen wil ik hier speciaal noemen:

Mijn co-promotor Theo Opsteegh voor zijn stimulerende en kritische begeleiding; jouw steun en vertrouwen ook in moeilijke fases van het onderzoek zijn voor mij zeer belangrijk geweest;

mijn promotor Henk Tennekes voor het kritisch doorlezen van het manuscript en de begeleiding tijdens de voltooiing van dit onderzoek;

Cor Schuurmans voor de bereidheid om als referent op te treden;

Fons Baede voor de vrijheid die hij me gegeven heeft tijdens dit onderzoek;

Kees Kok voor de vele discussies, de gezelligheid en het verdragen van mijn "jo-jo"-stemmingen;

Alle andere leden en voormalige leden van de werkgroep Algemene Circulatie voor de open en collegiale sfeer waarin ik dit onderzoek heb kunnen doen;

Birgit Kok voor het nauwkeurige typewerk;

De studio en de drukkerij voor hun bijdrage aan de uiteindelijke vormgeving van dit proefschrift;

Tenslotte wil ik van alle anderen die mij geholpen en gestimuleerd hebben speciaal Madelien Bruins bedanken.

SAMENVATTING

Het weer aan het aardoppervlak hangt nauw samen met de luchtstromingen op ongeveer 10 km hoogte, boven in de troposfeer. Op die hoogte bevindt zich de straalstroom, die gekarakteriseerd wordt door sterke westenwinden, met snelheden in de orde van 50 m/s. Ligging en structuur van de straalstroom zijn in grote mate bepalend voor de ontwikkelling van weersystemen, zoals depressies en hogedruk gebieden. Tengevolge van oneffenheden in het aardoppervlak, veroorzaakt door de grote bergketens en de aanwezigheid van continenten en oceanen, vertoont de straalstroom grote slingeringen in noord- en zuidwaartse richting. Deze slingeringen worden planetaire golven genoemd. De planetaire golfstructuur vertoont grote dagelijkse variaties. Ook na middeling over een maand of seizoen vertoont de planetaire golfstructuur nog belangrijke afwijkingen van het klimatologische langjarige gemiddelde. Deze afwijkingen of anomaliën zijn van invloed op het algemene weerbeeld gedurende die periode; ze kunnen bijvoorbeeld de oorzaak zijn van een warmere en drogere zomer dan gebruikelijk.

Anomaliën in de planetaire golfstructuur kunnen veroorzaakt worden door afwijkende condities aan het aardoppervlak, zoals anomale zeewatertemperaturen, sneeuwbedekking en bodemvochtigheid. Recente studies hebben aangetoond dat er een verband bestaat tussen anomale zeewatertemperaturen in de tropen en de planetaire golfstructuur. Tijdens El-Niño jaren, wanneer in het tropische gedeelte van de Stille Oceaan grote temperatuurveranderingen optreden, is de atmosferische circulatie in de tropen volledig ontregeld. Langdurige droogtes en grote overstromingen door hevige regenval kunnen hier het gevolg van zijn. Anomale zeewatertemperaturen in de tropen zijn ook van invloed op de structuur van de planetaire golven op de gematigde breedten. Het effect is echter geringer.

Anomaliën in de planetaire golfstructuur kunnen ook het gevolg zijn van de wisselwerking tussen verschillende meteorologische verschijnselen. Het is niet alleen zo dat de planetaire golven de ontwikkeling van depressies en hogedrukgebieden bepalen, maar omgekeerd oefenen deze ook weer invloed uit op de planetaire golfstructuur. Deze wederzijdse beïnvloeding, ook wel interactie genaamd, tussen de verschillende meteorologische processen, variërend van de langste planetaire golf tot het kleinste werveltje, wordt beschreven door de niet-lineaire termen in de wiskundige vergelijkingen voor de atmosferische circulatie. Tengevolge van deze niet-lineaire inter-

actie vertoont de planetaire golfstructuur niet alleen sterke dagelijkse variaties, maar kunnen ook langdurige anomaliën optreden. Strenge winters of hete zomers hoeven dus niet noodzakelijk een uitwendige oorzaak te hebben, maar kunnen volledig het gevolg zijn van de interne variabiliteit van de atmosfeer.

De door de interne variabiliteit veroorzaakte anomaliën in de planetaire golfstructuur kunnen echter in het algemeen niet vooruit voorspeld worden. Tengevolge van de niet-lineaire termen zijn de wiskundige vergelijkingen, die het verloop van de atmosferische circulatie in de tijd beschrijven, zeer gevoelig voor de begincondities. Computermodellen hebben aangetoond dat kleine veranderingen in de begincirculatie na enkele dagen al grote verschillen in de berekende circulatie veroorzaken. Dit betekent dat het zinloos is om uitgaande van de circulatie op een bepaald tijdstip de circulatie voor een maand later te berekenen, omdat de kennis over de begincirculatie onvermijdelijk fouten bevat. Voor de atmosfeer bestaat er dus een eindige voorspelbaarheidshorizon, welke niet verlengd kan worden door de fouten in de begincondities kleiner te maken.

Deze voorspelbaarheidshorizon, in de orde van een dag of tien, is waarschijnlijk niet constant, maar afhankelijk van de toestand van de atmosfeer. Voor bepaalde circulaties in bepaalde gebieden is de gevoeligheid voor fouten in de begincondities wellicht kleiner. Recente studies laten zien dat de grootschalige tropische circulatie tijdens El-Niño jaren zich volgens bepaalde vaste patronen ontwikkelt en wellicht van te voren voorspeld kan worden. Andere mogelijke situaties met een langere voorspelbaarheidshorizon zijn bijvoorbeeld blokkades, wanneer de planetaire golfstructuur een rug boven West-Europa of de Rocky Mountains vertoont. In deze situatie wordt de doorkomst van oceaandepressies geblokkeerd en ontwikkelt zich een hogedrukgebied over het continent. Dit gaat in het algemeen met mooi weer gepaard. Blokkades kunnen soms wel een maand standhouden. Sluitende theoriën over blokkades ontbreken echter nog op dit moment.

Alhoewel gedurende de laatste decennia de kennis omtrent de dynamica van planetaire golven aanzienlijk is toegenomen, is het beeld nog verre van volledig. Met name het effect van de niet-lineaire termen op de dynamica van planetaire golven wordt nog slecht begrepen. Dit proefschrift poogt een bijdrage te leveren tot een beter begrip van de niet-lineaire dynamica van planetaire golven met tijdschalen die variëren van een paar weken tot een seizoen. Het proefschrift bestaat uit drie afzonderlijke artikelen.

In het eerste artikel wordt de stabiliteit van planetaire golven onderzocht. Wanneer de amplitude van een planetaire golf een kritische waarde overschrijdt, wordt de golf instabiel en begint te breken. Voor geïdealiseerde planetaire golven zijn de kritische waarden en het brekingsmechanisme onderzocht. Dit is gedaan voor de ondiepwatervergelijkingen. Deze vergelijkingen worden gekarakteriseerd door een dimensieloze parameter F, Lamb's parameter genaamd. Vaak wordt F = 0 gekozen, in welk geval de ondiepwatervergelijkingen reduceren tot de barotrope vorticiteitsvergelijking. We hebben er echter voor gekozen om F als een parameter te beschouwen en de stabiliteit van de planetaire golven als functie van F te onderzoeken. Het blijkt dat de stabiliteit van de planetaire golven sterk afhankelijk is van F. De kritische amplitude voor instabiliteit neemt af bij toenemende F. Hier tegenover staat dat ook de groeisnelheden van de verstoringen afnemen bij toenemende F. Een ander belangrijk verschijnsel is de aanwezigheid van een nieuw instabiliteitsmechanisme wanneer F groter dan nul is. Dit nieuwe instabiliteitsmechanisme, zelfinteractie genaamd, gebeurt via dyade interacties. Dit in tegenstelling tot het gebruikelijke instabiliteitsmechanisme dat via triade interacties verloopt. Onder bepaalde voorwaarden is het verval tengevolge van zelfinteractie even snel als het verval tengevolge van triade interacties.

In het tweede artikel is onderzocht wat de invloed is van zelfinteractie op het dynamische gedrag van een eenvoudig atmosferisch model. Voor dit model zijn de evenwichtsoplossingen bepaald. Het blijkt dat zelfinteractie de structuur van de evenwichtsoplossingen aanzienlijk kan wijzigen. Dit gebeurt echter alleen voor onrealistische waarden van de parameters. Of dit ook geldt voor de echte atmosfeer is op voorhand niet te zeggen, vanwege de vele vereenvoudigingen die in het model zijn aangebracht.

In het derde artikel is de anomale planetaire golfstructuur tijdens de El-Niño winter van 1982/83 gesimuleerd met een barotroop model. Voor dit model is de stationaire evenwichtsrespons bepaald van een anomale tropische forcering, welke geschat is uit data. In het bijzonder is gekeken naar de invloed van de niet-lineaire termen, welke afhankelijk is van de sterkte van de anomale forcering. Omdat deze slechts tot op een factor 2 nauwkeurig bekend is, hebben we de respons als functie daarvan bepaald. Voor zwakke forcering is de respons in goede benadering lineair. De structuur van de lineaire respons komt vrij goed overeen met de waargenomen anomale planetaire golfstructuur. Bij matige forcering verschilt de respons weinig met

de lineaire respons. Wanneer de sterkte van de forcering verder wordt verhoogd treden er op een gegeven moment bifurcaties op tengevolge van de niet-lineaire termen. Bij bifurcaties ondergaat het karakter van de oplossingen drastische wijzigingen bij een kleine verandering in de sterkte van de forcering. Na de bifurcaties is de overeenkomst met het waargenomen patroon minder. We moeten hieruit concluderen dat zelfs voor een sterke El-Nifo gebeurtenis als die van 1982/83 de niet-lineaire termen onbelangrijk zijn voor de structuur van de anomale planetaire golven tengevolge van een anomale tropische forcering.

Alle berekende evenwichtsoplossingen zijn instabiel. Het tijdsafhankelijke gedrag vertoont zowel periodiek, quasi-periodiek als chaotisch gedrag. Het chaotische gedrag wordt waargenomen na de saddle-node bifurcaties. Uit de tijdsintegraties blijkt dat de (instabiele) evenwichtsoplossingen van invloed zijn op het tijdsafhankelijke gedrag. Zelfs in het chaotische domein lijken de tijdsgemiddelde patronen en evenwichtspatronen sterk op elkaar.

Chapter I

GENERAL INTRODUCTION AND SUMMARY

1. Low-frequency variability of planetary waves

The weather as we experience it in daily life is strongly related to the air flow in the upper troposphere and lower stratosphere. At the middle latitudes this air flow is characterized by a relatively narrow band of strong westerly winds, with maxima in the order of 50 ms^{-1} at an altitude of about 10 km. The origin of this so-called jet stream is the difference between the incoming solar radiation at the pole and equator. Warm air from the tropics ascends and moves poleward. The mid-latitude regions where warm and cold air meet are called frontal zones. A strong westerly jet develops, which is caused by the temperature gradient across the front and the rotation of the earth. Inhomogeneities in the earth surface, like the mountain ridges and the land-sea thermal contrast, cause meanders in the westerly winds. These meanders, called planetary waves, have length scales in the order of the earth radius. Position and structure of these planetary waves determine the development of synoptic-scale weather systems like depressions and anti-cyclones.

An example of the planetary-scale structure of the atmosphere is shown in Fig. 1. It displays the climatological flow for January at 500 mb. The main features of this pattern are the two troughs located at the east coast of both continents. The strongest winds are found at these troughs, where the distance between the isolines is smallest.

The daily 500 mb maps are very different from the climatological ones. They display a much more wavy pattern, with large day-to-day variations, caused by synoptic-scale cyclones and anti-cyclones with typical length scales of about 1000 km. The synoptic-scale cyclones arise as a result of instabilities along the frontal zone that occur when the temperature difference exceeds a critical value. They transport warm and cold air north- and southward respectively, thereby reducing the temperature differences across the frontal zone. The synoptic-scale systems have life times of about a week and are responsible for the weather as we experience it from day to day. They start developing in the troughs east of both continents,

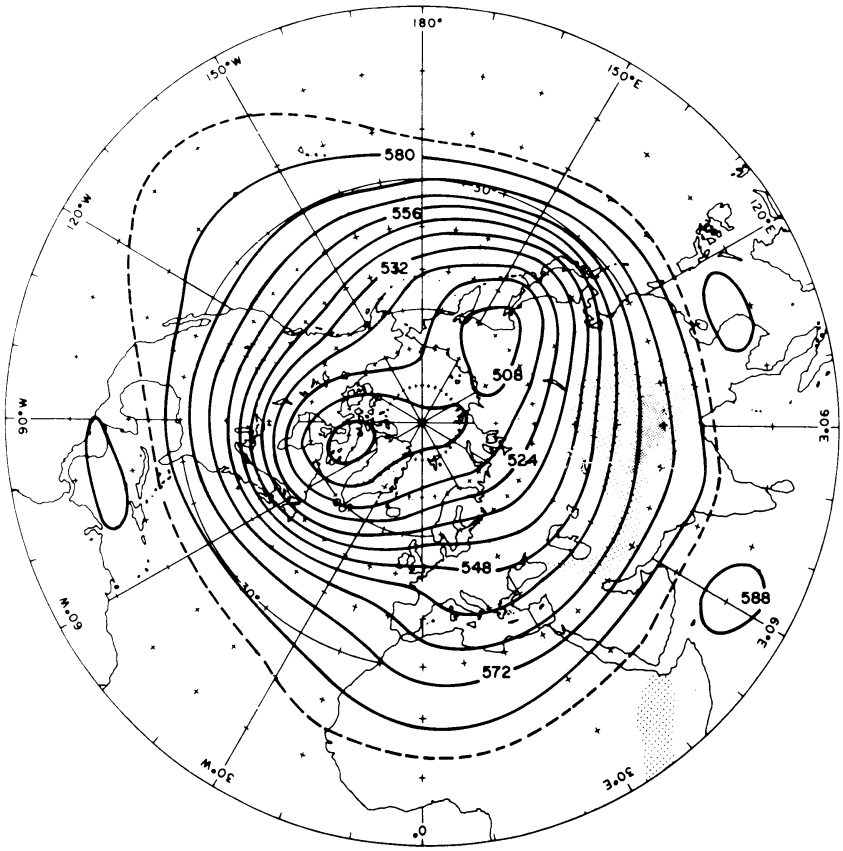

Fig. 1 Mean 500 mb contours in January. Northern Hemisphere. Heights shown in tens of geopotential meters.
(After Palmén and Newton, 1969)

where the wind speeds and related temperature differences are largest. They propagate toward the east across the oceans in the background flow provided by the planetary waves.

The planetary wave pattern not only varies from day to day, but also on longer time-scales of a month or a season. The longer time-scale variations in the planetary wave pattern determine the mean weather; for instance it may result in a warmer and drier summer than usual. This thesis deals with the possible causes of the low-frequency variations in the planetary wave pattern. Long-term forecasts of the planetary wave pattern for certain areas and periods may be possible if these causes are understood.

Low-frequency variations in the planetary wave pattern can be investigated by simulations with large computer models of the atmospheric circulation, called General Circulation Models (GCM's). In a GCM persistent deviations or anomalies of the planetary wave pattern have been generated as a result of persistent anomalies in the boundary conditions, like sea surface temperatures (SST), soil moisture, snow and sea-ice coverage, etc. These boundary conditions tend to vary on time scales of a month or longer and may thus influence the atmospheric circulation on long time scales. In many papers the importance of anomalous SST's for the anomalies in monthly or seasonal mean circulation was investigated. Simulations with GCM's (Rowntree, 1976; Geisler et al., 1985; Shukla and Wallace, 1983) showed that persistent sea surface temperature anomalies (SSTA's) in the tropical oceans generate anomalies in the global scale planetary wave pattern. From observational studies, the importance of SSTA's for the atmospheric circulation was already suggested by Namias (1969) and Bjerknes (1966), before the first experiments with GCM's.

The equations describing the atmospheric circulation are nonlinear, resulting in strong interactions between different scales of motion. Due to these nonlinearities, prolonged deviations of the climatological planetary wave pattern occur in a GCM even under constant boundary conditions. This means that a long hot summer does not necessarily need an external cause, but may be the sole result of the internal variability of the atmospheric system. The structure and frequency of the anomalies generated in a GCM under constant boundary conditions resemble those of the observed ones (Manabe and Hahn, 1981). These low-frequency fluctuations due to the internal variability, cannot be predicted ahead in general, because their occurrence depends sensitively on the initial conditions. This was first ob-

served by Lorenz (1969) using a simple model of the atmospheric circulation. Studies with more complicated models confirmed his findings. The consequence is that it is generally useless to try to make a detailed prediction of the atmospheric circulation for an extendend period of for instance a month by forward integration with a GCM, because the initial conditions inevitably contain small errors. For the atmospheric circulation there exist a prediction horizon, which cannot be pushed forward by reducing the initial errors. However, the prediction horizon is probably not a constant limit, but it may depend on the actual state of the atmosphere. It might be that the sensitivity to initial errors is less for certain circulation patterns and for certain geographical locations. Recent studies indicate that the large-scale tropical circulation during El-Niño events, when a large part of the tropical Pacific shows positive SSTA's, develops in a well behaved manner and may be predicted a long time ahead (Philander, 1983). Other possible circulation patterns with an extended prediction horizon are for instance blocking highs, when the planetary waves show a ridge over western Europe or the Rockies. In this situation, which may last for about a week to a month, the passage of cyclones, coming from the ocean, is blocked, resulting in the development of an anticyclone over the continent with usually fair weather.

Except for these circulation patterns we cannot predict the anomalies due to the internal variability and we have to confine ourselves to the ones caused by the anomalous boundary conditions.

Due to their complexity, GCM's do not provide much insight into the physical mechanisms that cause anomalies. We therefore return to simple models of the atmosphere, which, hopefully, still contain the essential physics needed to explain the observed anomalies. The observed long-term averaged planetary wave structure is approximately equivalent barotropic. The barotropic vorticity equation (BVE) may thus be a good approximation for the low-frequency behavior of planetary waves.

When studying the effects of anomalous boundary conditions, one frequently simplifies the BVE by neglecting the nonlinear quadratic terms among the perturbations of the climatological basic state. This approximation is justified because the amplitudes of seasonal or monthly mean anomalies are generally smaller than those of the climatological planetary waves. With the linear BVE Hoskins and Karoly (1981) showed that Rossby waves can transport energy from the tropics into the middle latitudes. It

was shown by Branstator (1985) and Held and Kang (1987) that the extratropical anomalies generated by GCM's in response to tropical SSTA's can be qualitatively simulated by BVE-models, that are linearized around the zonally varying climatological basic state of the GCM.

Internally generated low-frequency fluctuations are a result of nonlinear processes and need to be studied with the full nonlinear equations. Nonlinear effects in planetary-scale barotropic flows have frequently been studied to provide an explanation for the occurrence of blocking highs. With a simple model based on the BVE, containing only a few degrees of freedom, Charney and DeVore (1979) demonstrated the possibility for the existence of more than one quasi-stable steady state. The flow pattern of one of these steady states displays a wavy structure, resembling a blocked circulation, whereas the other one displays a more zonal structure corresponding with a normal circulation. They suggested that, in the atmosphere, transition from one quasi-stable steady state to another is accomplished by synoptic-scale cyclones. Indeed, for a baroclinic model that explicitly allows the formation of midlatitude synoptic-scale cyclones, Reinhold and Pierrehumbert (1982) demonstrated regime behavior, caused by the existence of multiple unstable steady states. Regime behavior is also observed in barotropic models possessing a larger number of degrees of freedom (Legras and Ghil, 1985). However, these studies do not provide a conclusive answer to the question whether observed long-lasting anomalies, and in particular blocking highs, indeed originate from multiple steady states. In a careful analysis Tung and Rosenthal (1985) showed that all these studies suffer from approximations which can be questioned. Regime behavior in these models disappears for more realistic parameter values. Studies with more sophisticated models are needed to answer the question whether or not multiple steady states are relevant for the low-frequency fluctuations in the atmosphere.

Kok and Opsteegh (1985) demonstrated that the statistical effect of the synoptic-scale transient eddies is large for the seasonal-mean circulation patterns despite the smallness of these terms in the time-averaged momentum balance. In simulating observed anomalies for the El-Niño event of 1982/83 they found that the statistical effect of transient eddies was most important in explaining the observed anomalies. Their study indicates that even for a strong El-Niño event as the one in 1982/83, the extratropical anomalies are mainly due to the internal dynamics.

Resonant amplification of a natural mode of oscillation as an explanation for observed anomalies has been suggested by several investigators. Simmons et al. (1983) demonstrated that the 300 mb climatological January flow is barotropically unstable. Linear stability analysis revealed a fastest growing perturbation which resembles the Pacific North America (PNA) teleconnection pattern. This pattern, consisting of a wave train with a low over the central Pacific, a high over the northern part of North America and a low over Florida, is a predominant anomaly pattern in the atmosphere. It was discovered from observational data by Wallace and Gutzler (1981). Simmons et al. (1983) demonstrated that this PNA pattern only needs to be triggered by a small forcing, but that it grows on the instability of the planetary-scale flow. Similar results were found by Frederiksen (1983) with a multilayer model. He showed that the structure of the fastest growing perturbation depends on the static stability parameter. The results of Geisler et al. (1985) with a GCM supported these results. Held and Kang (1987), using a slightly different basic state, did not find this behavior. Apparently the stability of planetary-scale flows is rather sensitive to small changes in the flow patterns.

Others (McWilliams, 1980; Verkley, 1984; Malguzzi and Malanotte-Rizzoli, 1984) have suggested the importance of nonlinear localized solutions of the unforced inviscid BVE for the explanation of observed anomalies, in particular blocking highs. Until now only a few nonlinear solutions of the BVE have been discovered analytically. However, from a numerical study Branstator and Opsteegh (1989), showed that solutions of the nonlinear BVE are abundant in phase space.

Although during the last decade substantial progress has been made in the understanding of the possible causes for low-frequency fluctuations in the planetary waves, the picture is still far from complete. As discussed above, it has recently become clear that barotropic processes may be important. This motivated further study of the dynamics of barotropic planetary waves. The present thesis consists of a collection of three separate papers on this subject.

2. Outline of this thesis

In the first paper (Chapter II) the stability of barotropic planetary waves is investigated. As mentioned before, studies by Simmons et al. (1983) and Frederiksen (1983) show that the climatological monthly mean flow is barotropically unstable and that the fastest growing perturbations might be relevant for the observed anomalies. These numerical studies, important as they are, do not provide much theoretical insight into the barotropic instability problem. Gill (1974) and Baines (1976) investigated for the BVE the stability properties of simple flow configurations. They found that the stability of a planetary wave can be described by considering only the most unstable triad. These triads, consisting of the planetary wave and two perturbations, become unstable when they are close to resonance, i.e. when the sum of the frequencies of the waves that form the triad is almost zero.

We have investigated the stability of planetary waves for the shallow-water equations (SWE) instead of the BVE. In the nondimensional SWE a single parameter $F = a^2\Omega^2/gH_e$ appears, called Lamb's parameter, in which a is the radius of the earth, Ω its angular velocity, g gravity and H_e the equivalent depth. In the past most investigators have simply chosen $F = 0$, which reduces the SWE to the BVE. We have decided to treat F as an unknown parameter. Hence we have investigated the sensitivity of our stability calculations to variations in F. The stability of planetary waves displays a sensitive dependence on F. The amplitude of the planetary wave for which instability occurs, decreases when F is increased. However, the growth rate and phase speed of the perturbations also decrease with increasing F. The instability of simple planetary scale flows occurs within the triad closest to resonance. In addition a second instability due to dyad interactions exist. This instability, called self-interaction, is caused by the fact that, in contrast to the BVE ($F = 0$), for $F > 0$ the normal modes of the SWE (Hough functions) are no longer exact solutions of the nonlinear SWE and will naturally decay. In the case of self-resonance the decay is rapid and comparable to the decay rates caused by barotropic instability. Outside the area of self-resonance, the decay is slow and the Hough functions can be considered as approximate solutions of the full nonlinear SWE.

The effect of self-interaction on the bifurcation diagram of a low-order model based on the SWE is investigated in the second paper

(Chapter III). Charney and DeVore (1979) demonstrated for a low-order model the possibility of saddle-node bifurcations due to topographic instability. Others (Charney and Straus, 1980; Legras and Ghil, 1985) investigated the effect of barotropic and baroclinic instability. For the model we investigated, we found that self-interaction generates saddle-node as well as Hopf bifurcations. Moreover self-interaction significantly affects the steady-state curve originating from topographic instability. This occurs only for large values of the forcing. Whether for the real atmosphere self-interaction is important remains unclear, because of the many simplifications made in this study.

In the third paper (Chapter IV) we analyze the effect that the nonlinear terms have on the structure and strength of extratropical anomalies that are excited by anomalous tropical forcing. Studies by Lau and Lim (1984), Sardeshmukh and Hoskins (1985), Kang and Held (1986), and Hendon (1986) all show that the nonlinear response to tropical forcing is in qualitative agreement with the predictions of linear theory. In these studies the effect of the nonlinearities is to modify the structure and amplitude of the stationary waves, whereas the positions of highs and lows remain relatively unaffected. The nonlinear response is computed by performing time integrations. In addition to this we have computed the nonlinear steady-state response of a barotropic model based on the BVE to anomalous tropical divergence forcing. This forcing was estimated from the anomalous observed outgoing long-wave radiation during the El-Niño winter of 1982/83. Because the amplitude of this forcing may be wrong up to a factor of two, we computed the steady states as a function of the strength of the anomalous forcing. For weak forcing the response is approximately linear. For stronger forcing the nonlinear terms become increasingly important. The linear response compares well with the observed anomalies. For moderate strength of the forcing, the structure of the response displays only minor changes compared to the linear response. Further increment of the forcing causes saddle-node bifurcations resulting in multiple steady states. Due to the bifurcations significant changes occur in the structure of the response pattern. As a result, the agreement with the observed anomalies decreases. From this we conclude that the atmospheric response to even a very strong El-Niño event like the one in 1982/83 is approximately linear. In accordance with other studies (Sardeshmukh and Held, 1984; Kang and Held, 1986; and Hendon, 1986) the main effect of the nonlinearities is

to modify the structure and amplitude of the planetary waves, with relatively small changes in the position of the pressure cells.

All computed steady states are unstable. Time integrations display periodic, quasi-periodic as well as chaotic behavior. Chaotic behavior is observed after the saddle-node bifurcations. This chaotic behavior is still governed by the (unstable) steady states. Even in the chaotic domain the time-mean patterns resemble the response patterns of the computed steady states.

3. References

Baines, P.G., 1976: The stability of planetary waves on a sphere. J. Fluid. Mech., 73, 193-213.

Bjerknes, J., 1966: A possible response of the atmospheric Hadley circulation to the equatorial anomalies of ocean temperature. Tellus, 18, 820-829.

Branstator, G., 1985: Analysis of general circulation model sea-surface temperature anomaly simulations using a linear model. J. Atmos. Sci., 42, 2225-2254.

Branstator, G., and J.D. Opsteegh, 1989: Free solutions of the barotropic vorticity equation. Submitted to J. Atmos. Sci.

Charney, J.G. and J.G. DeVore, 1979: Multiple flow equilibria in the atmosphere and blocking. J. Atmos. Sci., 36, 1205-1216.

Charney, J.G. and D.M. Straus, 1980: Form-drag instability, multiple equilibria and propagating planetary waves in baroclinic, orographically forced planetary wave systems. J. Atmos. Sci., 37, 1157-1176.

Frederiksen, J.S., 1983: A unified three-dimensional instability theory of the onset of blocking and cyclogenesis. II: Teleconnection patterns. J. Atmos. Sci., 40, 2593-2609.

Geisler, J.E., M.L. Blackmon, G.T. Bates and S. Munoz, 1985: Sensitivity of January climate response to the magnitude and position of equatorial Pacific sea surface temperature anomalies. J. Atmos. Sci., 42, 1037-1049.

Gill, A.E., 1974: The stability of planetary waves. Geophys. Fluid. Dyn., 6, 29-47.

Held, I.M. and I.-S. Kang, 1987: Barotropic models of the extratropical response to El-Niño. J. Atmos. Sci., 44, 3576-3586.

Hendon, H.H., 1986: The time-mean flow and variability in a nonlinear model of the atmosphere with tropical diabatic forcing. J. Atmos. Sci., 43, 72-88.

Hoskins, B.J. and D. Karoly, 1981: The steady linear response of a spherical atmosphere to thermal and orographic forcing. J. Atmos. Sci., 38, 1179-1196.

Kang, I.-S. and I.M. Held, 1986: Linear and nonlinear models of stationary eddies in the upper troposphere during Northern summer. J. Atmos. Sci., 43, 3045-3057.

Kok, C.J. and J.D. Opsteegh, 1985: Possible causes of anomalies in seasonal mean circulation patterns during the 1982/83 El-Niño event. J. Atmos. Sci., 42, 677-694.

Lau, K.M. and H. Lim, 1984: On the dynamics of equatorial forcing of climate teleconnection. J. Atmos. Sci., 41, 161-176.

Legras, B. and M. Ghil, 1985: Persistent anomalies, blocking and variations in atmospheric predictability. J. Atmos. Sci., 42, 433-471.

Lorenz, E.N., 1969: The predictability of a flow which possesses many scales of motion. Tellus, 21, 289-307.

Malguzzi, P. and P. Malanotte-Rizzoli, 1984: Nonlinear stationary Rossby waves on nonuniform zonal winds and atmospheric blocking. Part I: The analytical theory. J. Atmos. Sci., 41, 2620-2628.

Manabe, S., and D.G. Hahn, 1981: Simulation of atmospheric variability. Mon. Wea. Rev., 109, 2260-2280.

McWilliams, J.C., 1980: An application of equivalent modons to atmospheric blocking. Dyn. Atmos. Oceans, 5, 43-66.

Namias, J., 1969: Seasonal interaction between the North Pacific ocean and the atmosphere during the 1960's. Mon. Wea. Rev., 97, 173-192.

Palmén, E. and C.W. Newton, 1969: Atmospheric circulation systems. Academic Press, New York.

Philander, S.G.H., 1983: El Niño Southern Oscillation phenomena. Nature, 302, 295-301.

Reinhold, B.B. and R.T. Pierrehumbert, 1982: Dynamics of weather regimes: Quasi-stationary waves and blocking. Mon. Wea. Rev., 110, 1105-1145.

Rowntree, P.R., 1976: Response of the atmosphere to a tropical Atlantic ocean temperature anomaly. Quart. J. Roy. Meteor. Soc., 102, 607-625.

Sardeshmukh, P.D. and I.M. Held, 1984: The vorticity balance in the upper atmosphere of a general circulation model. J. Atmos. Sci., 41, 768-778.

Sardesmukh, P.D. and B.J. Hoskins, 1985: Vorticity balances in the tropics during the 1982-83 ENSO event. Quart. J. Roy. Meteor. Soc., 111, 261-287.

Shukla, J. and J.M. Wallace, 1983: Numerical simulation of the atmospheric response to equatorial Pacific sea-surface temperature anomalies. J. Atmos. Sci., 40, 1613-1630.

Simmons, A.J., J.M. Wallace and G.W. Branstator, 1983: Barotropic wave propagation and instability and teleconnection patterns. J. Atmos. Sci., 40, 1363-1392.

Tung, K.K., and A.J. Rosenthal, 1985: Theories of multiple equilibria. A critical reaximination. Part I: Barotropic models. J. Atmos. Sci., 42, 2804-2819.

Verkley, W.T.M., 1984: The construction of barotropic modons on a sphere. J. Atmos. Sci., 41, 2492-2504.

Wallace, J.M. and D.S. Gutzler, 1981: Teleconnections in the geopotential height field during the Northern Hemisphere winter. Mon. Wea. Rev., 109, 784-812.

Chapter II

BAROTROPIC INSTABILITY OF PLANETARY-SCALE FLOWS*

Abstract

The relevance of barotropic instability for the observed low-frequency variability in the atmosphere is investigated. The stability properties of the shallow-water equations on a sphere are computed for small values of Lamb's parameter ($F = a^2\Omega^2/gH_e$) where a is the earth's radius, Ω its angular velocity, g gravity and H_e the equivalent depth.

For small values of F these equations describe the horizontal structure of external and deep internal modes that are basically barotropic in the troposphere.

The stability of simple zonal flows, as well as free and forced planetary Rossby waves has been computed as a function of F. This is done numerically using a hemispheric spectral model with a T13 truncation. For F = 0 we have tried to interpret the numerical results by analytically computing the stability properties of the flow when only one triad is considered. The results show that for increasing F the critical amplitudes for instability decrease slightly, but in the area of instability both growth rate and frequency of the perturbations decrease with increasing F. The horizontal structure of the perturbations changes only slightly. In most cases the instability process occurs within one triad which is the triad closest to resonance. An analysis in terms of unstable triads seems equally relevant for zonal and for nonzonal flows. The stability properties of the observed 400 mb Northern Hemisphere winter climatological flow show the same dependence on F as found for simple flow patterns: both growth rate and frequency of the perturbations decrease for increasing F.

* Published in Journal of Atmospheric Sciences, 1988, 45, 2789-3016, with J.D. Opsteegh as co-author

1. Introduction

Since the studies by Eady (1949) and Charney (1947) on baroclinic instability, the barotropic instability mechanism has long been considered of minor relevance for the interpretation of observed flow patterns in the atmosphere. The theory for the appearance and growth of the so-called weather systems was completely based on the baroclinic instability mechanism. Both structure and growth rate of observed weather systems could be explained by linking them to the most rapidly growing perturbations of the baroclinically unstable quasi-stationary planetary scales of motion (Frederiksen, 1983a).

This does not mean that the usual weather systems are the only type of perturbations that grow on the energy of the background flow. It may well be that less rapidly growing modes emerge as well, but that they are, in general, obscured by the rapidly growing high-frequency eddies. If these slowly growing perturbations have low phase speeds, we can make them visible by applying a filtering technique to suppress the high frequencies. Indeed, on monthly or seasonal mean maps, anomaly patterns appear with a larger spatial scale. These perturbations are often called teleconnection patterns (Wallace and Gutzler, 1981). They are sometimes linked to local anomalies in tropical sea surface temperatures (SST) (Horel and Wallace, 1981). However, Simmons et al. (1983) and Frederiksen (1983b) showed that these patterns can be interpreted as growing modes of a barotropically unstable planetary scale flow. Therefore, for the explanation of atmospheric variability on longer time scales, the barotropic instability mechanism may have some relevance. Numerical studies on barotropic instability of complex observed flow configurations like the afore mentioned ones -important as they are- do not provide much theoretical insight into the barotropic instability problem.

The simplest equations appropriate to study the barotropic instability mechanism are the shallow water equations (SWE). The dynamical properties of solutions of the unforced inviscid SWE on a rotating sphere are determined by a single nondimensional parameter $F = a^2\Omega^2/gH_e$, called Lamb's parameter, where a is the earth's radius, Ω its angular velocity, g gravity and H_e the mean equivalent depth. For $F = 0$ the SWE reduce to the barotropic vorticity equation (BVE), whereas the limit $F \to \infty$ corresponds to the equatorial beta-plane approximation (Longuet-Higgins, 1968).

In reality, the atmosphere is a stratified fluid, which, in general, cannot be described by the equations for a homogeneous fluid. Only when nonlinear advection can be neglected, can separate equations for the vertical and horizontal structure of a stratified flow be derived. The horizontal structure is then described by the linear SWE. In these equations, a separation constant $c_e = \sqrt{gH_e}$ appears. When the advection terms cannot be neglected, or when they appear in linearized form, the use of the SWE cannot be justified a priori. As we are only interested in instabilities due to horizontal shear of the velocity field, we nevertheless feel that a study of the stability properties of the SWE has some relevance for barotropic instability in the atmosphere. In using these equations we are faced with the problem of making a choice for the equivalent depth. In the past most investigators have simply chosen $H_e = \infty$, which reduces the SWE to the BVE. We have decided to treat H_e as an unknown parameter. Hence, we will investigate the sensitivity of our stability calculations to variations in H_e and thus in Lamb's parameter F.

For the BVE (F = 0), Kuo (1949) demonstrated that barotropic instability of zonal flows is associated with the existence of inflection points where the gradient of absolute vorticity vanishes. Recently Ripa (1983a) generalized these results by demonstrating that for $F > 0$ a necessary condition for instability of a zonal flow is the vanishing of the absolute potential vorticity gradient somewhere in the fluid.

Lorenz (1972) suggested the importance of barotropic instability for planetary waves. For the BVE on a finite beta-plane with cyclic boundary conditions he demonstrated that free planetary waves become unstable when they exceed a critical amplitude which depends on wavenumber. For an infinite beta-plane, Gill (1974) showed that planetary waves are always unstable, due to the existence of resonant triads. On a spherical domain, most free planetary waves are neutrally stable below a certain critical amplitude, because, as a consequence of the cyclic boundary conditions, resonant triads do not exist in general (Baines, 1976). The importance of barotropic instability for the conversion of eddy kinetic energy to zonal kinetic energy has been investigated by Hoskins (1973). He found that growing perturbations only contain zonal flow components if the total wavenumber of the planetary waves is larger than 5. Baines (1976) pointed out that triad interactions among waves are more important than the wave zonal flow interactions studied by Hoskins.

The barotropic instability of planetary waves for the equatorial beta-plane ($F \to \infty$) has recently been analyzed in a series of papers by Ripa (1981, 1982, 1983bc) and Boyd (1983ab). In this case the normal modes are no longer exact solutions of the full nonlinear SWE and consequently a normal mode generates a harmonic by self-interaction. When the harmonic is at resonance with the primary wave, the decay due to self-interaction is comparable to the decay time scale for barotropic instability. In the case of self-resonance, the initial decay of the waves can be described by considering a two component system for the dyad interactions between the primary wave and its harmonic (Boyd, 1983a,b). Outside the domain of self-resonance, the decay time scale due to self-interaction becomes very large.

Lim and Chang (1983) argued that teleconnection patterns, with their barotropic structure in the troposphere, are not necessarily external modes but may equally well be considered large equivalent-depth internal modes. They studied the energy propagation properties of these deep internal modes and found that energy propagation is significantly affected by the choice of the equivalent depth. This may also be true for the barotropic instability problem. Simmons et al. (1983) used the BVE to study the teleconnection problem; i.e., they only considered instability of the external modes.

In this paper we study barotropic instability of observed atmospheric flow configurations for values of F representing the external and the deep internal modes. In order to better understand the results we start by studying the stability of very simple flow configurations. We have numerically computed the stability properties of simple zonal flows as well as free and forced planetary Rossby waves as a function of F. This is done using a hemispheric model with triangular truncation T13. For $F = 0$ we have also studied the stability of these flow patterns analytically by assuming that the instability process occurs within one triad. Comparing the results it is found that the instability of the gravest rotational modes for physically relevant growth rates of the perturbations can be described by considering a single triad.

Sections 2 and 3 of this paper deal with the basic equations, Lamb's parameter, and the description of the model. Section 4 is devoted to the stability of simple zonal flows, while sections 5 and 6 analyze the stability of free modes and forced stationary waves, respectively, and also discuss the consequences of self-interaction. In section 7 we will present the results for the climatological winter 400 mb flow. A discussion of the results will complete this paper.

2. The shallow-water equations

In nondimensional form the shallow-water equations on a rotating sphere may be written

$$\frac{\partial \zeta}{\partial t} = -\vec{v}.\nabla(\zeta + f) - (\zeta + f)D, \tag{1a}$$

$$\frac{\partial D}{\partial t} = -\nabla^2(\phi + \frac{\vec{v}.\vec{v}}{2}) - \nabla.[\vec{k}x\vec{v}(\zeta + f)] \tag{1b}$$

$$\frac{\partial \phi}{\partial t} = -\vec{v}.\nabla\phi - \phi D - \frac{D}{F}. \tag{1c}$$

where ζ, D and ϕ are the relative vorticity, horizontal divergence and perturbation geopotential respectively; f is the planetary vorticity; $\vec{v}$ is the horizontal velocity and $\vec{k}$ is the vertical unit vector.

Nondimensional variables are defined as follows:

$$\zeta = \zeta^*/\Omega;\ D = D^*/\Omega;\ \phi = \phi^*/a^2\Omega^2;\ t = t^*\Omega;\ f = f^*/\Omega.$$

where a and Ω are the radius and angular velocity of the earth, respectively, and the asterisks denote the dimensional variables.

The only nondimensional parameter in (1) is Lamb's parameter

$$F = \frac{a^2\Omega^2}{gH_e}.$$

The normal modes of the linear SWE are the Hough functions whose structure and phase speed depend on F. They consist of two types of waves with quite different properties: (a) east- and westward propagating gravity waves, and (b) westward propagating rotational waves of the Rossby-Haurwitz type (Kasahara, 1976).

Before proceeding, we will briefly discuss the SWE and their normal modes in the limit of small and large F. In the limit $F \to 0$ the phase speed and the structure of the rotational modes become equal to those of the normal modes of the BVE which are spherical harmonics. This can be seen from (1). For finite perturbations of the geopotential, the divergence D

approaches zero if $F \to 0$ and (1) reduce to

$$\frac{\partial \zeta}{\partial t} = - \vec{v}_\psi . \nabla(\zeta + f), \tag{2a}$$

$$0 = -\nabla^2(\phi + \frac{\vec{v}_\psi . \vec{v}_\psi}{2}) - \nabla . [\vec{k} x \vec{v}_\psi (\zeta + f)], \tag{2b}$$

$$\frac{\partial \phi}{\partial t} = - \vec{v}_\psi . \nabla \phi - \frac{D}{F} , \tag{2c}$$

where $\vec{v}_\psi = \vec{k} x \nabla \psi$ is the nondivergent velocity in which ψ is the stream function.

Equation (2a) is the BVE, which is decoupled from the non-linear balance equation (2b) and the equation for the geopotential (2c).

For large F, the energy of the normal modes is concentrated near the equator (Longuet-Higgins, 1968). Therefore, in the limit for $F \to \infty$ the SWE can be approximated to first order by the equations for the equatorial β-plane, for which the normal modes have been calculated by Matsuno (1966).

The dependence on F of structure and phase speed of the normal modes of the SWE has been investigated by Longuet-Higgins (1968).

Using the integral constraints for enstrophy and kinetic energy, Fjørtoft (1953) demonstrated that for $F = 0$ the (energy-weighted) average wavenumber squared is conserved. Combining Fjørtoft's theorem and the conservation of angular momentum, the stability of planetary waves with $n \leq 2$ can be ensured (Baines, 1976). Ripa (1982) showed by generalization of Fjørtoft's theorem that for $F\phi \ll 1$ this result is still valid. However, for $F\phi \sim O(1)$, no general statement about the stability of planetary waves can be made.

3. Numerical stability analysis

The stability of planetary scale flows is investigated by deriving the perturbation equations and next linearizing these equations around the basic flow.

The perturbations are expanded in spherical harmonics, e.g.,

$$\zeta(\lambda,\mu,t) = \sum_{m,n} \zeta_n^m(t) Y_n^m(\lambda,\mu) = \sum_{m,n} \zeta_n^m(t) P_n^m(\mu) e^{im\lambda} \qquad (3)$$

in which $Y_n^m(\lambda,\mu)$ are the spherical harmonics and $P_n^m(\mu)$ the associated Legendre polynomials defined by

$$P_n^m(\mu) = \left[\left(\frac{2n+1}{2}\right)\frac{(n-m)!}{(n+m)!}\right]^{\frac{1}{2}} \frac{(1-\mu^2)^{\frac{1}{2}m}}{2^n n!} \frac{d^{n+m}}{d\mu^{n+m}}(\mu^2-1)^n. \qquad (4)$$

Here λ and θ are longitude and latitude respectively and $\mu = \sin\theta$. After projecting the linearized perturbation equations on Y_n^m, we get an infinite set of three ordinary linear differential equations for the coefficients ζ_n^m, D_n^m and ϕ_n^m. This infinite set has been truncated to a T13 truncation, where we have retained only the antisymmetric components in the vorticity and symmetric components in the divergence and geopotential. This results in perturbations that have no cross equatorial flow. The coupling integrals appearing in the linearized perturbation equations have been computed numerically using the transform method (Bourke, 1972). Substituting perturbations whose time dependence is of the form $e^{i\omega t}$ we arrive at the eigenvalue problem. Eigenvalues with a negative imaginary part correspond with growing perturbations.

If we linearize around a state of rest, the eigenvectors are the normal modes of the truncated system. As an example, Fig. 1 displays for zonal wavenumber 2, the vorticity and divergence pattern of the gravest rotational mode for three different values of Lamb's parameter, i.e., F = 0.275, 2.75 and 27.5. The concentration of energy towards the equator for increasing values of Lamb's parameter is clearly seen. For F = 0.275, the vorticity structure is almost identical to the structure of the spherical harmonic $Y_3^2(\lambda,\mu)$, which is a normal mode for F = 0, while for F = 27.5 the absolute maximum of the vorticity is displaced about 30° towards the equator.

The frequencies of all modes decrease for increasing values of Lamb's parameter. For F approaching zero, the frequency of the rotational modes approaches the frequency of the normal modes of the BVE.

Because we expand the variables in spherical harmonics, which are not the normal modes of the SWE except for F = 0, any truncation distorts the

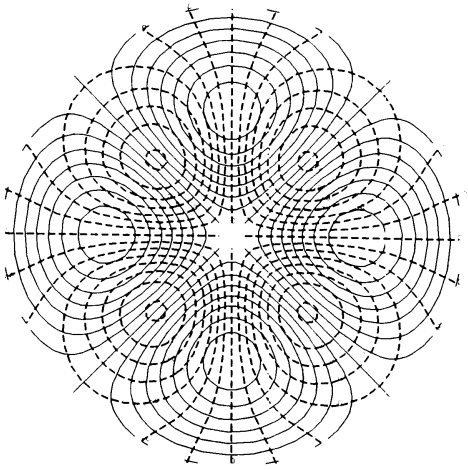

a
F = 0.275

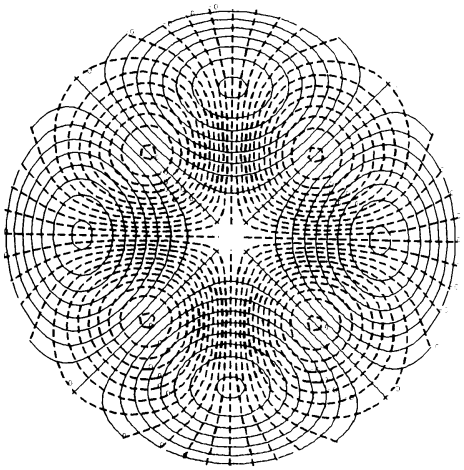

b
F = 2.75

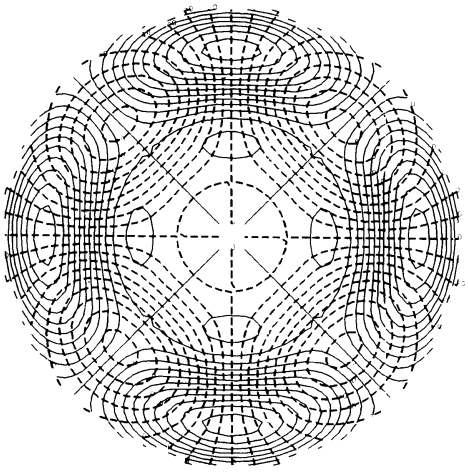

c
F = 27.5

Fig. 1. Stereographic plots of the vorticity and divergence patterns of the gravest rotational mode with zonal wave numer 2 for three different values of F.
Solid line: relative vorticity
Dashed line: divergence
a: F = 0.275; b: F = 2.75; c: F = 27.5

structure and frequency of the normal modes of the SWE. In order to see to what extent the modes of the T13 truncation are different from the Hough functions, we have compared them with the modes calculated by Longuet-Higgins (1968). The eigenvalues of the modes calculated by Longuet-Higgins are correct within an error margin of 0.01%.

The gravest modes of the T13 truncation are virtually the same as the Hough functions for all values of F. For large F the modes at the edge of the truncation show distortion. For instance the difference in phase speed between the (5,13) rotational mode of the T13 truncation and the same mode calculated by Longuet-Higgins for F = 27.5 is 20%.

4. Zonal flow instability

4.1 Sufficient conditions for stability

Ripa (1983a) derived sufficient conditions for the stability of a barotropic zonal flow u in geostrophic balance. In nondimensional form these conditions may be formulated as follows:

If there exists any value of α such that

$$(\alpha\cos\theta - u)\,\frac{\partial}{\partial\theta}\left(\frac{\zeta + f}{1 + \phi F}\right) \geq 0, \tag{5a}$$

and

$$(\alpha\cos\theta - u)^2 \leq \left(\frac{1}{F} + \phi\right), \tag{5b}$$

then the flow $u(\theta)$ is stable.

The choice of u as a function of θ is restricted by the requirement that $1 + \phi F > 0$. By choosing $\alpha = \max(u/\cos\theta)$ or $\alpha = \min(u/\cos\theta)$ the following weaker conditions for the stability of the zonal flow can be found:

$$\frac{\partial}{\partial\theta}\left(\frac{\zeta + f}{1 + \phi F}\right) \text{ does not change sign,} \tag{6a}$$

and

$$\max\left(\frac{u}{\cos\theta}\right) - \min\left(\frac{u}{\cos\theta}\right) \leq \min\left\{\frac{\left(\frac{1}{F} + \phi\right)^{1/2}}{\cos\theta}\right\} \tag{6b}$$

From these criteria we can derive the limiting forms for the nondivergent BVE ($F = 0$) and for the equatorial β-plane equations ($F \to \infty$).

In the limit $F = 0$ condition, (6b) is always satisfied, while condition (6a) reduces to

$$\frac{\partial}{\partial\theta}(\zeta + f) \text{ does not change sign.} \tag{7}$$

Condition (7) is often referred to as the Kuo instability criterion.

For $F \to \infty$ the perturbations are all equatorially trapped modes, so that we can make the approximation $\cos\theta \approx 1$, which reduces stability condition (6b) to:

$$\max(u) - \min(u) \leq \min\left[\left(\frac{1}{F} + \phi\right)^{1/2}\right]. \tag{8}$$

Here we have to remember that for $F \to \infty$ we still have the requirement $1 + \phi F > 0$.

In the derivation of these stability criteria no assumptions have been made about the structure of the perturbations (Ripa, 1983a). Therefore, these criteria apply equally well for

$$\text{shear instability:} \quad \langle \zeta' \rangle = \langle D' \rangle = \langle \phi' \rangle = 0$$

and

$$\text{inertial instability:} \quad \frac{\partial}{\partial\lambda}\zeta' = \frac{\partial}{\partial\lambda}D' = \frac{\partial}{\partial\lambda}\phi' = 0.$$

The primed variables are perturbations and $\langle\ \rangle$ denotes the zonal average.

For inertial instability an independent stability criterion can be derived (Ripa, 1983a):

The flow is inertially stable if

$$(f + 2u\tan\theta)\left(f - \frac{1}{\cos\theta}\frac{\partial}{\partial\theta}(u\cos\theta)\right) \geq 0. \tag{9}$$

For the equatorial β-plane this criterion may be simplified to:

$$f\left(f - \frac{\partial u}{\partial y}\right) \geq 0, \tag{10}$$

which is the classical criterion for hydrodynamic instability (Holton, 1979).

From now on we shall call instability due to the violation of conditions (6a), (6b) and (9), Kuo instability, gravity wave instability and hydrodynamic instability, respectively. In this paper we will not deal with gravity wave instability.

Figure 2 displays the amplitudes of the P_3^0 and P_5^0 flow for which conditions (6a) and (9) are violated. The plus and minus sign of ζ_3^0 correspond with easterly and westerly flow at the equator respectively. The amplitudes for Kuo instability decrease for increasing values of F. The hydrodynamic instability criterion is independent of F. The Kuo instability criterion is violated more easily when the ζ_3^0 and ζ_5^0 components have negative sign. This asymmetry is caused by the planetary vorticity appearing in (6a).

4.2 Numerical stability analysis

Baines (1976) investigated the linear stability of zonal flows for the nondivergent BVE on the sphere by numerically solving the eigenvalue problem. The zonal flows he studied consisted of a single Legendre polynomial P_n^0. For these flows the critical amplitudes for instability are close to the Kuo instability criterion. The kind of instability he found was shear instability. Extending the work of Baines (1976), we have investigated the stability of zonal flows for different values of F. We represent the vorticity ζ of the zonal flow by a single Legendre function and ϕ is calculated from the nonlinear balance equation.

By numerically computing the eigenvalues from the linearized perturbation equations the critical amplitudes of the P_3^0 and P_5^0 flow can be found beyond which instability in the T13 truncation occurs.

Within the range of positive values of $1 + \phi F$ no unstable rotational modes were found for the $+P_3^0$ flow. As will be explained below, this is due to the absence of an effective triad for instability of the $+P_3^0$ flow when only the symmetric modes are considered. The crosses in Fig. 2a are the numerically computed critical amplitudes for Kuo instability of the $-P_3^0$ flow. They show good correspondence with the Kuo instability criterion. The computed critical amplitudes are somewhat larger than the amplitudes derived from the Kuo instability criterion, but display the same dependence

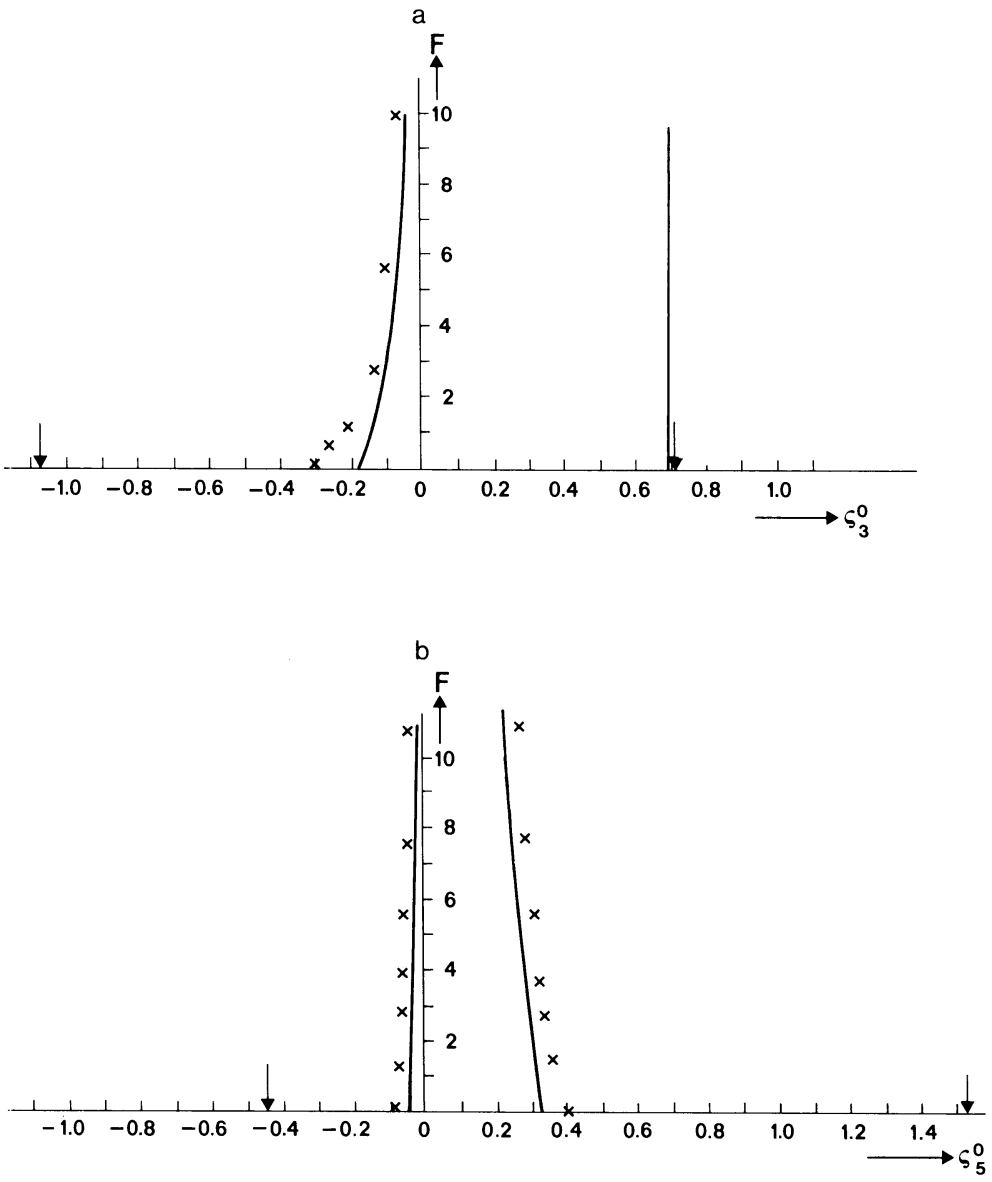

Fig. 2. Criteria for instability of the ζ_3^0 (a) and ζ_5^0 (b) flow as a function of F. Solid line : Kuo instability; Arrows: Hydrodynamic instability; The crosses denote the numerically computed critical amplitudes for instability.

on F. Here we have to recall that the Kuo instability criterion only marks necessary conditions for instability.

The crosses in Fig. 2b are the numerically computed critical amplitudes for unstable rotational modes of the P_5^0 flow. They agree well with the Kuo instability criterion.

Figure 3a, b display the computed growth rates as a function of F, and the amplitudes of the P_3^0 and P_5^0 flow, respectively. The critical amplitudes decrease for increasing F, but the growth rates also decrease. The thick dashed lines in Fig. 3b separate the areas where different perturbations have largest growth rates. For large F the $-P_3^0$ flow is unstable for a small range of amplitudes.

The frequency of the fastest growing modes is shown in Fig. 4. It can be seen that for all amplitudes of the P_3^0 and P_5^0 flow the frequency decreases with increasing F, however, the rate of decrease depends strongly on the amplitude of these flow components.

The structure of the fastest growing perturbation is rather insensitive to the particular value of F. Large changes occur only at the transition from one perturbation to another, indicated by the thick dashed lines in Figs. 3b and 4b.

Summarizing, we state that when F is increased from zero, zonal flows tend to become unstable at smaller amplitudes. The structure of the growing perturbations undergoes only minor changes but growth rate and frequency are strongly dependent on F.

4.3 Instability of zonal flows by the method of triad interactions

In several papers (Lorenz, 1972; Gill, 1974; Baines, 1976), the stability of planetary waves was investigated with severely truncated systems. It was shown that in many cases it is possible to get a good estimate of the growth rate and structure of perturbations that grow on a single unstable planetary wave by considering only a few component system. The most severely truncated system consists of one triad, i.e., the primary wave and two perturbing waves. On an infinite β-plane the relevant triad is resonant and on the sphere it is the triad closest to resonance.

The stability of zonal flows has never been investigated in terms of triad interactions. This may be ascribed to the fact that on an infinite β-plane resonant triads for which the primary wave is a zonal flow compo-

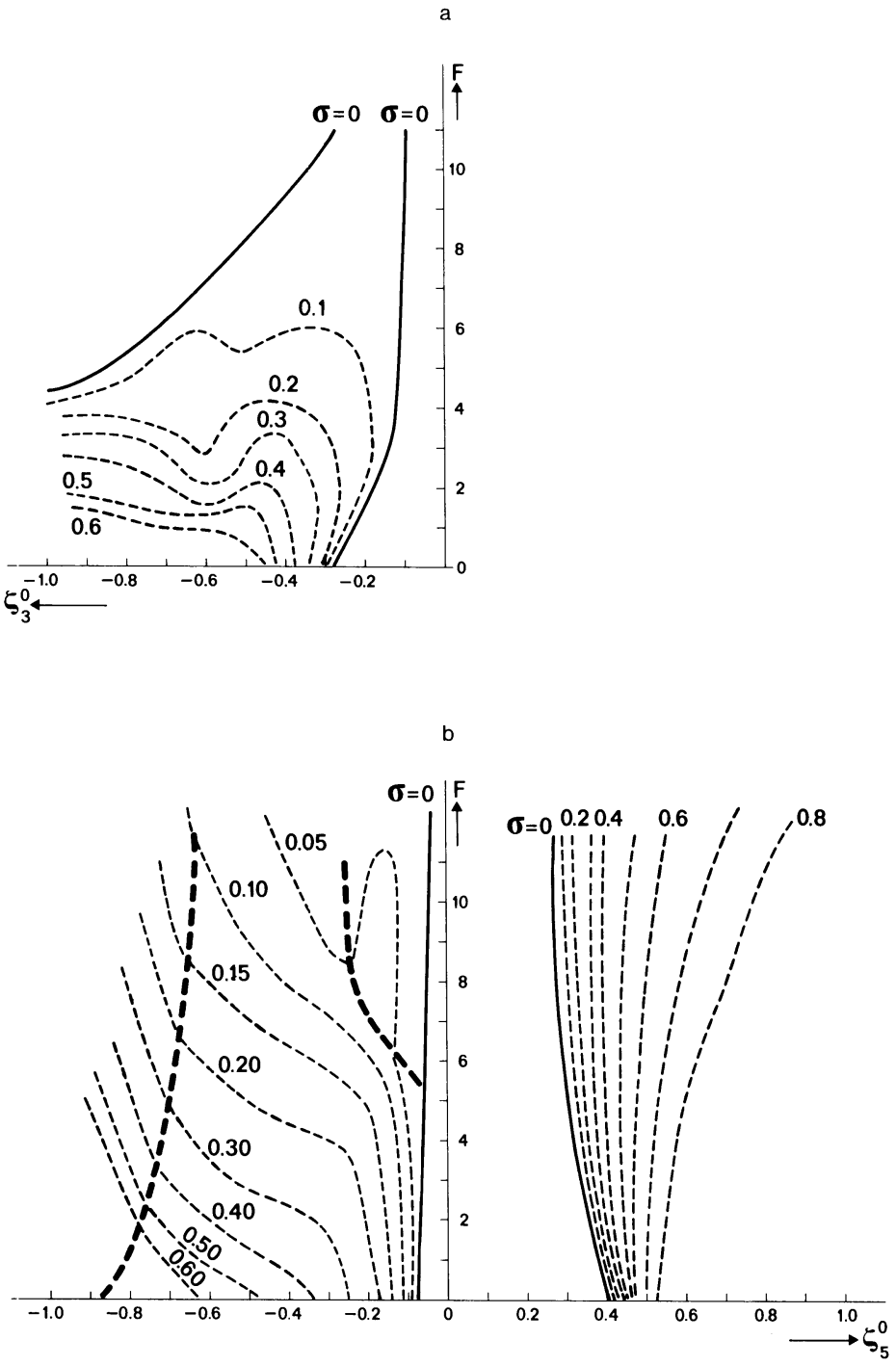

Fig. 3. Numerically computed growth rate of the fastest growing perturbation for the ζ_3^0 (a) and ζ_5^0 flow (b) as a function of F and the strength of the flow. The solid lines indicate the critical value for instability. The thick dashed lines in 3b mark the demarkation between two different modes.

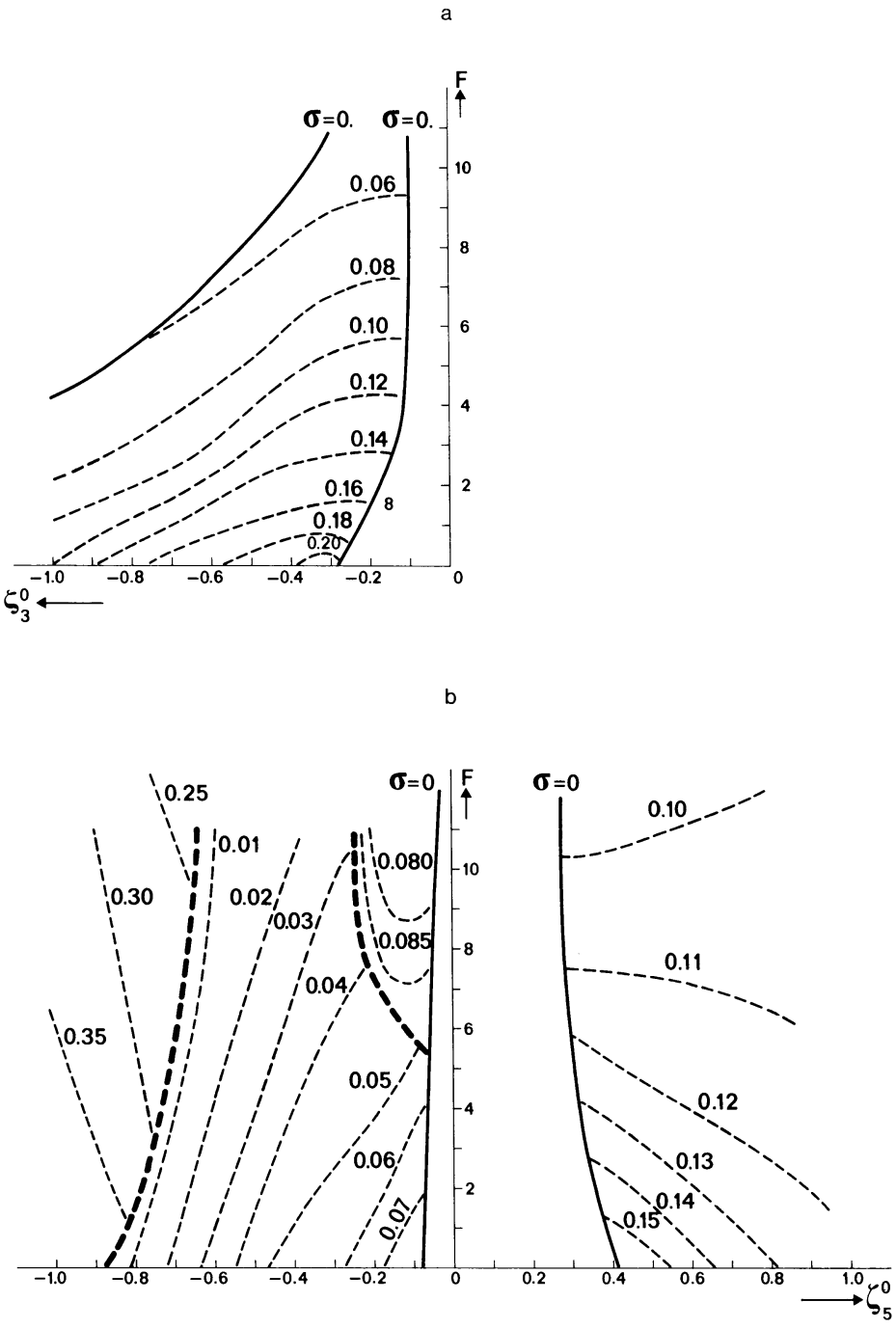

Fig. 4. As in Fig. 3 but for the frequency.

nent do not exist. This is a consequence of Fjørtofts theorem. Also for marginally unstable zonal flows, the growing perturbations have large gradients in a narrow critical layer. In the spectral domain, one needs many components in order to adequately resolve the structure of the perturbations in the critical layer. However, for physically relevant growth rates, the critical layer broadens to a zone with a smooth behaviour of the perturbations in this zone. It may therefore be possible to study the instability of zonal flows by considering only one or a few triad interactions.

For F = 0 we will try to interpret the numerical results by analytically computing the stability properties of the flow when only one triad is considered. The relevant equation is the BVE

$$\frac{\partial \zeta}{\partial t} + \left(\frac{\partial \psi}{\partial \lambda}\frac{\partial \zeta}{\partial \mu}\right) - \left(\frac{\partial \psi}{\partial \mu}\frac{\partial \zeta}{\partial \lambda}\right) + 2\frac{\partial \psi}{\partial \lambda} = 0. \tag{11}$$

The eigensolutions of the linearized equations are the spherical harmonics: $P_\gamma(\mu)e^{i(m_\gamma\lambda-\omega_\gamma t)}$, where we for simplicity have introduced the notation of Platzman (1962): $\gamma = n_\gamma + im_\gamma$.
They obey the dispersion relation, $\omega_\gamma = -2m_\gamma c_\gamma$, with

$$c_\gamma = \frac{1}{n_\gamma(n_\gamma + 1)} .$$

The evolution equation for small perturbations to a solution ζ_0 of this equation, neglecting quadratic terms among the perturbations is given by

$$\frac{\partial \zeta'}{\partial t} + \left(\frac{\partial \zeta_0}{\partial \mu}\frac{\partial \psi'}{\partial \lambda}\right) + \left(\frac{\partial \zeta'}{\partial \mu}\frac{\partial \psi_0}{\partial \lambda}\right) - \left(\frac{\partial \psi_0}{\partial \mu}\frac{\partial \zeta'}{\partial \lambda}\right) - \left(\frac{\partial \psi'}{\partial \mu}\frac{\partial \zeta_0}{\partial \lambda}\right) + 2\frac{\partial \psi'}{\partial \lambda} = 0 \tag{12}$$

where the primes denote the perturbation variables. If ζ_0 is a zonal flow, (12) becomes:

$$\frac{\partial \zeta'}{\partial t} + \left(\frac{\partial \zeta_0}{\partial \mu}\frac{\partial \psi'}{\partial \lambda}\right) - \left(\frac{\partial \psi_0}{\partial \mu}\frac{\partial \zeta'}{\partial \lambda}\right) + 2\frac{\partial \psi'}{\partial \lambda} = 0. \tag{13}$$

We now restrict the zonal flow to one single Legendre polynomial $\zeta_0(\mu) = \zeta_\gamma P_\gamma(\mu)$. This leads to:

$$\frac{\partial \zeta'}{\partial t} + \left[\zeta_\gamma \frac{dP_\gamma}{d\mu} \frac{\partial \psi'}{\partial \lambda}\right] + \left[c_\gamma \zeta_\gamma \frac{dP_\gamma}{d\mu} \frac{\partial \zeta'}{\partial \lambda}\right] + 2\frac{\partial \psi'}{\partial \lambda} = 0. \tag{14}$$

If we expand the perturbations in spherical harmonics,

$$\zeta'(\lambda,\mu,t) = \sum_\alpha \zeta'_\alpha(t) Y_\alpha(\lambda,\mu),$$

and project (14) on Y_β, we arrive at the equations for the coefficients of the perturbations:

$$\frac{d\zeta'_\beta}{dt} = 2imc_\beta \zeta'_\beta + \tfrac{1}{2}im\zeta_\gamma \sum_\alpha (c_\alpha - c_\gamma)\zeta'_\alpha K_{\alpha\beta\gamma} \tag{15}$$

where

$$K_{\alpha\beta\gamma} = \int_{-1}^{+1} P_\alpha P_\beta \frac{dP_\gamma}{d\mu}\, d\mu \quad \text{is the coupling integral.}$$

The most severe truncation of this infinite set of equations results in two equations for the perturbations ζ_α and ζ_β, which form a triad with the zonal flow ζ_γ:

$$\begin{aligned} \frac{d\zeta_\alpha}{dt} &= 2imc_\alpha \zeta_\alpha - \tfrac{1}{2}im\zeta_\gamma[(c_\gamma - c_\alpha)\zeta_\alpha K_{\alpha\alpha\gamma} + (c_\gamma - c_\beta)\zeta_\beta K_{\beta\alpha\gamma}] \\ \frac{d\zeta_\beta}{dt} &= 2imc_\beta \zeta_\beta - \tfrac{1}{2}im\zeta_\gamma[(c_\gamma - c_\beta)\zeta_\beta K_{\beta\beta\gamma} + (c_\gamma - c_\alpha)\zeta_\alpha K_{\alpha\beta\gamma}] \end{aligned} \tag{16}$$

together with the equations for their complex conjugates $\bar{\zeta}_\alpha$ and $\bar{\zeta}_\beta$. In these equations the primes have been omitted. On substituting solutions with a time dependence of the form $e^{i\omega t}$, (16) has nontrivial solutions only if

$$\omega^4 - \omega^2\{A^2 + C^2 + 2BD\} + \{A^2C^2 + B^2D^2 - 2ABCD\} = 0 \tag{17}$$

where

$$A = m[2c_\alpha - (c_\gamma - c_\alpha)\zeta_\gamma K_{\alpha\alpha\gamma}]; \quad B = -m(c_\gamma - c_\beta)\zeta_\gamma K;$$

$$C = m[2c_\beta - (c_\gamma - c_\beta)\zeta_\gamma K_{\beta\beta\gamma}]; \quad D = -m(c_\gamma - c_\alpha)\zeta_\gamma K;$$

and

$$K = K_{\alpha\beta\gamma} = K_{\beta\alpha\gamma}.$$

Growing perturbations exist if (17) has complex roots, which occurs when

$$[2(c_\alpha - c_\beta) - \zeta_\gamma[(c_\gamma - c_\alpha)K_{\alpha\alpha\gamma} - (c_\gamma - c_\beta)K_{\beta\beta\gamma}]]^2 + (c_\gamma - c_\alpha)(c_\gamma - c_\beta)\zeta_\gamma^2 K^2 < 0.$$

This occurs if ζ_γ is situated inside the interval formed by

$$\zeta_{\gamma_{1,2}} = 2\frac{\omega_\alpha - \omega_\beta}{m(p \pm \sqrt{q})} \tag{18}$$

when $p^2 + q$ is positive and outside this interval when it is negative. In this equation

$$\omega_\alpha = -2mc_\alpha, \quad \omega_\beta = -2mc_\beta, \quad p = -(c_\gamma - c_\alpha)K_{\alpha\alpha\gamma} + (c_\gamma - c_\beta)K_{\beta\beta\gamma},$$

and

$$q = (c_\gamma - c_\alpha)(c_\beta - c_\gamma)K^2.$$

The numerator at the right-hand side of (18) is the frequency difference of the two perturbations, which for two different perturbations never equals zero. Resonant triad interactions with a zonal flow as primary wave are thus impossible and the zonal flow is stable below a critical amplitude. For the triad interactions the critical amplitude depends on the amount of off-resonance, $\omega_\alpha - \omega_\beta$, and the strength of the nonlinear interaction terms in the denominator.

Due to Fjørtoft's theorem, only a few growing perturbations exist for the gravest meridional modes. For instance, for the P_3^0 flow only two unstable triads are possible:

$$(0,3)\begin{cases}(1,2)\\(1,4)\end{cases} \quad \text{and} \quad (0,3)\begin{cases}(2,2)\\(2,4)\end{cases}.$$

The amplitude for which the P_3^0 flow is unstable in each of these triads is computed from (18). The triad formed with the (1,2) and (1,4) component displays the rather unexpected behaviour that it is only unstable for negative values of ζ_3^0 between -0.31 and -4.37. The triad formed with the (2,2) and (2,4) component is stable between ζ_3^0 = -0.49 and +1.11.

In a hemispheric model with symmetrical perturbations, the triad formed with the (2,2) and (2,4) components is neglected and consequently unstable triad interactions for the $+P_3^0$ flow do not exist. This explains why for the $+P_3^0$ flow in the hemispheric T13 model, unstable perturbations were not found. The growth rate and frequency for the (1,2), (1,4) perturbation as a function of the amplitude of the ζ_3^0 component are displayed in Figs. 5a and 5b. These were computed from (17). For comparison the results of the T13 model are taken from Fig. 3. The critical amplitude for the occurrence of instability within the triad is -0.31, which is only slightly different from the critical amplitude in the T13 system (-0.29). When $|\zeta_3^0|$ is smaller than 2.0 the dependence of the growth rate of the perturbation on ζ_3^0 is very similar to the results obtained with the T13 truncation. For very large values of $|\zeta_3^0|$ the growth rate in the T13 truncation depends linearly on ζ_3^0, whereas for the triad it goes to zero. The frequency of the fastest growing mode in the T13 truncation depends more strongly on the amplitude of ζ_3^0. The structure of the growing perturbations is very similar; 97% of the kinetic energy of the perturbation in the T13 truncation is in the (1,2), (1,4) components.

This example illustrates that, analogous to planetary waves, the instability of zonal flows can be approximated by considering only one triad, namely, the most efficient triad. For very large values of the zonal flow, more components are needed for an adequate description of its stability properties. The most efficient triad is defined as the one with the smallest critical amplitude. This critical amplitude is determined by the amount of "off-resonance" and the strength of the nonlinear interaction terms.

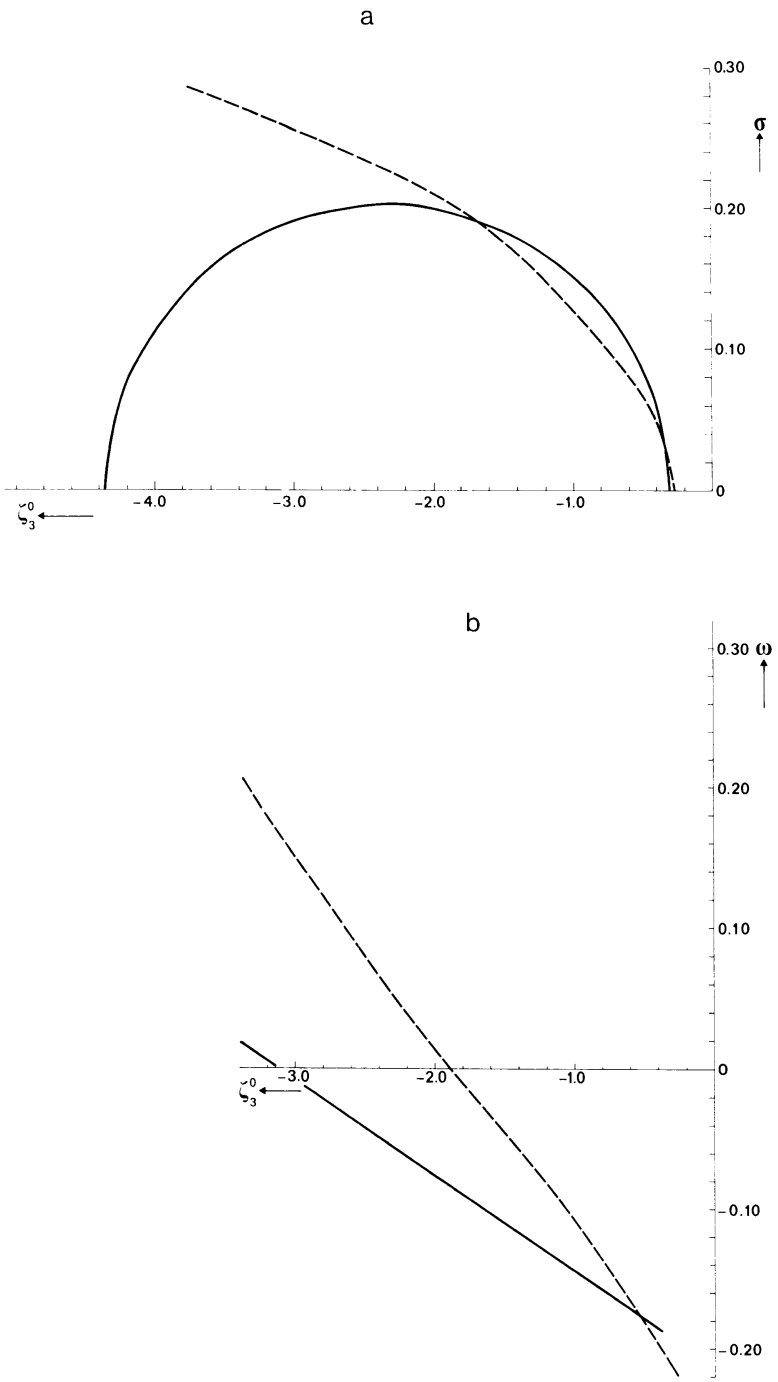

Fig. 5. Computed growth rate (a) and frequency (b) of the fastest growing mode of the $-\zeta_3^0$ flow for F = 0.
Solid line : triad
Dashed line: T13 truncation

5. Free planetary waves

In this section we will investigate the stability of the (2,3) wave superimposed on a zonal flow which is in solid body rotation. We will first consider the case where F = 0 and secondly F > 0.

For F = 0, the numerically computed growth rates (σ) as a function of the amplitude of the (2,3) wave (A) and the strength of the solid body rotation (ζ_1^0) are displayed in Fig. 6. The critical amplitude for instability (the line $\sigma = 0$) depends linearly on ζ_1^0. This is different from the situation on a β-plane where the stability of a planetary wave is independent of the strength of the uniform zonal flow on which it is superimposed (Lorenz, 1972). For values of A larger than 0.4 the dependence of σ on A and ζ_1^0 is rather complex, displaying local minima and maxima.

Similarly as in the case for the zonal flow we will analytically compute the stability of the (2,3) wave by considering only the most efficient triad.

Inserting in (12) the expansion for a single spherical harmonic superimposed on a solid body rotation:

$$\zeta_0(\lambda,\mu,t) = \zeta_1^0 P_1^0(\mu) + \zeta_y P_y(\mu)\, e^{i(m_y\lambda-\omega_y t)} \tag{19}$$

which obeys the dispersion relation:

$$\omega_y = -2m_y c_y - \sqrt{(3/2)}\, m_y \zeta_1^0 (c_y - 1/2) \tag{20}$$

we arrive at the following perturbation equation:

$$\frac{\partial \zeta'}{\partial t} - im_y c_y \zeta_y P_y e^{i(m_y\lambda-\omega_y t)} \frac{\partial \zeta'}{\partial \mu}$$

$$+ \left[\zeta_1^0\sqrt{(3/2)} + \zeta_y \frac{dP_y}{d\mu} e^{i(m_y\lambda-\omega_y t)}\right] \frac{\partial \psi'}{\partial \lambda}$$

$$+ \left[\tfrac{1}{2}\zeta_1^0\sqrt{(3/_2)} + c_\gamma \zeta_\gamma \frac{dP_\gamma}{d\mu} e^{i(m_\gamma \lambda - \omega_\gamma t)}\right]\frac{\partial \zeta'}{\partial \lambda}$$

$$- \left(im_\gamma \zeta_\gamma P_\gamma e^{i(m_\gamma \lambda - \omega_\gamma t)}\right)\frac{\partial \psi'}{\partial \mu} + 2\frac{\partial \psi'}{\partial \lambda} = 0 \ , \qquad (21)$$

where we have used the identity $\psi_\gamma = -c_\gamma \zeta_\gamma$, and $P_1^0(\mu) = \sqrt{(3/_2)}\mu$.

Following Lorenz (1972), we will analyze the stability of this flow in a coordinate system moving with the phase velocity of the primary wave. We therefore apply the following coordinate transformation:

$$\lambda_0 = \lambda - \frac{\omega_\gamma}{m_\gamma} t.$$

Equation (26) then transforms into

$$\frac{\partial \zeta'}{\partial t} - \left(im_\gamma c_\gamma \zeta_\gamma P_\gamma e^{im_\gamma \lambda_0}\right)\frac{\partial \zeta'}{\partial \mu} + \left[\zeta_1^0\sqrt{(3/_2)} + \zeta_\gamma \frac{dP_\gamma}{d\mu} e^{im_\gamma \lambda_0} + 2\right]\frac{\partial \psi'}{\partial \lambda_0}$$

$$+ c_\gamma\left[2 + \sqrt{(3/_2)}\zeta_1^0 + \zeta_\gamma \frac{dP_\gamma}{d\mu} e^{im_\gamma \lambda_0}\right]\frac{\partial \zeta'}{\partial \lambda_0} - \left(im_\gamma \zeta_\gamma P_\gamma e^{im_\gamma \lambda_0}\right)\frac{\partial \psi'}{\partial \mu} = 0. \qquad (22)$$

Next we expand the perturbations into spherical harmonics:

$$\zeta'(\lambda_0, \mu, t) = \sum_\alpha \zeta'_\alpha(t) Y_\alpha(\lambda_0, \mu)$$

and project (22) on Y_β. We then arrive at the equations for the coefficients of the perturbations:

$$\frac{d\zeta'_\beta}{dt} = -im_\beta \zeta'_\beta (c_\gamma - c_\beta)\left(\sqrt{(3/_2)}\ \zeta_1^0 + 2\right) - \frac{i}{2}\zeta_\gamma \sum_\alpha \zeta'_\alpha (c_\gamma - c_\alpha) K_{\beta\alpha\gamma}$$

where

$$K_{\beta\alpha\gamma} = \int_{-1}^{+1} P_\beta \left(m_\alpha P_\alpha \frac{dP_\gamma}{d\mu} - m_\gamma P_\gamma \frac{dP_\alpha}{d\mu}\right) d\mu \qquad (23)$$

Similarly as for the stability of a zonal flow we can derive from (23) an expression for the critical amplitude of the primary wave γ within a triad formed with two perturbations α and β. Growing perturbations exist if

$$\zeta_\gamma^2 > 4(1 + \tfrac{1}{2}\sqrt{(3/2)}\zeta_1^0)^2 \frac{\{m_\alpha(c_\alpha - c_\gamma) - m_\beta(c_\gamma - c_\beta)\}^2}{(c_\alpha - c_\gamma)(c_\gamma - c_\beta)K^2}. \qquad (24)$$

This equation includes the result of Baines (1976) derived for a free Rossby wave in a medium at rest. The part of the numerator between brackets reflects the resonance condition. It is equal to zero if $\omega_\alpha + \omega_\beta + \omega_\gamma = 0$. The critical amplitude for instability at off-resonance, i.e., when $\omega_\alpha + \omega_\beta + \omega_\gamma \neq 0$ depends on the amount of off-resonance and the strength of the nonlinear interactions, which are determined by the coupling integral K.

From (24) we can see that the stability of the planetary wave is also linearly dependent on the strength of the solid body rotation on which the wave is superimposed. This is in agreement with the previous numerical results. The difference between these results and the results for the β-plane is due to the fact that the modification of the phase speed of the wave by the zonal flow is dependent on wavenumber for a spherical domain, while on the β-plane it is not.

By computing σ for the (2,3) wave in all possible triad interactions it appears that the most efficient triad is formed with the (1,2) and (1,4) wave. Figure 7 displays for this triad σ as a function of A and ζ_1^0.

For small values of A the growth rate computed by considering only the most efficient triad is in good agreement with the numerical results for the T13 model (Fig. 6). When A becomes larger than 0.4 the growth rates become noticably different in the two truncations. Thus for realistic values of the amplitude of ζ_3^2 the instability process can essentially be described as an interaction among waves in only one triad. This result is similar to what we derived for zonal flows. It has also been demonstrated by Baines (1976) for a large number of planetary waves in the absence of a solid body rotation.

We will now proceed to the case where F > 0. The eigenvectors of the linearized SWE are the Hough functions, which can be written as

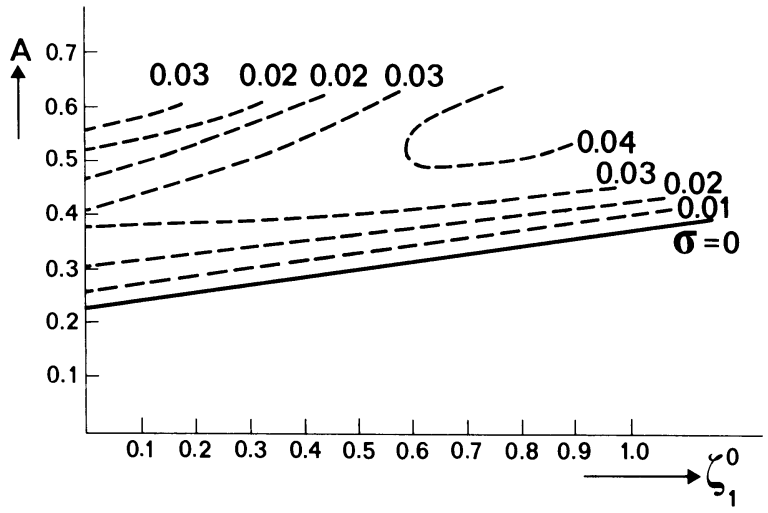

Fig. 6. Numerically computed growth rates of the fastest growing perturbation for the ζ_3^2 wave superimposed on a solid body rotation as a function of ζ_1^0 and for F = 0.

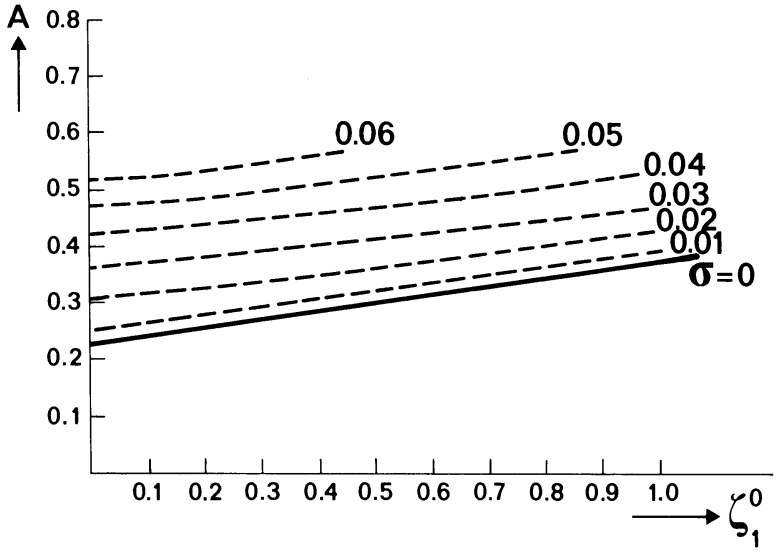

Fig. 7. Analytically computed growth rates for the ζ_3^2 wave superimposed on a solid body rotation as a function of ζ_1^0 and for F = 0.

$$H_\gamma(\lambda,\mu)e^{-i\omega_\gamma t} = \begin{bmatrix} B_{\zeta_\gamma}(\mu) \\ B_{D_\gamma}(\mu) \\ B_{\phi_\gamma}(\mu) \end{bmatrix} e^{i(m_\gamma\lambda-\omega_\gamma t)}, \qquad (25)$$

where γ is the mode number and B_{ζ_γ}, B_{D_γ} and B_{ϕ_γ} the meridional structure of ζ, D and ϕ for this mode. Extensive computations of these Hough functions in dependence of F has been performed by Longuet-Higgins (1968).

After expanding the variables in Hough functions

$$\begin{bmatrix} \zeta\ (\lambda,\mu,t) \\ D\ (\lambda,\mu,t) \\ \phi\ (\lambda,\mu,t) \end{bmatrix} = \sum_\alpha A_\alpha(t)H_\alpha(\lambda,\mu) \qquad (26)$$

and projection on $H_\beta(\lambda,\mu)$, we arrive at the evolution equation for the coefficients of the expansion

$$\frac{d}{dt}A_\beta(t) = -im_\beta\omega_\beta A_\beta + i\sum_{\alpha,\gamma}\Pi_{\beta\alpha\gamma}A_\alpha A_\gamma \qquad (27)$$

where $\Pi_{\beta\alpha\gamma}$ are the coupling integrals for the Hough functions. For $F > 0$ the couping integrals $\Pi_{\beta\gamma\gamma} \neq 0$, and consequently the Hough functions are not exact solutions of the nonlinear equations.

A single unperturbed mode γ generates a secondary mode β by self-interaction. In case of self-resonance, i.e., $\omega_\gamma + \omega_\gamma + \omega_\beta = 0$ the energy transfer to the secondary wave is most efficient.

Because of the wave rule ($m_\gamma + m_\gamma + m_\beta = 0$) for the coupling integrals to be nonzero, there are two possibilities for self-resonance:

1) Second Harmonic Resonance (SHR), which occurs if a primary wave γ is at self-resonance with its first harmonic β:

$$2\omega(m_\gamma,n_\gamma) = \omega(m_\beta,n_\beta)$$

$$m_\beta = 2m_\gamma.$$

2) Long wave/short wave Resonance (LSR), which occurs if:

$$\omega_\gamma = 0 \text{ and } m_\beta = 0.$$

In this case the primary wave is at self-resonance with the zonal flow.

For an equatorial β-plane, Boyd (1983b) has demonstrated that in a resting mean state, SHR is only possible between a Rossby primary wave and a Rossby harmonic wave or between a westward traveling primary gravity wave and a westward traveling gravity harmonic; LSR occurs for Rossby waves superimposed on a zonal flow which makes them stationary ($\omega_\gamma = 0$).

Before proceeding to a numerical stability analysis of the Hough modes we will first study their evolution in time close to resonance. The time evolution can be described by the interaction of the primary wave γ and its secondary mode β (Boyd, 1983b):

$$\begin{aligned} \frac{dA_\gamma}{dt} &= - im_\gamma \omega_\gamma A_\gamma - iIA_\gamma A_\beta, \\ \frac{dA_\beta}{dt} &= - im_\beta \omega_\beta A_\beta - iIA_\gamma^2, \end{aligned} \tag{28}$$

where A_γ and A_β are the amplitudes of the primary and secondary wave, respectively, and $I = \Pi_{\beta\gamma\gamma} = \Pi_{\gamma\gamma\beta}$, the interaction coefficient. For reasons of mathematical simplicity we choose a coordinate system moving with the secondary wave A_β. Equation (28) then becomes:

$$\begin{aligned} \frac{dA'_\gamma}{dt} &= -im_\gamma \omega'_\gamma A'_\gamma - iIA'_\gamma A'_\beta \\ \frac{dA'_\beta}{dt} &= -iIA'^2_\gamma \end{aligned} \tag{29}$$

where the primes denote the variables in the moving coordinate system. In case of self-resonance, $\omega'_\gamma = 0$. Equation (29) can be reduced to a second-order differential equation for the perturbation A_β:

$$\frac{d^2A_\beta}{dt^2} + 2i(m_\gamma \omega_\gamma + IA_\beta)\frac{dA_\beta}{dt} = 0 \tag{30}$$

where the primes have been ignored. The initial conditions are:

$$A_\beta = 0 \text{ and } \frac{dA_\beta}{dt} = -iIA_0^2 \text{ where } A_0 = A_\gamma(0).$$

The solution to (30) is:

$$\frac{A_\beta(t^*)}{|A_0|} = \alpha + i\sqrt{(1-\alpha^2)}\,\tanh\left[-t^*.\sqrt{(1-\alpha^2)} + i\,\arctan\left(\frac{\alpha}{\sqrt{(1-\alpha^2)}}\right)\right] \quad (31)$$

where

$$\alpha = \frac{m_\gamma \omega_\gamma}{IA_0} \text{ and } t^* = IA_0 t.$$

Figure 8a, b displays the time dependent behaviour of the amplitude and phase of $A = \frac{A_\beta}{|A_0|}$ for different values of α.

In case of self resonance ($\alpha = 0$), (31) reduces to

$$A = -i\,\tanh(t^*) \quad (32)$$

and all the energy of the primary wave is irreversibly transferred to the secondary wave, which is 90° out of phase with the primary wave.

For $0 < |\alpha| < 1$, all the energy of the primary wave is still transferred to the secondary wave, but the rate of energy transport becomes smaller for increasing α. The phase difference between the secondary and the primary wave in the final state approaches zero for $|\alpha| \to 1$. If $|\alpha| > 1$, the energy of the primary wave is no longer irreversibly transferred to the secondary wave, but instead a vacillation exists between the two waves. The amplitude and period of the vacillation decrease for increasing α. For $\alpha = 4$, the maximum amplitude of the secondary wave is only 25% of the primary wave. The result for $\alpha = 0$ was also derived by Boyd (1983b) for the equatorial β-plane.

Close to the resonance point $\alpha = 0$, the Hough modes are no longer even approximate solutions to the shallow water equations. This means that for small values of α a stability analysis can only be interpreted in terms of the sensitivity of the evolution of the flow pattern to initial errors. In other words it provides information about the predictability of initial states that are represented by Hough modes. For large values of α, we may assume that the Hough modes are approximate solutions.

For the T13 truncation we have investigated the stability of the "(2,3)" Hough mode superimposed on a solid body rotation as a function of F.

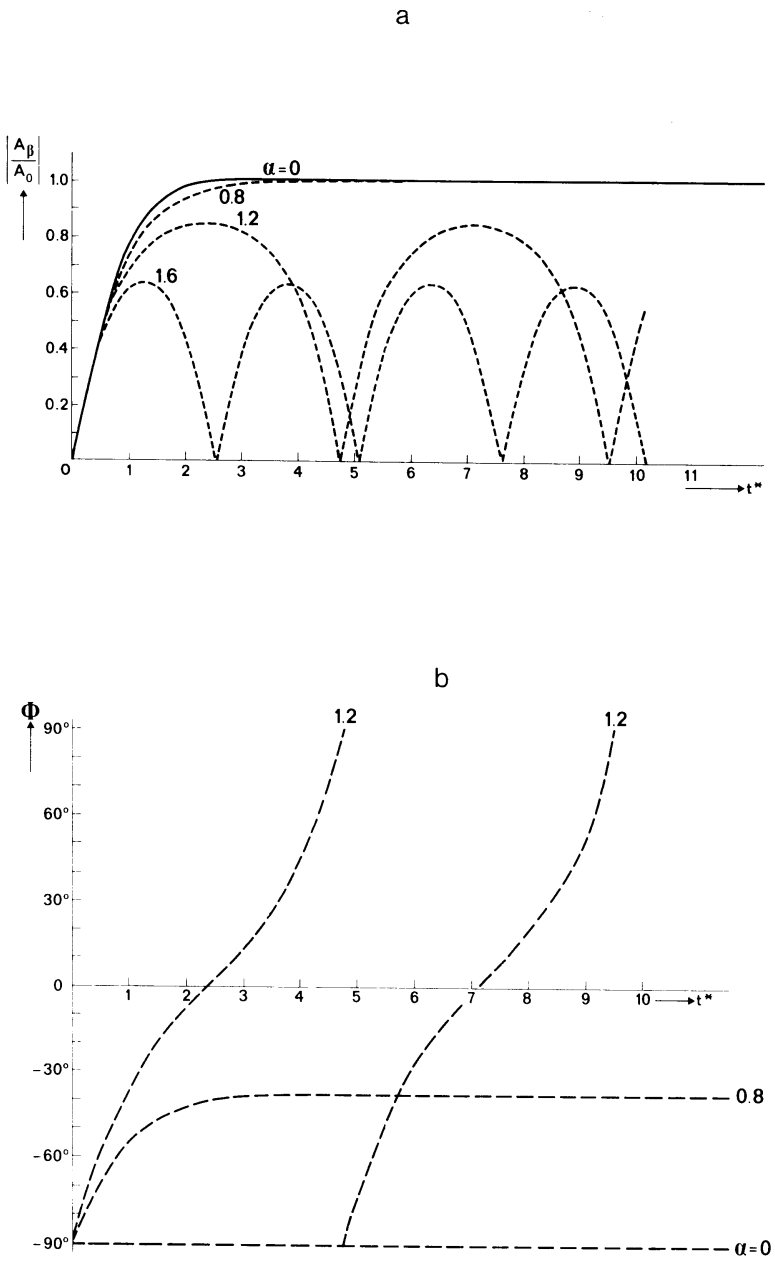

Fig. 8. Evolution of the amplitude (a) and phase (b) of the secondary wave growing on a primary Hough mode for different values of α. Resonance occurs for $\alpha = 0$.

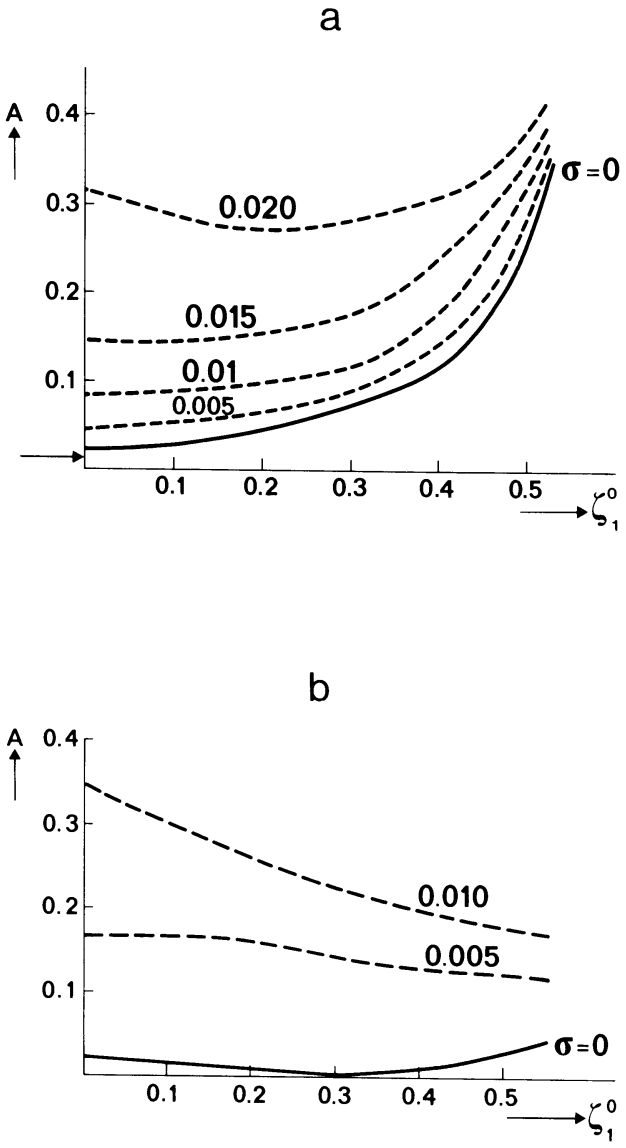

Fig. 9. As Fig. 6, but for F = 2.75; (a) growing perturbations with m odd; (b) growing perturbations with m even.

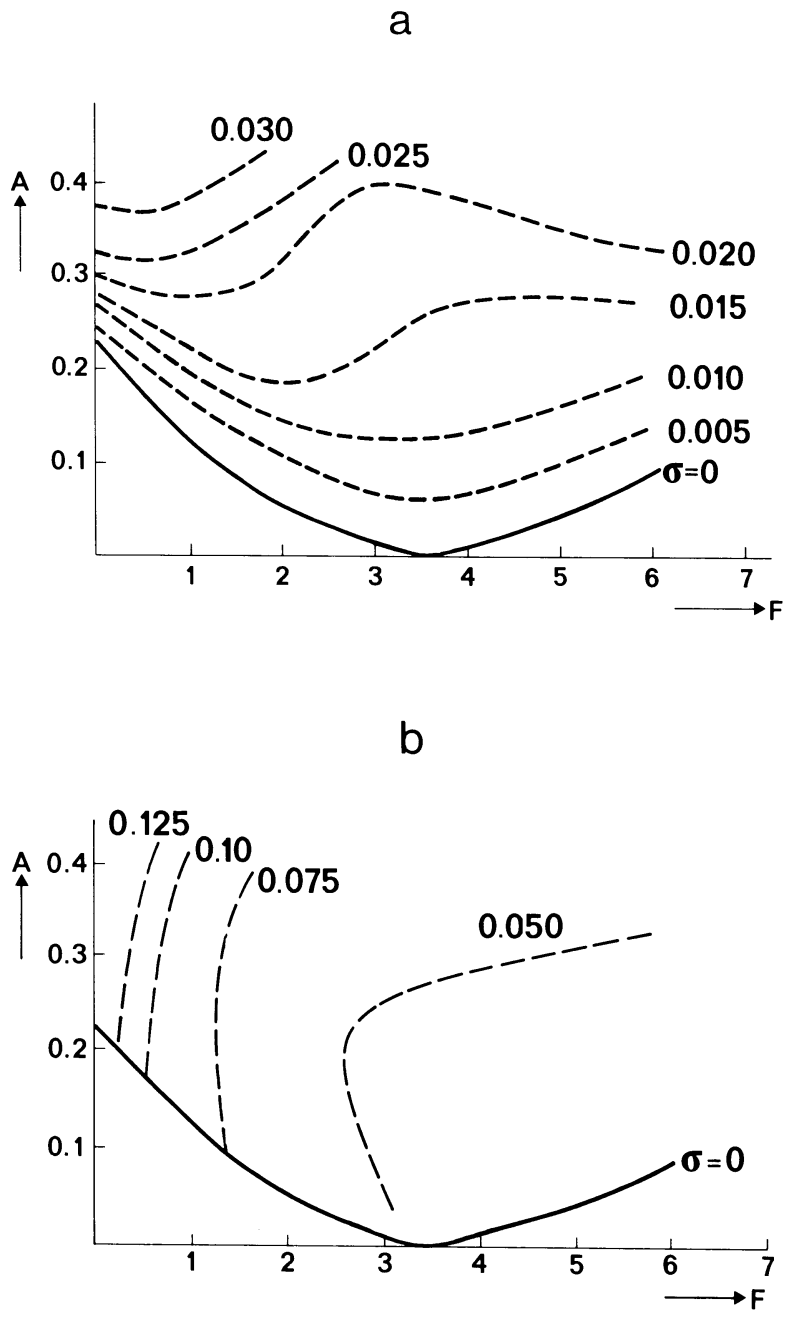

Fig. 10. Growth rate (a) and frequency (b) of the most rapidly growing perturbations with m odd as a function of F and A for $\zeta_1^0 = 0$.

The growing perturbations contain either wave components with m odd or m even. When only antisymmetric modes in ψ are considered, perturbations with m even are always due to dyad interactions, whereas perturbations with m odd result from triad interactions. For F = 0, in which case dyad interactions are impossible, only growing perturbations with m odd exist, a result which can also be derived from Fjørtoft's theorem. The maximum growth rates for both types of perturbations are shown for F = 2.75 in Fig. 9a (m odd) and Fig. 9b (m even). This value for F corresponds to a scale height of 8 km which seems reasonable for barotropic flow in the atmosphere. The growth rates are shown as a function of the strength of ζ_1^0 and A. Comparing Fig. 9a with Fig. 6 we see that for small values of ζ_1^0 there is a substantial reduction of the critical amplitude, but the increase of the growth rate with increasing amplitudes of the mode is slower. This is in agreement with the results of the stability analysis of zonal flows. The arrow in Fig. 9a marks the critical amplitude computed from (24) for $\zeta_1^0 = 0$, when the frequencies of the Hough modes at F = 2.75 are inserted. For the coupling integrals in this equation we have used the values for F = 0. The fact that the critical amplitude found in this way compares well with the numerically computed critical amplitude suggests that for F = 2.75, a triad interaction approach is also approximately valid, and that the drop in the critical amplitude at $\zeta_1^0 = 0$ can almost completely be ascribed to the change in the frequencies. This is further confirmed by inspection of the most rapidly growing perturbations, showing the dominance of the "(1,2)" and "(1,4)" modes. The much stronger increase in the critical amplitude for increasing ζ_1^0 at F = 2.75 is probably due to changes in the normal mode structure. For F = 0 the structure of the normal modes are spherical harmonics and independent of ζ_1^0. For F = 2.75 these structures change noticeably with increasing ζ_1^0.

The critical amplitude for the perturbations with m even (Fig. 9b) approaches zero for $\zeta_1^0 = 0.3$, for which the "(2,3)" mode is stationary and has LSR. The growth rates are much smaller than for perturbations with m odd. Only for large values of ζ_1^0 does the growth rate due to dyad interactions become increasingly more important.

Figure 10a, b displays the growth rate and frequency of the most rapidly growing perturbations for m odd as a function of F. In this experiment, $\zeta_1^0 = 0$. The critical amplitude is zero when F is approximately 3.5, for which the triad formed with the "(1,2)" and "(1,4)" mode is resonant. Also

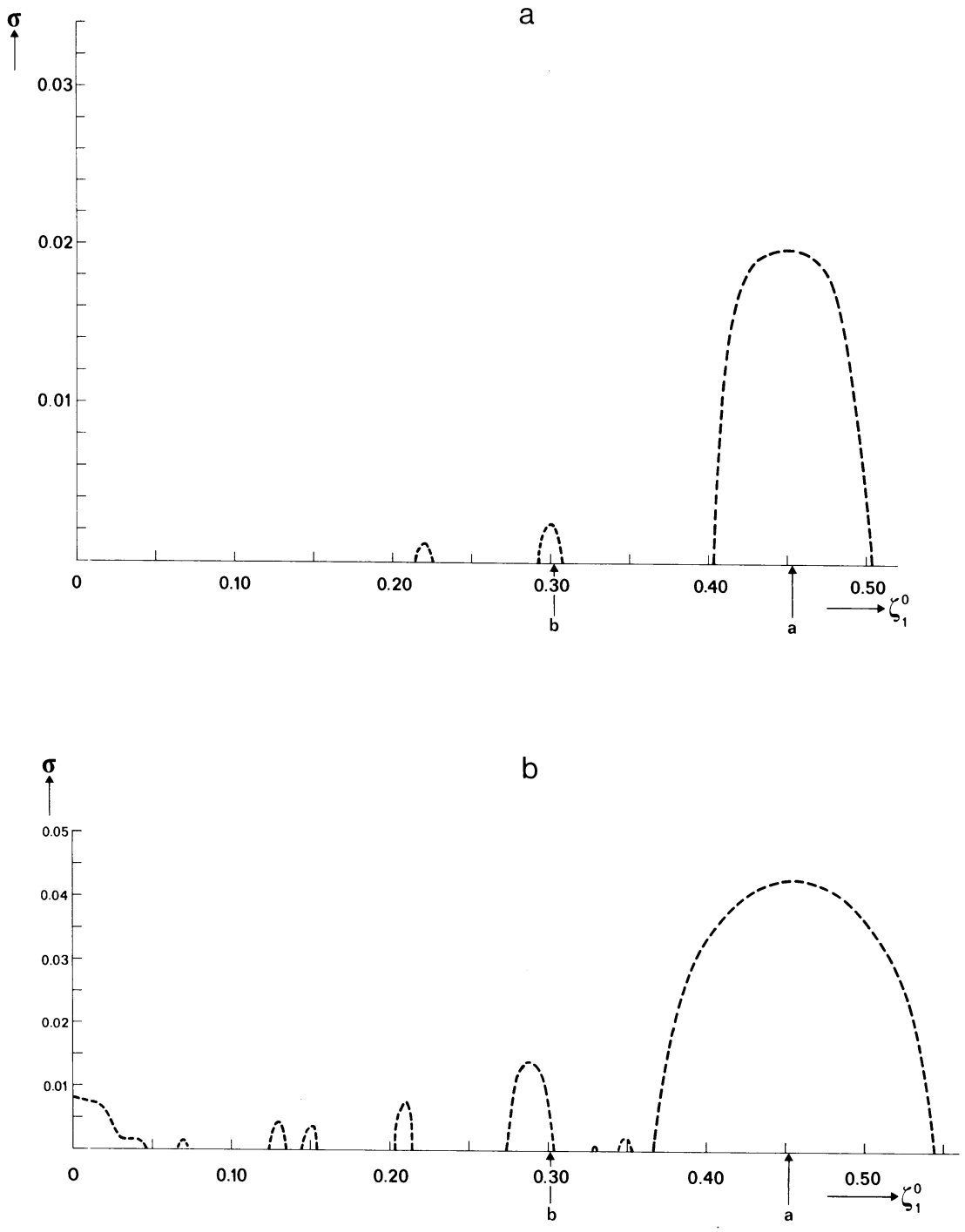

Fig. 11. Numerically computed growth rates of the most rapidly growing perturbations for the forced stationary (2,3) wave as a function of ζ_1^0 and for F = 0. The arrows a and b denote the resonance points for the triad formed with the (1,2), (1,4) and (1,2), (3,4) components respectively. (a) $|\zeta_3^2| = 0.2$; (b) $|\zeta_3^2| = 0.4$.

for this value of F the increase of σ with A shows a minimum. The frequency decreases and shows a stronger dependence on A for increasing values of F.

The critical amplitude for perturbations with m even (not shown) approaches zero for increasing F; however, the growth rates for these types of perturbations are much slower.

6. Forced stationary waves

In this section we will investigate the stability of forced stationary waves by assuming that we have appropriate forcing terms in the equations, such that the considered wave has zero frequency.

In the atmosphere, stationary waves are forced by different forcing mechanisms, including orographic, diabatic and nonlinear wave forcing. As a first approximation we will assume that the stationary planetary waves are forced by a prescribed forcing. The forcing term needed to keep the wave stationary is simply calculated as a residual term in the momentum equations to keep the time derivative equal to zero.

The vorticity of the forced stationary wave is described by a single spherical harmonic, the divergence is set to zero, and the geopotential is calculated from the nonlinear balance equation. This has the advantage that the structure of the waves is the same for all values of Lamb's parameter, in contrast to the structure of free waves which depend on F.

For different amplitudes of the (2,3) wave, we have numerically computed its stability as a function of the strength of the solid body rotation. For F = 0, the growth rate σ as a function of ζ_1^0 is shown in Fig. 11a and 11b for $|\zeta_3^2|$ = 0.2 and 0.4, respectively. Figure 11a displays two peaks in the growth rate for ζ_1^0 = 0.3 and 0.45, the latter one being dominant. When $|\zeta_3^2|$ is increased from 0.2 to 0.4 (Fig. 11b), the peaks in σ become larger and broader and the one at ζ_1^0 = 0.3 shifts to a smaller value of the solid body rotation. Also, new peaks appear that are significantly smaller than the first two.

Again we will try to interpret the results for F = 0 in terms of triad interactions.

Because of the constant forcing term, the evolution equation for small perturbations to the stationary wave is the same as for free planetary waves and is given by (12), where ψ_0 is now a stationary wave.

For a stationary wave consisting of a single spherical harmonic superimposed on a solid body rotation, (21) reduces to

$$\frac{\partial\zeta'}{\partial t} - im_\gamma c_\gamma \zeta_\gamma P_\gamma e^{im_\gamma\lambda}\frac{\partial\zeta'}{\partial\mu} + [\zeta_1^0\sqrt{(3/2)} + \zeta_\gamma \frac{dP_\gamma}{d\mu} e^{im_\gamma\lambda}]\frac{\partial\psi'}{\partial\lambda} +$$

$$[\tfrac{1}{2}\zeta_1^0\sqrt{(3/2)} + c_\gamma\zeta_\gamma \frac{dP_\gamma}{d\mu} e^{im_\gamma\lambda}]\frac{\partial\zeta'}{\partial\lambda} - im_\gamma\zeta_\gamma P_\gamma e^{im_\gamma\lambda}\frac{\partial\psi'}{\partial\mu} + 2\frac{\partial\psi'}{\partial\mu} = 0. \qquad (33)$$

Expansion of the perturbation in spherical harmonics and projection on Y_β gives

$$\frac{d\zeta'_\beta}{dt} = -im_\beta\zeta'_\beta[\sqrt{(3/2)}\zeta_1^0(\tfrac{1}{2} - c_\beta) - 2c_\beta] - \tfrac{1}{2}i\zeta_\gamma \sum_\alpha \zeta'_\alpha (c_\gamma - c_\alpha)K_{\beta\alpha\gamma}. \qquad (34)$$

Comparing (34) with (23) for a free wave, we see that the equations are identical for

$$\zeta_1^0 = 4\sqrt{(2/3)}[\frac{1}{n_\gamma(n_\gamma + 1) - 2}]. \qquad (35)$$

For this value of the solid body rotation, the free wave becomes stationary and consequently the artificial forcing term is zero.

Reducing the infinite set of equations to a triad consisting of the primary wave γ and two perturbations α and β, we find after substituting solutions of the form $e^{i\omega t}$, that nontrivial solutions exist if:

$$\omega^2 + (A - C)\omega + (AC - BD) = 0$$

where

$$A = m_\alpha\{\sqrt{(3/2)}\zeta_1^0(\tfrac{1}{2} - c_\alpha) - 2c_\alpha\} \quad B = \tfrac{1}{2}\zeta_\gamma(c_\gamma - c_\beta)K$$

$$C = m_\beta\{\sqrt{(3/2)}\zeta_1^0(\tfrac{1}{2} - c_\beta) - 2c_\beta\} \quad D = \tfrac{1}{2}\zeta_\gamma(c_\gamma - c_\alpha)K \qquad (36)$$

Growing perturbations exist if this polynomial in ω has complex roots, which occurs for

$$\zeta_y^2 > \frac{\{m_\alpha[\sqrt{(3/2)}\zeta_1^0(\tfrac{1}{2} - c_\alpha) - 2c_\alpha] + m_\beta[\sqrt{(3/2)}\zeta_1^0(\tfrac{1}{2} - c_\beta) - 2c_\beta]\}^2}{(c_\alpha - c_y)(c_y - c_\beta)K^2}. \quad (37)$$

In contrast to the situation for free waves, we can always find a value of ζ_1^0 such that the critical amplitude is zero. This can be understood if we consider the resonance condition of a forced stationary wave:

$$\omega_\alpha + \omega_\beta = 0 \quad (38)$$

where ω_α and ω_β are the natural frequencies of the perturbations α and β.

Because ω_α and ω_β depend differently on ζ_1^0, every triad formed with the wave γ becomes resonant for a particular value of the solid body rotation. A particular triad will always have two resonance points that are due to the sum and difference of the absolute value of the frequencies.

The critical amplitude for which the triad becomes resonant is

$$\zeta_1^0 = 4\sqrt{(2/3)}\,\frac{m_\alpha c_\alpha + m_\beta c_\beta}{m_\alpha - 2m_\alpha c_\alpha + m_\beta - 2m_\beta c_\beta}. \quad (39)$$

For the forced (2,3) wave, resonance with the (1,2) and (1,4) wave occurs for $\zeta_1^0 = -1.633$ and 0.452, while resonance with the (1,2) and (3,4) wave occurs for $\zeta_1^0 = -0.027$ and 0.307.

Comparing the positive values with those for which Fig. 11a displays maxima in σ, it is evident that the peaks can be attributed to resonant interactions in single triads. This is confirmed by investigation of the structure of the fastest growing perturbations in the T13 model at $\zeta_1^0 = 0.3$ and 0.45. They are dominated by the (1,2) and (3,4) waves at $\zeta_1^0 = 0.3$ and by the (1,2) and (1,4) waves at $\zeta_1^0 = 0.45$. The small peaks appearing in Fig. 11b when the (2,3) wave is increased from 0.2 to 0.4 do not correspond with resonant triads. They are due to more complicated interactions.

Next we will try to understand the shift in the resonance peak in Fig. 11b. Inspection of the growing perturbations for this peak reveals an increasing contribution of the (1,4) wave for increasing amplitudes of the

primary (2,3) wave. Similarly the growing perturbation of the other resonance peak at $\zeta_1^0 = 0.45$ displays a contribution from the (3,4) wave, although this contribution is much smaller. Apparently there is a mutual interaction between the two triads.

In order to investigate this more closely we have analyzed the set of equations containing both triads. The system of equations contains four components, i.e., the primary wave and three perturbations instead of four, because the (1,2) component belongs to both triads. This set of equations can still be examined in an analytical way.

The method is the same as for a triad, but now a system of six equations for the perturbations and their complex conjugates has to be solved. If we again assume perturbations of the form $e^{i\omega t}$ this leads to a sixth-order equation in ω:

$$\omega^6 + a_2\omega^4 + a_1\omega^2 + a_0 = 0 \qquad (40)$$

with

$$a_0 = g_3^2A + g_2^2B + g_1^2C + 2\{-g_1^2g_2^2g_3^2 - g_1g_3pr - g_2g_3pq + g_1g_2qr\},$$

$$a_1 = A + B + C + 2\{g_1^2r + g_2^2q + g_3^2p + pq + qr + pr\},$$

$$a_2 = g_1^2 + g_2^2 + g_3^2 + 2(p + q + r),$$

where

$$g_i = m_i\{\sqrt{(3/2)}\zeta_1^0(\tfrac{1}{2} - c_i) - 2c_i\}, \qquad i = 1,2,3,$$

$$p = \tfrac{1}{4}(\zeta_\alpha)^2(c_\alpha - c_1)(c_\alpha - c_2)K_{12_\alpha}K_{21_\alpha},$$

$$q = \tfrac{1}{4}(\zeta_\alpha)^2(c_\alpha - c_1)(c_\alpha - c_3)K_{13_\alpha}K_{31_\alpha},$$

$$r = \tfrac{1}{4}(\zeta_\alpha)^2(c_\alpha - c_2)(c_\alpha - c_3)K_{32_\alpha}K_{23_\alpha}.$$

Here, α is the primary (2,3) wave and 1,2 and 3 indicate the spherical harmonics (1,2), (1,4) and (3,4), respectively.

The roots of (40) have been calculated for different values of ζ_α as a function of ζ_1^0. The maximum growth rates are displayed in Fig. 12.

For small amplitudes of the (2,3) wave, the peaks of maximum growth rate occur at the resonance points for both triads, which are indicated by arrows. For larger amplitudes of the (2,3) wave both peaks display a shift with respect to the point of resonance although the shift of the peak due to resonance of the triad formed with the (1,2) and (1,4) wave is hardly noticeable. The shift of the other peak is similar as the shift noticed in the T13 model. The effect of increasing the number of components beyond four on the stability of the (2,3) wave is thus rather small.

In the remaining part of this section we will consider the case that $F > 0$. Because the frequencies of the normal modes depend on F (not shown), the position of the resonant peaks also depends on F. For $F = 2.75$, resonance with the "(1,2)", "(3,4)" components occurs at ζ_1^0 -0.042 and 0.244, and with the "(1,2)", "(1,4)" components at $\zeta_1^0 = -0.56$ and 0.322.

For $F = 2.75$ we have computed the stability properties of a forced stationary "(2,3)" wave for $|\zeta_3^2| = 0.2$ and 0.4. The results are displayed in Fig. (13a, b). The stability analysis has been performed for discrete values of ζ_1^0, starting at $\zeta_1^0 = 0$ and with increments of 0.01. Except for the solid lines, Fig. 13a, b only shows the growth rate of the fastest growing perturbations. Crosses and dots indicate growing perturbations with m odd and m even, respectively.

The two largest peaks in Fig. 13a are due to resonances of the triads formed with the "(1,2)" and "(3,4)" and "(1,2)" and "(1,4)" modes, which are indicated by the arrows a and b, respectively. All the growing modes resulting from these resonance peaks are connected by dashed lines.
It should be remarked that the (1, 2), (3,4) dashed curve cannot be resolved accurately as it is based on only one point. So the maximum may be somewhat larger than the computed value.

Comparing with the case for $F = 0$, we notice that the large peak due to resonance of the triad formed with the (1,2) and (1,4) wave has become a factor of 2 smaller. The other resonance peak displays a small increase in amplitude.

The solid line in Fig. 13a represents growing perturbations due to dyad interactions. This curve was computed with increments of ζ_1^0 of 0.002. Arrow c indicates the value of ζ_1^0 for which LSR occurs. The perturbations, having zero frequency, attain their maximum growth rate at $\zeta_1^0 = 0.304$ for which

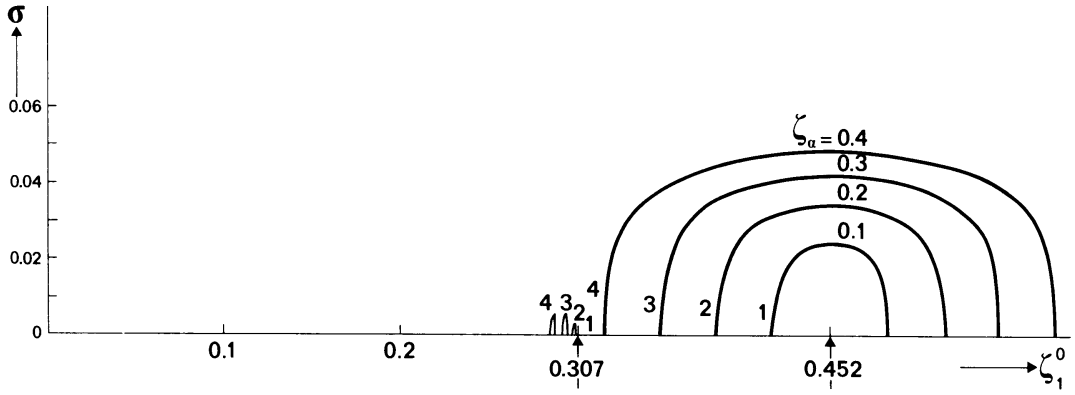

Fig. 12. Analytically computed growth rates for the forced stationary (2,3) wave as a function of ζ_1^0. The growth rates are computed for different amplitudes of the (2,3) wave.

the "(2,3)" mode is stationary. Growing perturbations with smaller growth rates resulting from more complicated interactions occur for values of ζ_1^0 between 0.06 and 0.15.

Increasing the amplitude of the "(2,3)" wave to 0.4, the wave becomes unstable for nearly all values of ζ_1^0 (Fig. 13b). However, the largest peaks are still due to resonant triad interactions and dyad interactions.

Increasing Lamb's parameter induces instability, because of the relaxation of Fjørtoft's theorem. This is best illustrated for the "(1,2)" wave (not shown), which is absolutely stable for F = 0. For F = 2.75 and $|\zeta_2^1| = 0.4$, unstable perturbations exist for certain intervals of ζ_1^0, while for F = 5.5 the "(1,2)" wave is unstable for almost the entire interval of ζ_1^0. Inspection of the growing perturbations shows large contributions from higher zonal and total wavenumbers. The consequence is that for increasing values of Lamb's parameter the effect of truncation becomes more serious, and more components have to be retained in order to adequately describe the stability of planetary waves.

7. Stability of observed flows

In order to investigate the effect of Lamb's parameter on the stability of observed flow patterns, we have numerically computed the stability of the mean winter climatological 400 mb flow. We have used the wind climatology as derived by Oort (1983). From the winds we have computed the streamfunction pattern. The divergence was set to zero and the geopotential computed from the nonlinear balance equation. We performed the calculations for a T13 truncation and treated the climatology as a forced stationary flow pattern.

Figure 14a, b displays the growth rate and frequency of the three fastest growing modes as a function of F. Depending on the particular value of F, different modes have fastest growth rates. For small values of F, mode 1 is the most rapidly growing mode. It has an e-folding time of about 20 days for F = 0, which decreases rapidly with increasing F. The period of this mode increases from 40 days for F = 0 to 50 days for F = 8. Figure 15a displays one-half a period of this mode for F = 0. As would be expected, it has some resemblance to the fastest growing perturbation as found by Simmons et al. (1983) for January 300 mb climatological flow pattern, although the growth rate is much slower. Here we have to remember that we

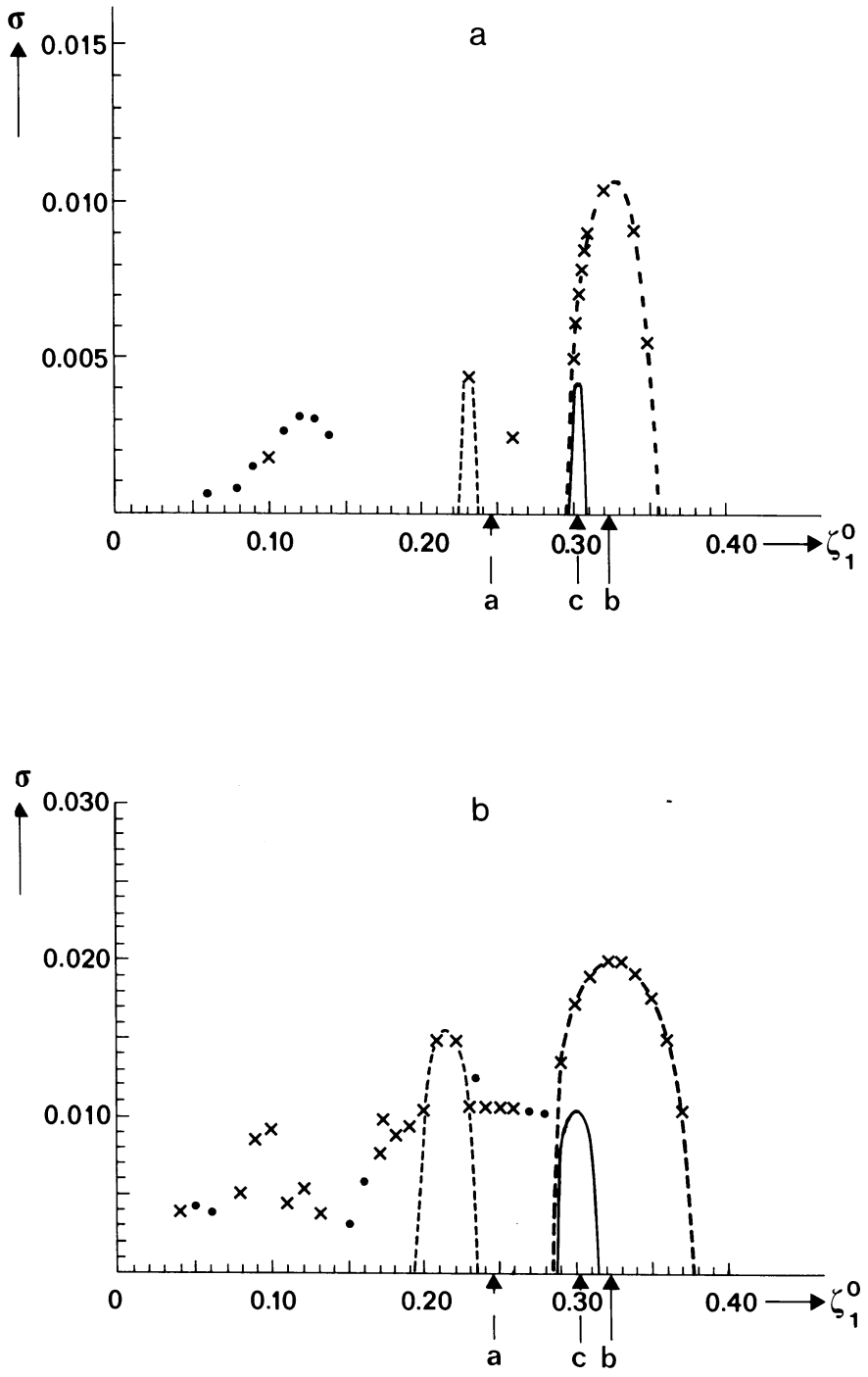

Fig. 13 As in Fig. 11 but for F = 2.75. The crosses and dots denote growing perturbations with m odd and m even, respectively. The dashed and solid line indicate the growing perturbations due to triad and dyad interactions, respectively; LSR is indicated by the arrow c.

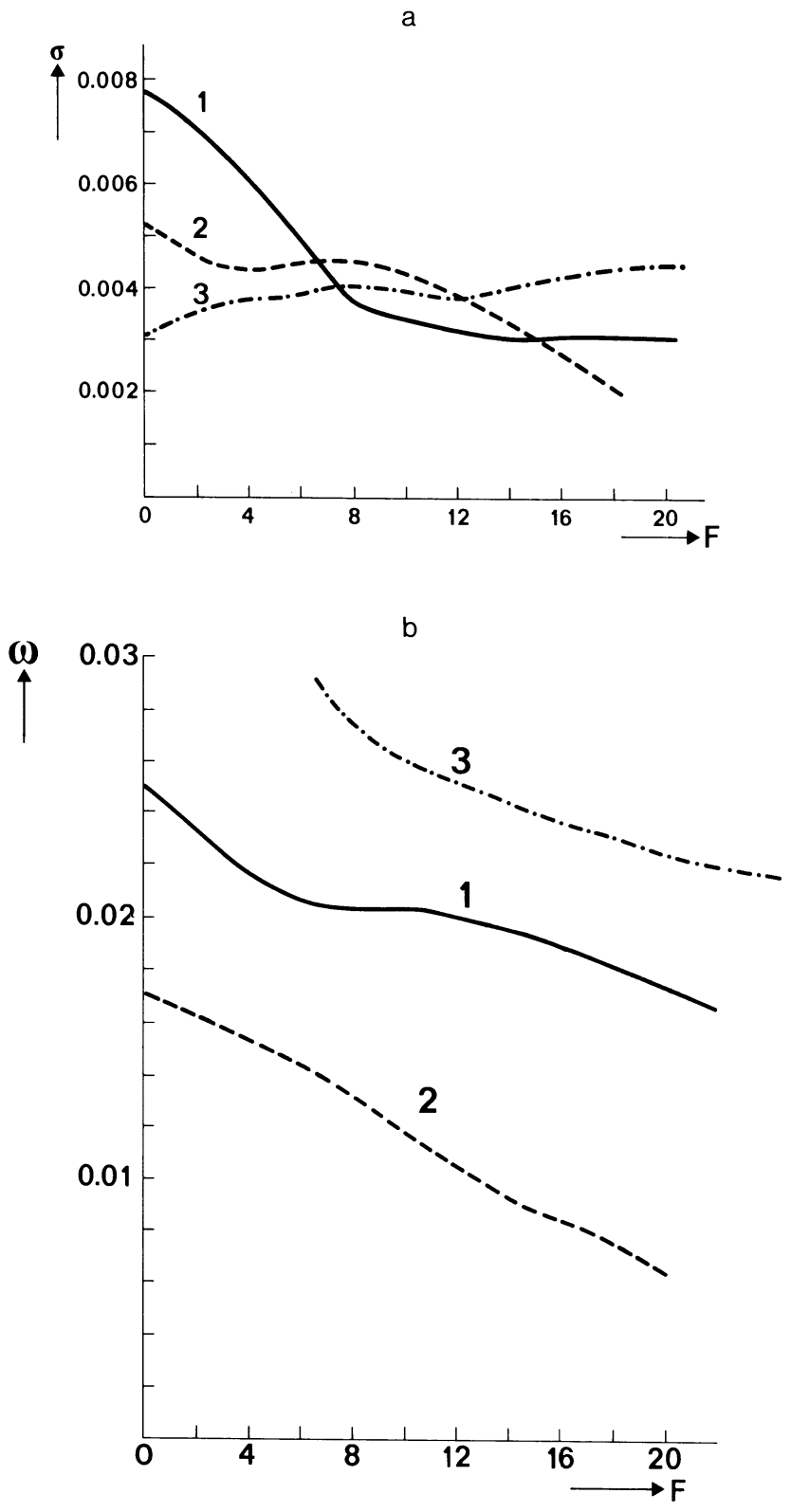

Fig. 14. Growth rate (a) and frequency (b) of the three most rapidly growing perturbations for the observed 400 mb winter climatology flow as a function of F.

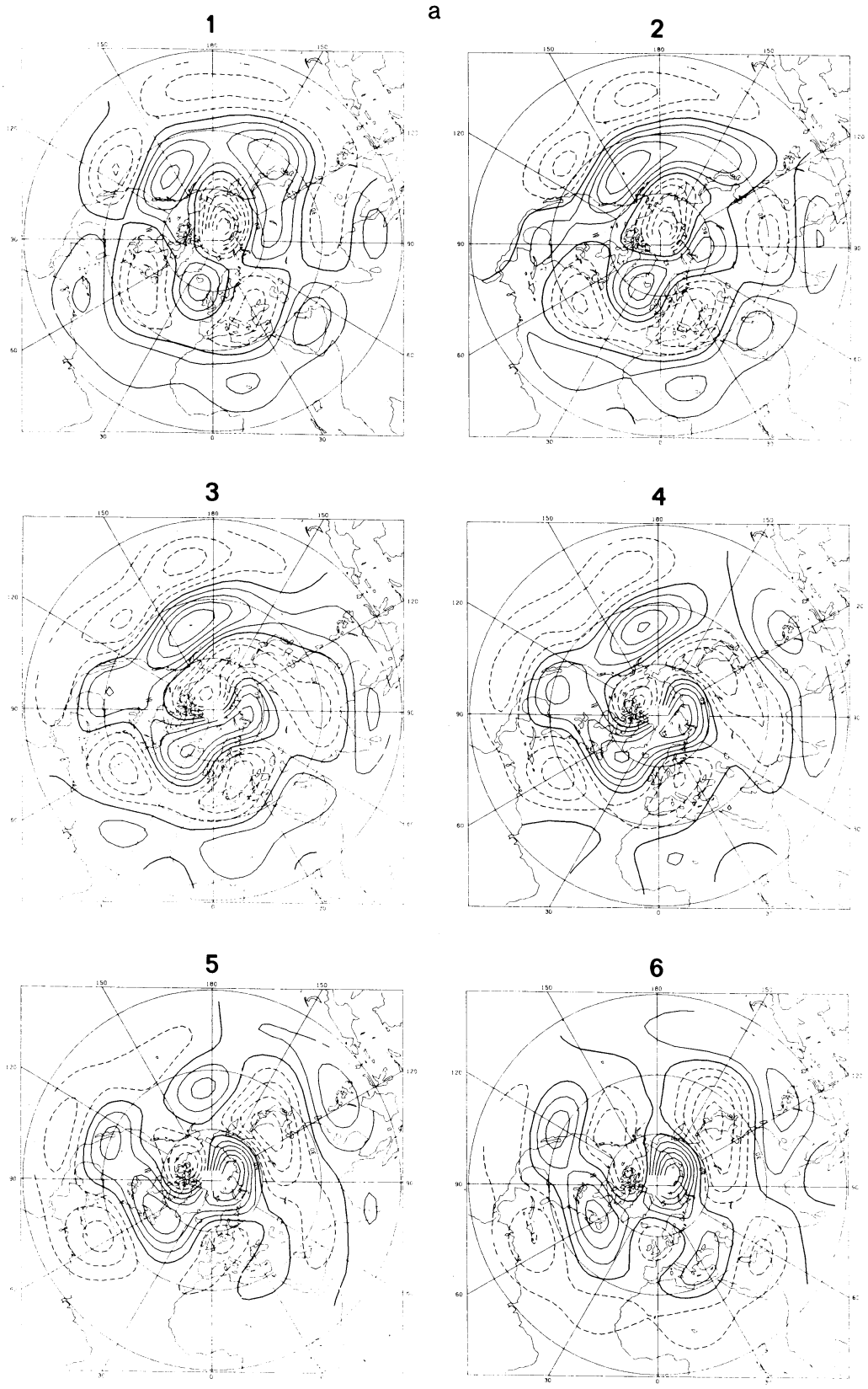

Fig. 15. Streamfunction patterns of the most rapidly growing perturbations for the observed 400 mb winter climatology for F = 0 (a) and F = 8 (b). Shown is one-half a period. The difference between two succesive streamfunction plots is 1/12 of a full period.

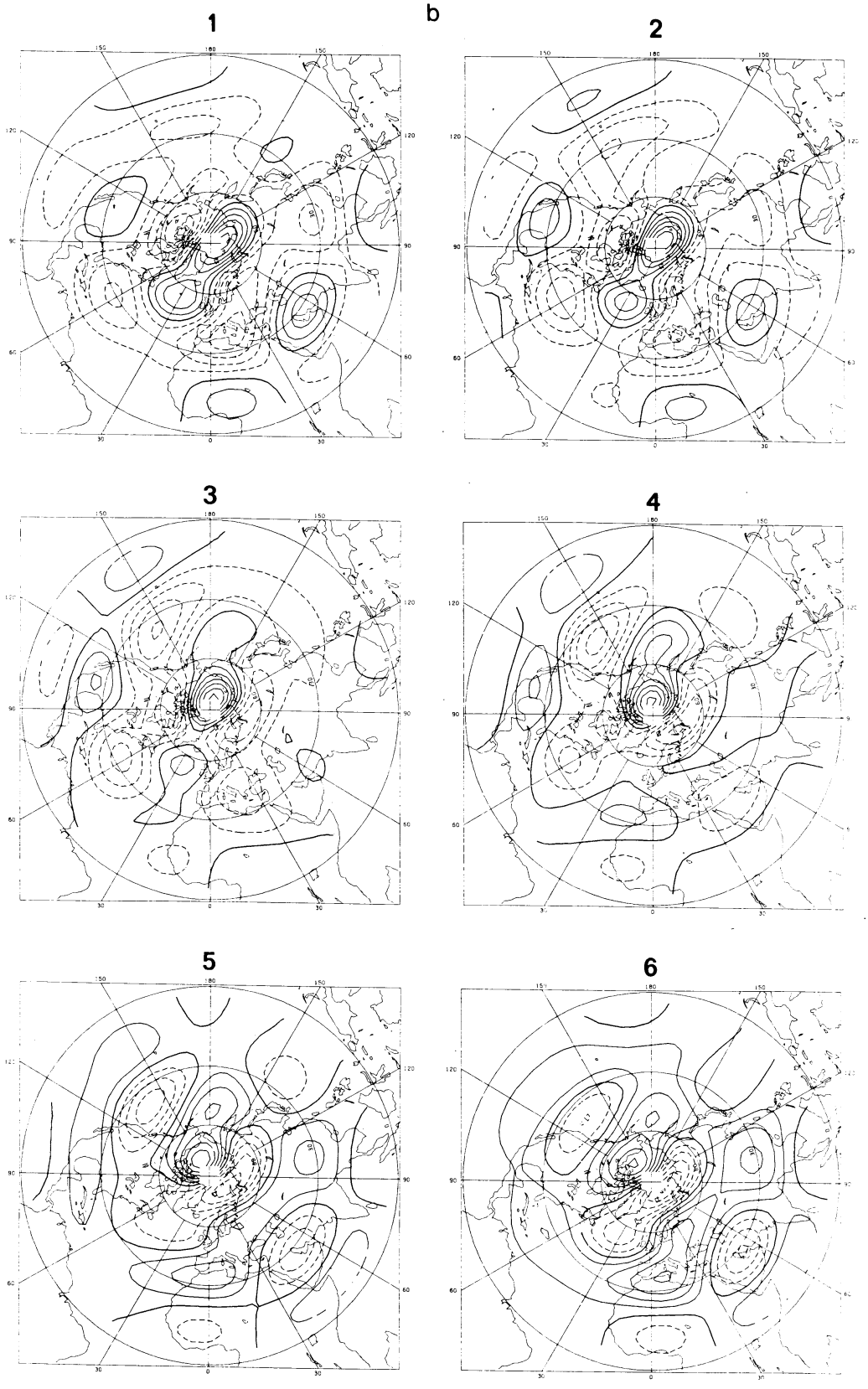

Fig. 15 (Continued)

have used a 400 mb climatology that is likely to be less unstable. Apart from that, the results may depend on the particular truncation used. Figure 15b displays the fastest growing mode for F = 8 (mode 2). Most of the variability in this mode is concentrated along a ray that runs from 60°E across the north pole to 120°W. It does not have much variability over the central Pacific. The period of this mode is of the order of 100 days. For F > 10, mode 3 (not shown) is the most rapidly growing mode, but it has a rather high frequency.

Our findings for observed flow patterns are in agreement with the results for simple flow configurations. Increasing Lamb's parameter has a profound influence on the stability characteristics of the observed flow. Both the frequency and growth rate of the perturbations decrease for increasing values of F. The decrease in growth rate is not uniform for all perturbations. As a consequence, we find different modes with fastest growth rates in different ranges of F.

8. Conclusions

The stability of simple planetary scale solutions of the shallow-water equations was analyzed for small values of F. Increasing F results in smaller critical amplitudes but growth rate and phase speed of the perturbations decrease with increasing F. A linear stability analysis of the mean winter climatological 400 mb flow showed the same dependence on F.

Instability of simple planetary-scale flows often occurs within one triad, which is the triad closest to resonance. This most efficient triad approach applies to the instability of simple zonal flows but only for physically realistic values of the amplitudes. In the area of marginal instability it fails because many modes are needed in order to describe the structure of the perturbation across the critical line. For very large values of the amplitude, the most efficient triad approach again fails. The reason for this is not clear. Accordingly, a description of the instability process of free and forced planetary waves within one triad applies only for realistic values of the amplitudes of the waves and not for very large values.

By considering a single triad it is easy to understand why the stability of forced stationary waves superimposed on a zonal flow is so sensitive to the strength of the zonal flow. Variation of the zonal flow strongly affects the resonance conditions and thus the stability of the triads. If we generalize this picture to the atmosphere, where the low wavenumber spectrum is dominated by stationary waves forced by combined orographic and diabatic forcing, sudden changes in the amplitudes of these waves could be explained by small variations of the zonal mean flow. If F is increased, the values of zonal flows for which the growing perturbations display maximum growth rates change and, as was the case with free waves, the growth rates become smaller.

When $F > 0$, the normal modes (Hough functions) are no longer exact solutions of the nonlinear shallow-water equations and they will naturally decay. Outside the domain of self-resonance, the rate of decay is small with respect to the time scale of barotropic instability. In case of self-resonance, the decay can be described by dyad interactions and occurs on the same time scale as barotropic instability. Within this range a conventional stability analysis of Hough modes has to be interpreted in terms of the sensitivity of the evolution of the flow pattern to initial errors.

Acknowledgements

The authors wish to thank H. Tennekes, W. Verkley, J. Verhaar and R. Mureau for their valuable comments. We also like to thank Mrs. B. Kok for typing the manuscript.

9. References

Baines, P.G., 1976: The stability of planetary waves on a sphere. J. Fluid Mech., 73, 193-213.

Bourke, W., 1972: An efficient, one-level, primitive equation spectral model. Mon. Wea. Rev., 100, 683-689.

Boyd, J.P., 1983a: Long wave/short wave resonance in equatorial waves. J. Phys. Oceanogr., 13, 450-458.

Boyd, J.P., 1983b: Second harmonic resonance for equatorial waves. J. Phys. Oceanogr., 13, 459-466.

Charney, J.G., 1947: The dynamics of long waves in a baroclinic westerly event. J. Meteor., 4, 135-163.

Eady, E.T., 1949: Long waves and cyclone waves. Tellus, 1, 33-52.

Fjørtoft, R., 1953: On the changes in the spectral distribution of kinetic energy for two dimensional , nodivergent flow. Tellus, 5, 225-230.

Frederiksen, J.S., 1983a: Disturbances and eddy fluxes in Northern Hemisphere flows: Instability of three-dimensional January and July flows. J. Atmos. Sci., 40, 836-855.

Frederiksen, J.S., 1983b: A unified three-dimensional instability theory of the onset of blocking and cyclogenesis. II Teleconnection patterns. J. Atmos. Sci., 40, 2593-2609.

Gill, A.E., 1974: The stability of planetary waves. Geophys. Fluid Dyn., 6, 29-47.

Holton, J.R., 1972: An Introduction to Dynamic Meteorology. Academic Press, 319 pp.

Horel, J.D. and J.M. Wallace, 1981: Planetary-scale atmospheric phenomena associated with the Southern Oscillation. Mon. Wea. Rev., 109, 813-829.

Hoskins, B.J., 1973: Stability of Rossby-Haurwitz wave. Quart. Journ. Rev., 99, 723-745.

Kasahara, A., 1976: Normal modes of ultralong waves in the atmosphere. Mon. Wea. Rev. 104, 669-690.

Kuo, H.L., 1949: Dynamic instability of two-dimensional non-divergent flow in a barotropic atmosphere. J. Meteorol., 6, 105-122.

Lim, H., and C.P. Chang, 1983: Dynamics of teleconnection and Walker circulations forced by equatorial heating. J. Atmos. Sci., 40, 1897-1915.

Longuet-Higgins, M.S., 1968: The eigenfunctions of Laplace's tidal equations over a sphere. Proc. R. Soc., London, Ser. A, 262, 511-607.

Lorenz, E.N., 1972: Barotropic instability of Rossby wave motion. J. Atmos. Sci. 29, 258-264.

Matsuno, T., 1966: Quasi-geostrophic motions in the equatorial area. J. Meteorol. Soc. Jpn., 44, 25-43.

Oort, A.H., 1983: Global Atmospheric circulation statistics, 1958-1973, NOAA, Professional paper 14.

Platzman, G.W., 1962: The analytical dynamics of the spectral vorticity equation. J. Atmos. Sci., 19, 313-328.

Ripa, P., 1981: On the theory of nonlinear interactions among geophysical waves. J. Fluid Mech., 103, 87-115.

Ripa, P., 1982: Nonlinear wave-wave interactions in one-layer reduced gravity model on the equatorial beta-plane. J. Phys. Oceanogr., 12, 97-111.

Ripa, P., 1983a: General stability conditions for zonal flows in a one-layer model on the β-plane or the sphere. J. Fluid Mech., 126, 463-489.

Ripa, P., 1983b: Weak interactions of Equatorial Waves in a one-layer model. Part I: General properties. J. Phys. Oceanogr., 13, 1208-1226.

Ripa, P., 1983c: Weak interactions of Equatorial Waves in a one-layer model. Part II: Applications. J. Phys. Oceanogr. 13, 1227-1240.

Simmons, A.J., J.M. Wallace, and G.W. Branstator, 1983: Barotropic wave propagation and instability, and atmospheric teleconnection patterns. J. Atmos. Sci., 40, 1363-1392.

Wallace, J.M., and D.S. Gutzler, 1981: Teleconnection in the geopotential height field during the Northern Hemisphere winter. Mon. Wea. Rev., 109, 785-812.

Chapter III

BIFURCATIONS IN A BAROTROPIC LOW-ORDER MODEL WITH SELF-INTERACTION*

ABSTRACT

For finite equivalent depth, the shallow-water equations (SWE) exhibit instabilities based on dyad interactions. This process is called self-interaction. In the present paper we investigate how the stationary states of a low-order spectral model based on the SWE on the sphere are affected by self-interaction. This is done by computing the bifurcation diagram for increasing strength of the forcing in one of the vorticity components. The instabilities occurring in this low-order system are topographic instability and self-interaction. Self-interaction generates saddle-node as well as Hopf bifurcations, resulting in multiple steady-states and limit cycles. For large values of the forcing self-interaction significantly affects the steady-state curve originating from topographic instability. Extrapolating these results to the real atmosphere, self-interaction may influence the atmosphere's nonlinear behavior.

* Submitted to Journal of Atmospheric Sciences with J.D. Opsteegh as co-author

1. Introduction

In Haarsma and Opsteegh (1988) (Chapter II of this thesis) the stability properties of the shallow-water equations (SWE) were investigated. In that paper we demonstrated the existence of an instability mechanism, called self-interaction, which originates from dyad interactions. For infinite equivalent depth ($H_e \rightarrow \infty$), in which case the SWE reduce to the barotropic vorticity equation (BVE), this instability process vanishes.

In their pioneering study Charney and DeVore (1979) demonstrated the existence of multiple steady states due to saddle-node bifurcations in a low-order model containing topographic instability only. Since then many studies have been devoted to the analysis of nonlinear low-order models in which various types of instability occur. Topographic instability was combined with either baroclinic instability (Charney and Straus, 1980; Reinhold and Pierrehumbert, 1982) or barotropic instability (Legras and Ghil, 1985; Källén, 1981).

In this paper we combine topographic instability with self-interaction. We are interested in the following two questions: What type of bifurcations occur in a model with self-interaction only and what is the effect of self-interaction on the bifurcation diagram that originates from topographic instability? The latter question is inspired by studies of Reinhold and Pierrehumbert (1982) and others, who showed that the bifurcation diagram due to a single instability mechanism can be drastically changed when a new instability mechanism is introduced. In Haarsma and Opsteegh (1988) we discussed the relevance of the SWE for the large-scale low-frequency motion in the atmosphere. The SWE describe the horizontal structure of a stratified flow, like the atmosphere, only when nonlinear advection is small. So they are probably too simple to study all aspects of the lower frequencies in the atmosphere. Nevertheless the choice of a finite equivalent depth is probably more realistic than simply assuming that $H_e \rightarrow \infty$, in which case the SWE reduce to the frequently studied BVE. If this is true, then self-interaction might be an important instability mechanism for the large-scale low-frequency motion in the atmosphere.

In section 2 we describe the low-order spectral model. A summary of self-interaction is presented in section 3. In section 4 we present the bifurcation diagram when self-interaction is the only instability mechanism. The bifurcation diagram when topographic instability and self-interac-

tion are combined is discussed in section 5, followed by the conclusions and a discussion of the results in section 6.

2. Model

The nondimensional SWE on a rotating sphere, including forcing, dissipation and topography are given by:

$$\frac{\partial \zeta}{\partial t} = - \vec{v}.\nabla(\zeta + f) - (\zeta + f)D + G_f - \varepsilon\zeta, \tag{1a}$$

$$\frac{\partial D}{\partial t} = - \nabla^2(\phi + \frac{\vec{V}.\vec{V}}{2}) - \nabla.[\vec{k}x\vec{V}(\zeta + f)] - \varepsilon D, \tag{1b}$$

$$\frac{\partial \phi}{\partial t} = - \vec{V}.\nabla(\phi - \phi_h) - (\phi - \phi_h)D - \frac{D}{F}, \tag{1c}$$

where ζ, D and ϕ are the relative vorticity, horizontal divergence and perturbation geopotential respectively, ϕ_h is the geopotential of the topography, f the planetary vorticity, $\vec{V}$ is the horizontal velocity field, $\vec{k}$ the vertical unit vector and G_f the vorticity forcing. The vorticity as well as the divergence equation contain a Rayleigh friction term with friction parameter ε.

The nondimensional variables involved in (1a - 1c) are defined as follows:

$$\zeta = \zeta^*/\Omega;\ D = D^*/\Omega;\ \phi = \phi^*/a^2\Omega^2;\ t = t^*\Omega;\ f = f^*/\Omega, \tag{2}$$

where a and Ω are the radius and angular velocity of the earth respectively. The asterisks denote the dimensional variables. The only nondimensional parameter in (1) is Lamb's parameter:

$$F = \frac{a^2\Omega^2}{gH_e}, \tag{3}$$

where H_e is the equivalent depth and g is gravity. As shown in Haarsma and Opsteegh (1988) the SWE reduce to the BVE in the limit $F \to 0$.

For convenience we rewrite (1c) as:

$$\frac{\partial \phi}{\partial t} = - \vec{V}.\nabla(\phi - \frac{\eta}{F}) - \phi D - (1 - \eta)\frac{D}{F}, \qquad (1d)$$

where $\eta = \phi_h^* / (gH_e)$ is the topography scaled by the equivalent depth.

We express the variables of (1) in a series of spherical harmonics. The expansion is truncated at a certain wavenumber, thereby reducing the set of three partial differential equations to a finite set of 3N ordinary differential equations, where N is the number of spectral components retained in the truncation. We have only considered the asymmetric components in the vorticity and the symmetric components in the divergence and geopotential, thereby excluding cross equatorial flow. The special form of truncation we have chosen in the different experiments will be outlined in the discussion of each experiment. For all experiments the Rayleigh friction ε is $1.90\ 10^{-6}\ s^{-1}$, which corresponds to an e-folding time of 6 days.

3. Self-interaction

In this section we will give a short review of self-interaction. A more extensive treatment can be found in Boyd (1983a,b) and in Haarsma and Opsteegh (1988). The normal modes of the SWE are Hough functions (Longuet-Higgins, 1968). For F = 0, they reduce to spherical harmonics, which are the normal modes of the BVE. The spherical harmonics are exact solutions of the nonlinear BVE, but for F > 0 the normal modes of the linear SWE are not exact solutions of the nonlinear SWE. So they decay without the necessity of being perturbed. The decay is such that a single Hough mode γ generates a secondary Hough mode β. This is called self-interaction.

In general self-interaction is weak and the decay of a Hough mode is slow compared to the decay rates resulting from barotropic instability by wave triads. So Hough modes can be considered approximate solutions of the nonlinear SWE. However when the phase speed of the primary Hough mode equals that of its secondary mode, the decay into that mode is fast. This is called self-resonance.

We distinguish two types of self-resonance:

1. Second Harmonic Resonance: occurs when the phase speed of the primary wave with zonal wave number m_y equals that of its second harmonic component ($2m_y$)
2. Long wave/short wave resonance: occurs for stationary primary Hough modes. They decay into zonal flow components.

4. Bifurcations due to self-interaction

In this section we investigate what type of bifurcations occur due to self-interaction. We choose F = 2.75, which corresponds to an equivalent depth of 8.10^3 m for the atmosphere. The restriction to self-interaction can be accomplished by choosing a spectral truncation that excludes barotropic instability by triad interactions. Such a choice is possible because of Fjørtoft's theorem (1953). This theorem states that there can be no energy and enstrophy transport in one direction of the wave spectrum. Therefore the only unstable triads are those satisfying the following inequality for total wave number n:

$$n_\alpha < n_\gamma < n_\beta, \tag{4}$$

where the subscript γ denotes the primary wave and α and β the perturbations. The spectral truncation used in this section is shown in Fig. 1. The crosses indicate the vorticity components, whereas the divergence and geopotential are denoted by circles. The modes retained in this spectral truncation are the zonal modes "(0,1)" and "(0,3)", and the wave modes "(2,3)" and "(2,5)". Because of (4), barotropic instability is impossible for these modes. The only possible type of self-resonance is longwave/shortwave resonance, which occurs when the "(2,3)" or the "(2,5)" mode becomes stationary resulting in resonant decay into the zonal flow. Second harmonic resonance is impossible because of the absence of modes with m = 4.

The vorticity equation (1a) is forced in the (0,1) and (2,3) component:

$$G_f = \zeta_1^{0\,*} P_1^0(\lambda,\mu) + \zeta_3^{2\,*} P_3^2(\lambda,\mu). \tag{5}$$

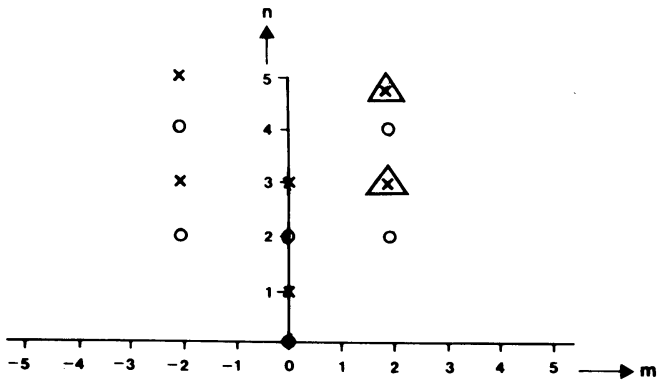

Fig. 1 Spectral truncation of the SWE.
The vorticity components are indicated by crosses, the divergence and geopotential components by circles. The topography is denoted by a triangle.

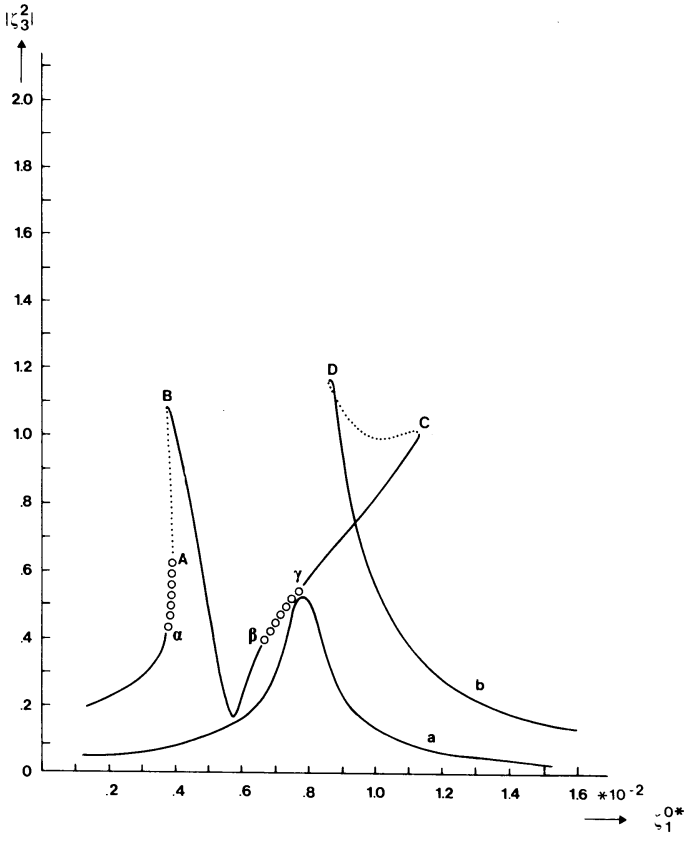

Fig. 2 Projection of the steady state curves on $|\zeta_3^2|$ for $\zeta_3^{2*} = 0.7\ 10^{-2}$ (curve a) and $\zeta_3^{2*} = 2.8\ 10^{-2}$ (curve b). F = 2.75. Dots indicate unstable steady states with a positive real eigenvalue. Unstable steady states possessing a pair of complex conjugated eigenvalues with a positive real part are denoted by a circle.

Here $P_n^m(\lambda,\mu)$ is the associated Legendre polynomial, where λ is longitude, $\mu = \sin\phi$ and ϕ is latitude. The coefficient ζ_n^{m*} denotes the strength of the forcing in the (m,n) component. The steady states were computed at the prescribed value of ε (friction) for increasing ζ_1^{0*}, keeping ζ_3^{2*} at a fixed value. This was done for $\zeta_3^{2*} = 0.7\ 10^{-2}$ and $\zeta_3^{2*} = 2.8\ 10^{-2}$. These values correspond with a maximum vorticity forcing at 35°N of $0.37\ 10^{-12}\ s^{-2}$ and $1.48\ 10^{-12}\ s^{-2}$ respectively. We will denote these two wave forcings as weak and strong wave forcing respectively. For the computation of steady states we used the pseudo-arclength method as described by Legras and Ghil (1985) and Haarsma and Opsteegh (1989) (Chapter IV of this thesis).

Figure 2 displays the projection of the steady-state curves on the (2,3) vorticity component for weak wave forcing (curve a) and strong wave forcing (curve b). The weak wave forcing curve shows a peak at $\zeta_1^{0*} = 0.78\ 10^{-2}$. For this value of ζ_1^{0*} the strength of the (0,1) component in the solution is 0.30. This is the value for which the "(2,3)" mode becomes stationary, resulting in resonant excitation of this mode by the wave forcing ζ_3^{2*}. The (0,3) component (not shown) of all computed steady states remains very small ($< 0.3\ 10^{-2}$), the energy transfer from the "(2,3)" mode to the zonal modes due to self-interaction is balanced by the dissipation. Bifurcations do not occur for weak wave forcing; all computed steady states are stable.

The results for strong wave forcing (curve b of Figure 2) show significant differences with those for weak wave forcing. The projection of the steady-state curve on the (2,3) vorticity component now displays two peaks instead of one. Both peaks are folded, resulting in multiple steady states for ζ_1^{0*} between $0.37\ 10^{-2}$ and $0.39\ 10^{-2}$ and between $0.86\ 10^{-2}$ and $1.13\ 10^{-2}$. In contrast with the weak forcing case the (0,3) component (not shown) now attains a considerable amplitude with maxima in the order of 0.6.

At the turning points (points A, B, C and D) a saddle-node bifurcation occurs, where a real eigenvalue changes sign. The steady states at the returning branches of the curve (between A and B, and C and D) are unstable, possessing a single positive real eigenvalue. The stationary growing perturbations display contributions from the zonal as well as the wave components.

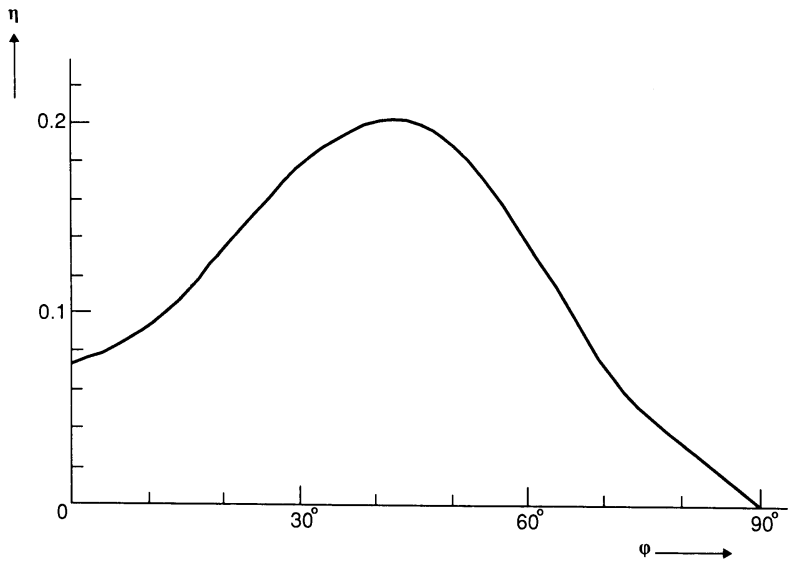

Fig. 3 Meridional structure of the topography.

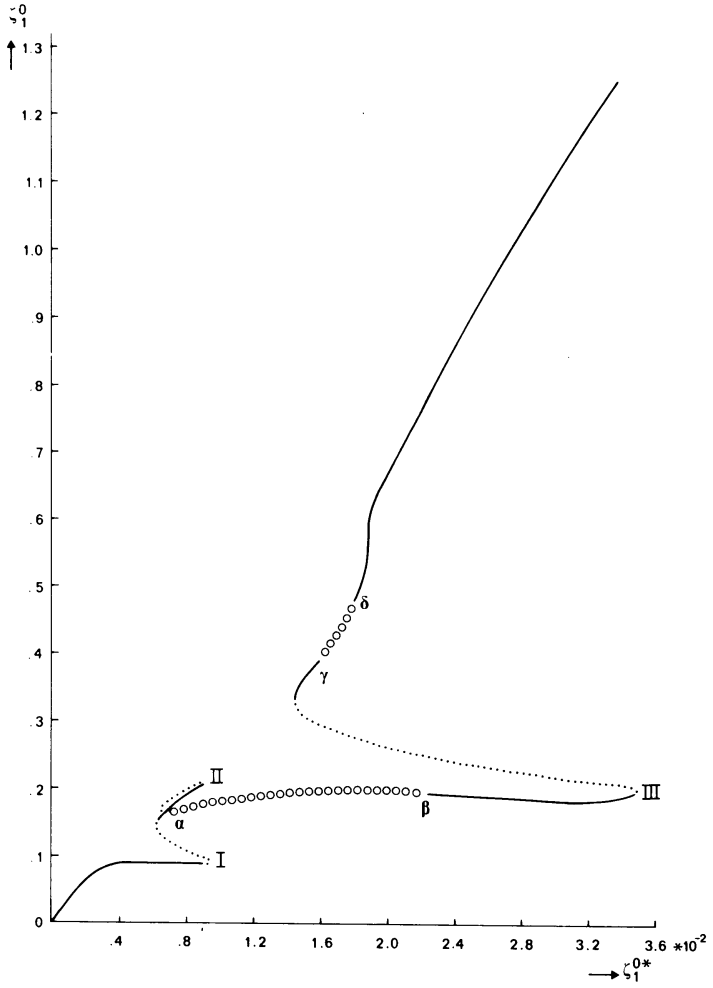

Fig. 4 Projection of the computed steady state curve on ζ_1^0 for $F = 10^{-5}$. The meaning of the symbols indicating the stability of the steady states is the same as in Fig. 2.

Hopf bifurcations, which occur when a pair of complex conjugated eigenvalues crosses the imaginary axis, show up at the points α, β, γ and A. At point A the Hopf and saddle-node bifurcation coalesce: The complex conjugated eigenvalue with positive real part at the interval between α and A becomes identically zero at A and changes into the purely positive real eigenvalue at the interval between A and B. Like the growing perturbations due to the saddle-node bifurcations, the limit cycles due to the Hopf bifurcations display contributions from the zonal as well as the wave components.

These results demonstrate, that like topographic-, barotropic- and baroclinic instability, self-interaction is able to generate saddle-node and Hopf bifurcations.

5. Bifurcations in a model with topographic instability and self-interaction

In this section we investigate how the introduction of self-interaction affects the bifurcation diagram that originates from topographic instability. First, in 5.1, we compute the steady states for a model with topographic instability only. Subsequently we compute in 5.2 the steady states when self-interaction is added. In that section we also present an analysis of the observed differences between the steady-state curves of these two experiments.

5.1 Topographic Instability

In order to exclude self-interaction, we set F at a very small value ($F = 10^{-5}$). The spectral truncation is the same as used in the previous experiment. The topography is represented by the (2,2) and (2,4) components. They are indicated by triangles in Fig. 1. We choose $\eta_2^2 = 0.122$ and $\eta_4^2 = 0.077$. This results in a mountain with zonal wave number two and a meridional structure such as depicted in Fig. 3. The maximum amplitude of η is 0.2, which is attained at 43°N. The possible interactions between the topography and the wave components are given below:

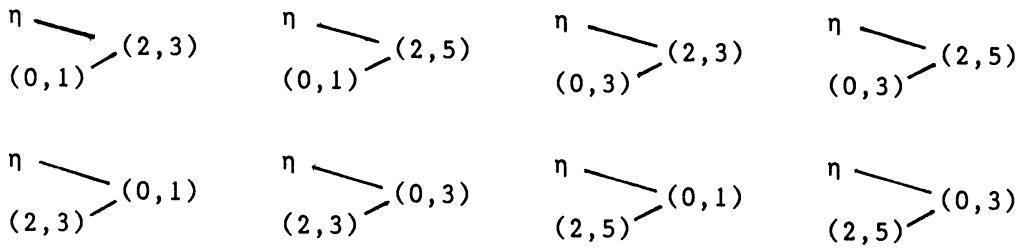

Due to the topography energy flows from the zonal into the wave components and vice versa.

In contrast to the previous experiment with self-interaction, the vorticity equation (1a) is only forced in the (0,1) component:

$$G_f = \zeta_1^{0*} P_1^0(\lambda,\mu). \tag{6}$$

No forcing is applied at the (2,3) component. The wave modes are solely excited by interaction of the zonal flow with the topography. We have computed the steady states for increasing ζ_1^{0*}. The projection of the steady-state curve on the (0,1) component of the vorticity is shown in Fig. 4. It displays a number of turning points or saddle-node bifurcations. The three saddle-node bifurcations where the steady-state curve returns are indicated by I, II and III. The returning branches of the curve are unstable, possessing a single positive real eigenvalue. Due to the folds in the steady-state curve, at least three steady states exist simultaneously between $\zeta_1^{0*} = 1.54\ 10^{-2}$ and $\zeta_1^{0*} = 3.48\ 10^{-2}$ and five between $\zeta_1^{0*} = 0.64\ 10^{-2}$ and $\zeta_1^{0*} = 0.90\ 10^{-2}$. The amplitudes of the (2,3) and (2,5) component (not shown) display local maxima at II and I respectively, whereas both components attain their absolute maximum close to III. At this point both components are approximately 90° out of phase with the topography, resulting in a large form drag. For ζ_1^{0*} larger than $1.9\ 10^{-2}$, beyond the last fold in the steady-state curve, both components are approximately in phase with the topography. For these states the form drag is small, and consequently an increment of ζ_1^{0*} mainly results in an increment of ζ_1^0.

Hopf bifurcations are observed after the second and third fold at $\zeta_1^{0*} = 0.71\ 10^{-2}$ (point α) and $\zeta_1^{0*} = 1.63\ 10^{-2}$ (point γ), resulting in growing perturbations between α and β, and γ and δ.

5.2 Topographic instability and self-interaction

In order to allow self-interaction we now choose F = 2.75, and repeat the experiment of the foregoing section. We will refer to the experiment with F = 2.75 as B and to the experiment of the previous section as A.

The projection of the steady-state curve on the (0,1) vorticity component is displayed in Fig. 5. Comparison with the steady-state curve for experiment A (Fig. 4) shows that for ζ_1^{0*} smaller than $1.3\ 10^{-2}$ both curves are very similar to each other. This is also the case for the (2,3) and (2,5) components (not shown). The bifurcations I and II occur for approximately the same values of ζ_1^{0*}. Significant differences exist for larger values of ζ_1^{0*}. In B, bifurcation III occurs for a much smaller value of ζ_1^{0*} ($1.32\ 10^{-2}$). The peaks in the (2,3) and (2,5) components at this bifurcation point are also much smaller than in experiment A. Apparently at larger values of ζ_1^{0*} self-interaction facilitates the formation of bifurcations due to topographic instability, by transferring topographically induced wave energy back into the zonal flow component. For still larger values of ζ_1^{0*} a completely new fold in the steady-state curve appears due to a saddle-node bifurcation at $\zeta_1^{0*} = 2.0\ 10^{-2}$ (IV).

The Hopf bifurcation in experiment A, after the second fold disappears, whereas the Hopf bifurcation after the third fold now occurs at $\zeta_1^{0*} = 0.95\ 10^{-2}$ (point γ) resulting in growing perturbations for ζ_1^{0*} between $0.95\ 10^{-2}$ and $1.13\ 10^{-2}$ (point δ).

The introduction of self-interaction thus causes significant changes in the steady-state curve of experiment A. In order to investigate the relative contribution cf both topographic instability and self-interaction for each of the bifurcations in the new steady-state curve, we performed a stability analysis of the steady states for the linearized equations without the topographic term. The result is shown in Fig. 6. The steady states on the returning branches of bifurcation I and III are all stable, while the states on the returning branch of II are only partially unstable, displaying much smaller growth rates than the original ones. From this we conclude that all these three bifurcations originate from topographic instability. The topographic origin of the first two bifurcations is in agreement with the already observed fact that the steady-state curve for small ζ_1^{0*} is very similar to the one in experiment A, which allows only topographic instability. Also the third bifurcation, although significantly

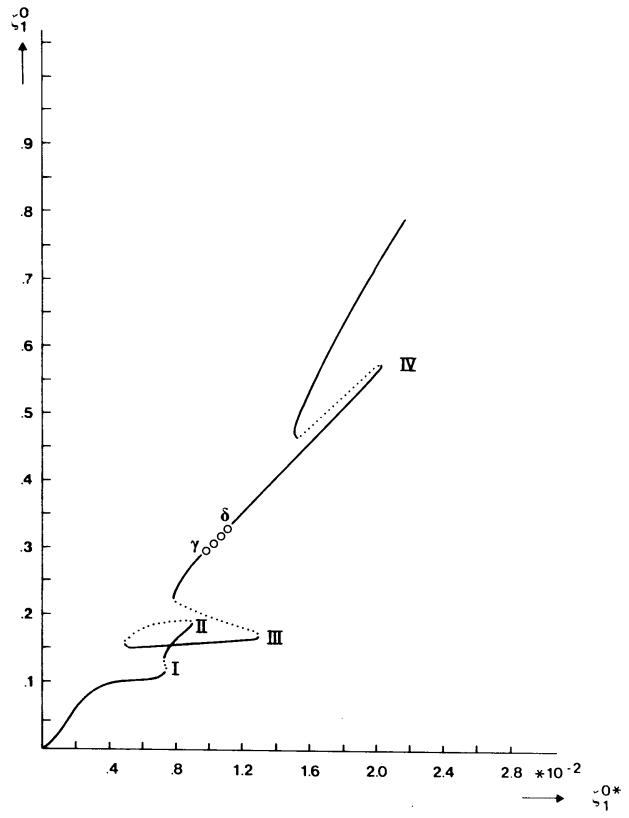

Fig. 5 As Fig. 4, but now for F = 2.75.

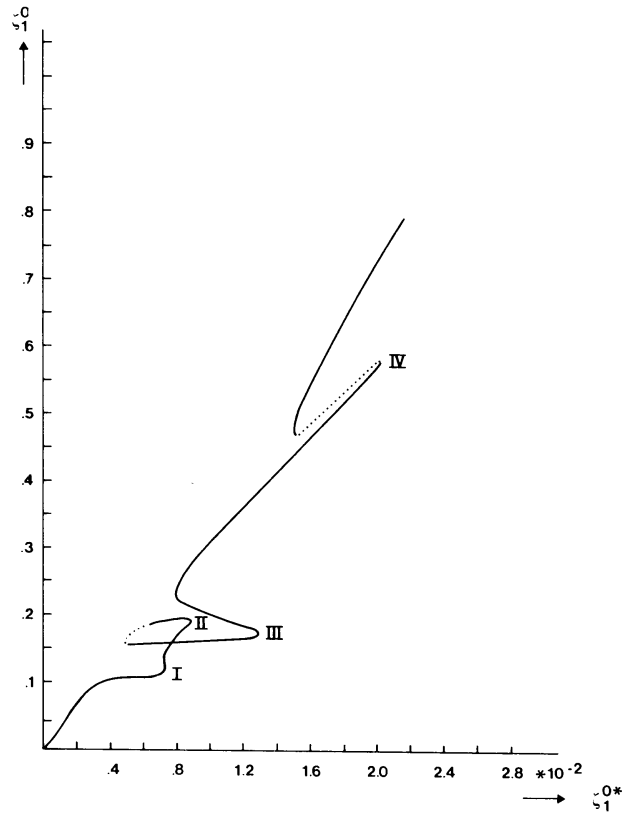

Fig. 6 As Fig. 4. Shown is the stability of the steady states when the topographic forcing is removed.

modified by self-interaction, still originates from topographic instability. The growth rates on the returning branch of bifurcation IV hardly change when the topographic term is removed. This new bifurcation is thus entirely caused by self-interaction. Fig. 6 also shows that the Hopf bifurcation beyond III at $\zeta_1^{0*} = 0.95\ 10^{-2}$ has disappeared when the topographic term is removed, revealing that the origin of this bifurcation is topographic instability.

In order to obtain a better understanding of the origin of the bifurcations and the changes in the steady-state curve due to the introduction of self-interaction, we will use Pedlosky's (1981) analysis of topographic instability. In the analysis of Pedlosky, which is valid when $\eta^{1/3} << 1$, the structure of the topographically forced wave is approximately equal to that of a free wave. The nonlinear interactions only determine the amplitude of the wave. The saddle-node bifurcation where the steady-state curve retuns, occurs when the zonal flow is slightly stronger than the zonal flow for which the free wave is stationary (super resonant flow) (Figs. 1 and 2 of his paper). In Pedlosky's analysis the zonal flow is only in second order affected by the nonlinear interactions. In our experiment, where $\eta = 0.2$, the forced zonal flow component is strongly modified by interactions; the amplitude of the (0,3) component is comparable to that of the (0,1) component. Despite the strong nonlinearities, we will try to interprete our results in terms of his analysis.

We computed the frequency ω of the eigenmodes of the zonal symmetric part of the computed steady states. The structure of the eigenmodes changes constantly along the steady-state curve, but they can always be identified. For the BVE in solid body rotation they reduce to the spherical harmonics (2,5) and (2,3). In the following we shall denote these modes as mode 1 and mod 2 respectively. Fig. 7a displays for experiment A ($F = 10^{-5}$) the frequencies of mode 1 (curve a) and mode 2 (curve b) as a function of the (0,1) vorticity component of the computed steady states. The arrows I, II and III indicate the position of the saddle-node bifurcations where the steady-state curve returns. Mode 1 becomes stationary for $\zeta_1^0 = 0.093$, which is somewhat smaller than 0.095 for which the first saddle-node bifurcation occurs.

In agreement with the analysis of Pedlosky this saddle-node bifurcation thus occurs for slightly super resonant flow. This mode is also stationary for $\zeta_1^0 = 0.175$ and $\zeta_1^0 = 0.192$. Again these values are somewhat smaller than

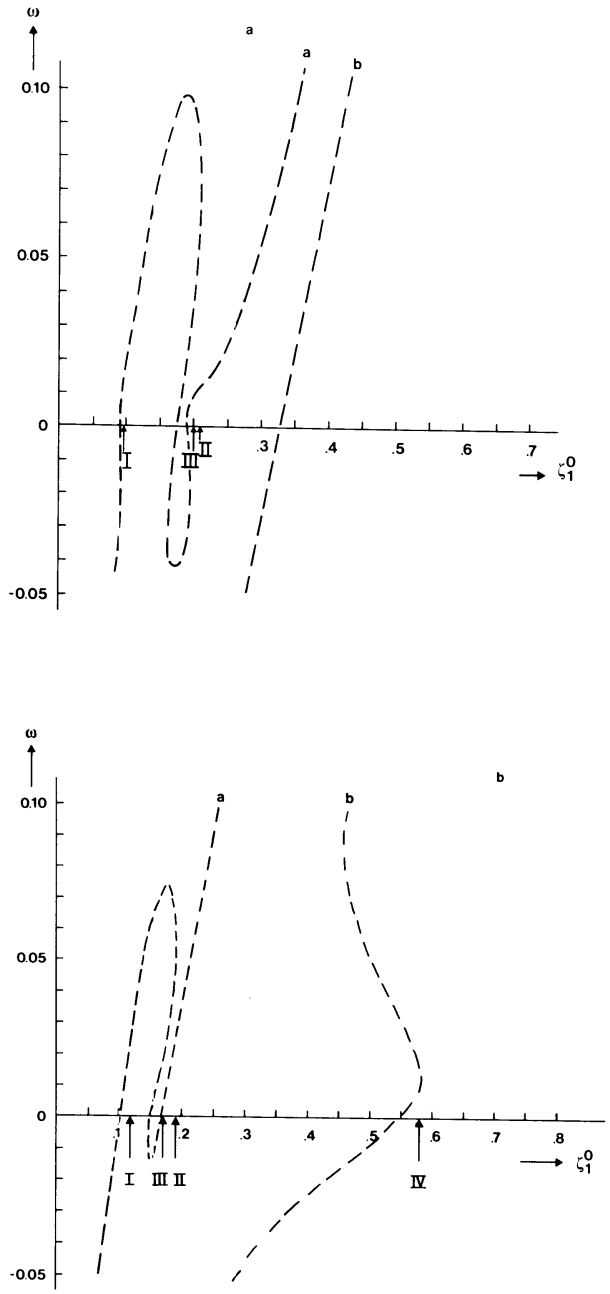

Fig. 7 Frequencies of the modes of the zonal symmetric part of the computed steady states for $F = 10^{-5}$ (a) and $F = 2.75$ (b). The frequencies are displayed as a function of ζ_1^0 of the computed steady states. The arrows indicate the bifurcations where the steady state curve returns.

the values of ζ_1^0 for which the other two saddle-node bifurcations occur: $\zeta_1^0 = 0.209$ (II) and $\zeta_1^0 = 0.200$ (III). It follows that all three bifurcations in the steady-state curve occur when mode 1 is super resonant. Mode 2 is stationary for $\zeta_1^0 = 0.327$. However, the steady-state curve does not show a corresponding fold due to saddle-node bifurcations. Apparently in this case the Rayleigh friction is too strong in comparison with the topographic forcing for bifurcations to occur.

The frequencies of the two modes for experiment B are displayed in Fig. 7b. Similarly as for experiment A the first three bifurcations in the steady-state curve, which originate from topographic instability, are connected to super resonance of mode 1. The values ζ_1^0 for which this mode becomes stationary i.e. 0.104, 0.153 and 0.167 are approximately the same as in experiment A.

The new bifurcation (IV) occurs at $\zeta_1^0 = 0.578$, which is somewhat larger than the value for which mode 2 becomes stationary ($\zeta_1^0 = 0.545$). In contrast to experiment A, the introduction of self-interaction thus causes a saddle-node bifurcation when mode 2 is super resonant.

Compared to experiment A, mode 2 becomes stationary for a much larger value of ζ_1^0. Also, the frequency of this mode does not show a linear increment with ζ_1^0. Instead the curve displays a bent close to the point where the mode is stationary. Self-interaction thus strongly influences the frequency of mode 2. This is caused by the fact that self-interaction is causing a large feedback of wave energy into the (0,3) component of the zonal flow, thereby altering the frequency and structure of the eigenmodes of this zonal flow. Fig. 8, displaying the projection of the steady-state curve on the (0,3) vorticity component for experiment A and B, clearly shows the large differences in the amplitude between A and B. In experiment A the ζ_3^0 component decreases rapidly after bifurcation III, whereas in experiment B, this component increases monotonously with ζ_1^{0*} until bifurcation IV. For large values of ζ_1^{0*} self-interaction thus completely changes the distribution of energy between zonal and wave components. Moreover, Fig. 8 shows that in both experiments the value of ζ_3^0 is approximately the same for the first three bifurcations. This is also the case for the (0,1) component (Fig. 7). The reduction in ζ_1^{0*} for which bifurcation III occurs, is thus connected to the smaller amplitudes of the wave modes. As discussed before, this reduction is caused by self-interaction which makes excitation of large wave modes impossible.

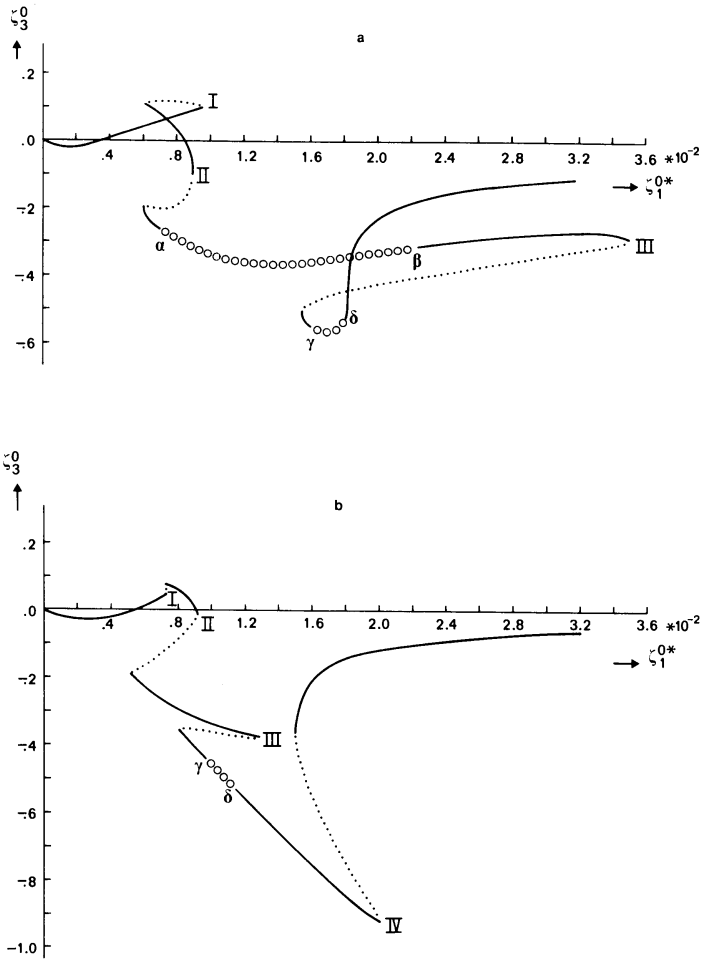

Fig. 8 Projection of the computed steady-state curve on ζ_3^0 for F = 10^{-5} (a) and F = 2.75 (b).

Summarizing we state that for small ζ_1^{0*} self-resonance does not significantly affects the steady-state curve originating from topographic instability. For larger values of ζ_1^{0*} (>1.3 10^{-2}), self-interaction significantly reduces the value of ζ_1^{0*} for which bifurcation III occurs. A new bifurcation, entirely caused by self-interaction, emerges for still larger values of ζ_1^{0*}. In agreement with the quasi-linear theory of Pedlosky we demonstrated that, although in our experiment the flow patterns cannot strictly be considered as quasi-linear, saddle-node bifurcations due to topographic instability as well as self-interaction occur when the zonal flow is slightly super resonant.

6. Conclusions and discussions

The shallow-water equations including topography contain three instability mechanisms, i.e.: topographic instability, barotropic instability and self-interaction. In Haarsma and Opsteegh (1988) the last two instability mechnisms were investigated. There it was shown that they can be described by triad and dyad interactions respectively and that the critical amplitudes for instability as well as the growth rate and frequency of the growing perturbations depend on Lamb's parameter F. For F = 0, in which case the shallow-water equations reduce to the barotropic vorticity equation, self-interaction is impossible.

The effect of topographic instability on the bifurcation diagram was first studied by Charney and DeVore (1979). For a low-order model they demonstrated the possibility of saddle-node bifurcations due to topographic instability. Others have studied the effect of barotropic instability (Källén, 1981; Legras and Ghil, 1985) and baroclinic instability (Charney and Straus, 1980; Reinhold and Pierrehumbert, 1982).

Following these studies we have investigated what kind of bifurcations can be generated in a low-order model with self-interaction. We demonstrated that like the other instability mechanisms self-interaction generates saddle-node as well as Hopf bifurcations.

We next investigated how the introduction of self-interaction affects the bifurcation diagram which originates from topographic instability. For small ζ_1^{0*} self-interaction does not significantly affect the steady-state curve originating from topographic instability. Significant changes appear

for ζ_1^{o*} larger than 1.3 10^{-2}. In absence of topography this value of ζ_1^{o*} would result in a zonal flow of about 100 ms^{-1} at midlatitude. For the atmosphere this is an unrealistically large value. Whether or not self-interaction is important for the real atmosphere is still unclear. This can only be answered by investigating more realistic models of the atmosphere.

7. References

Boyd, J.P., 1983a: Long wave/short wave response in equatorial waves. J. Phys. Oceanogr., 13, 450-458.

Boyd, J.P., 1983b: Second harmonic resonance for equatorial waves. J. Phys. Oceanogr., 13, 459-466.

Charney, J.G. and J.G. DeVore, 1979: Multiple flow equilibria in the atmosphere and blocking. J. Atmos. Sci., 36, 1205-1216.

Charney, J.G. and D.M. Straus, 1980: Form-drag instability, multiple equilibria and propagating planetary waves in baroclinic orographically forced planetary wave systems. J. Atmos. Sci., 37, 1157-1176.

Fjørtoft, R., 1953: On the changes in the spectral distribution of kinetic energy for two dimensional, nondivergent flow. Tellus, 5, 225-230.

Haarsma, R.J. and J.D. Opsteegh, 1988: Barotropic instability of planetary-scale flows. J. Atmos. Sci., 45, 2789-3016.

Haarsma, R.J. and J.D. Opsteegh, 1989: Nonlinear response to anomalous tropical forcing. Submitted to J. Atmos. Sci.

Källén, E., 1981: The nonlinear effects of orographic and momentum forcing in a low-order barotropic model. J. Atmos. Sci., 38, 2150-2163.

Legras, B. and M. Ghil, 1985: Persistent anomalies, blocking and variations in atmospheric predictability. J. Atmos. Sci., 42, 433-471.

Longuet-Higgins, M.S., 1968: The eigenfunctions of Laplace's tidal equations over a sphere. Proc. R. Soc., London, Ser. A., 262, 511-607.

Pedlosky, J., 1981: Resonant topographic waves in barotropic and baroclinic flows. J. Atmos. Sci., 38, 2626-2641.

Reinhold, B.B. and R.T. Pierrehumbert, 1982: Dynamics of weather regimes: Quasi-stationary waves and blocking. Mon. Wea. Rev., 110, 1105-1145.

Chapter IV

NONLINEAR RESPONSE TO ANOMALOUS TROPICAL FORCING*

Abstract

We have investigated the nonlinear steady-state response of a barotropic model to an estimate of the observed anomalous tropical divergence forcing for the El-Niño winter of 1982/83. The 400 mb climatological flow was made a forced solution of the model by adding a relaxation forcing. The Rayleigh friction coefficient (ε = 20 days^{-1}) was chosen such that this solution is marginally stable. The steady states were computed as a function of a dimensionless parameter α, that governs the strength of the anomalous forcing. The computed steady-state curve deviates markedly from a straight line, displaying a fold and an isolated branch. The linear steady-state response pattern ($\alpha << 1$) compares well with the observed pattern. After the fold at α = 0.65, the agreement is smaller. A further increase in α after the fold results in saturation of the response. The streamfunction patterns of the isolated branch display unrealistic large amplitudes.

Time integrations show that the steady states govern the time dependent behavior despite their unstable nature. The resulting time-mean patterns are very similar to the steady states. Periodic, quasi-periodic and complete chaotic behavior are all three observed.

Increasing the Rayleigh friction coefficient to ε = 10 days^{-1} results in a disappearence of the fold as well as the isolated branch. Like for ε = 20 days^{-1}, the agreement between the steady-state response and the observed pattern decreases when α is increased. From these results we conclude that the atmospheric response to even a very strong El-Niño event like the one in 1982/83 is approximately linear.

*Submitted to Journal of Atmospheric Sciences with J.D. Opsteegh as co-author.

1. Introduction

The impact of the release of tropical latent heat for extratropical anomalies on time scales longer than a few weeks was suggested first by Bjerknes (1966). The results of recent experiments with linear steady-state models supported Bjerknes' ideas (Opsteegh and Van den Dool, 1980; Webster, 1982). Hoskins and Karoly (1981) provided a theoretical explanation for these teleconnections in terms of dispersion of Rossby waves from the tropics into the middle latitudes. From observations Horel and Wallace (1981) found that the occurrence of the Pacific North America (PNA) pattern in the Pacific was related to El-Niño years. More recent studies with General Circulation Models (GCM's) (Geisler et al., 1985; Blackmon et al., 1983; Kang and Lau, 1986) and observational studies (Mo and Livezey, 1986; Lau and Boyle, 1987) confirmed the relation between tropical forcing and large-scale low-frequency anomalies in the extratropics.

Concerning the role of transients in generating extratropical anomalies there is less agreement. Budget calculations indicate that the contributions from transients are small (Sardeshmukh and Hoskins, 1985; Lau and Boyle, 1987). However, several investigators have pointed out, using model simulations, that despite the smallness of these terms they can significantly modify and strengthen the observed midlatitude anomalies (Kok and Opsteegh, 1985; Kang and Held, 1986).

The contribution of the barotropic instability of planetary waves to the explanation of persistent extratropical anomalies was discussed by Simmons et al. (1983). Using a model based on the barotropic vorticity equation, they showed that the fastest growing mode of the unstable climatological time-mean flow could be linked to observed teleconnection patterns. A similar result was obtained by Frederiksen (1983) with a multilevel model. He found that the structure, growth rate and frequency of the fastest growing perturbations are primarily dependent on the static stability parameter. These ideas were supported by Geisler et al. (1985) and Branstator (1985), who showed that certain anomaly patterns are generated by a variety of tropical forcings, indicating the existence of barotropically unstable modes.

Another approach was followed by Reinhold and Pierrehumbert (1982) and Legras and Ghil (1985), who investigated simplified nonlinear models of the atmosphere and demonstrated that in the chaotic domain these models exhibit

regime-like behavior. In experiments with GCM's (Manabe and Hahn, 1981; Lau, 1981) persistent large-scale anomalies from the time-mean circulation occur when the boundary forcing is kept constant. These studies suggest that in order to fully explain low-frequency variability in the atmosphere one has to consider the nonlinear interaction among the planetary waves. Sardeshmukh and Hoskins (1985) explicitly computed the contributions from the nonlinear terms in the vorticity budget for the El-Niño winter of 1982/83. They showed that the nonlinearities in the advection and stretching terms contribute significantly to the vorticity budget. Following the suggestions of Sardeshmukh and Hoskins the main goal of this paper is to analyse the importance of the nonlinear terms for the extratropical response to a tropical forcing.

Within a linear framework, Branstator (1985) demonstrated that the wave pattern in the climatological basic state affects the steady-state response to anomalous forcing. By including zonally asymmetric components in the basic state of a linear model he showed that it is possible to qualitatively simulate the time-mean response of a GCM to a tropical SST anomaly. Model simulations that include the nonlinear interactions among the planetary waves, such as those performed by Lau and Lim (1984), Sardeshmukh and Hoskins (1985), Kang and Held (1986), Hendon (1986) and Held and Kang (1987), all show that the nonlinear response to tropical forcing is in qualitative agreement with the predictions of linear theory. In these studies the major effect of the nonlinearities is to modify the structure and amplitude of the stationary waves, while the position of highs and lows remains relatively unaffected.

In the above mentioned studies the nonlinear response is computed by performing time integrations. In addition to these studies we have computed nonlinear steady states of the barotropic vorticity equation (BVE) in response to a climatological relaxation forcing and an anomalous tropical forcing. The steady states are computed as a function of a non-dimensional parameter α which determines the strength of the anomalous forcing. By computing the steady states when α is increased from zero to one we get a gradual transition from linear to nonlinear solutions. The stability of the computed steady states is numerically evaluated. We next investigated the relevance of these (unstable) steady states for the time-mean patterns derived from time integrations.

The relaxation forcing was determined such that the climatological 400 mb winter flow is a forced solution when the anomalous forcing is absent. The value of the Rayleigh friction coefficient is chosen such that this solution is marginally stable. We computed the steady states (varying α from 0 to 1) for the observed anomalous tropical forcing occurring during the El-Niño winter of 1982/83. The forcing was computed by estimating the anomalous topical divergence from the observed anomalies in outgoing long wave radiation (OLR). Time integrations were performed for several values of α. Next we omitted the relative vorticity in the stretching term, which makes the divergence forcing independent of the solution. By doing so we were able to distinguish the separate effects of the nonlinearities in the advection and in the stretching term. As our choice for the value of the Rayleigh friction coefficient is considered to be quite low, we also investigated the sensitivity of the solutions to an increase in the friction parameter.

Sections 2 and 3 of this paper deal with the model equations and the method for the computations of steady states. In section 4 we present the steady-state curves, while in section 5 we investigate the relevance of these steady states for the dynamics of the system by performing time integrations. The effect of the relative vorticity in the stretching term and the sensitivity of the results to an increase in the Rayleigh friction are treated in sections 6 and 7 respectively, followed by the conclusions and a discussion of the results in section 8.

2. Model Equations

We study solutions of the barotropic vorticity equation with forcing and dissipation:

$$\frac{\partial \zeta}{\partial t} + J(\psi, \zeta + f) + \varepsilon\zeta = F, \tag{1}$$

where ζ and f are the relative and planetary vorticity, ψ the streamfunction, J the Jacobian operator, ε is the Rayleigh friction parameter, and F the forcing. We apply this equation at the 400 mb level. The forcing is computed from an estimate of the time-mean divergence D at that level:

$$F = -(\zeta + f)D. \tag{2}$$

We split F into a climatological part F_c and a perturbation part $\hat{F}$. The climatological forcing is prescribed in such a way that the observed climatological winter flow ζ_c is a stationary solution. The anomalous divergence $\hat{D}$ is taken to be zero in middle latitudes. In the tropics we assume that there is a balance between diabatic heating and adiabatic cooling by upward motion: $\sigma\omega = -Q/c_p$. Using this balance and the continuity equation $\nabla.\vec{V} = -\partial\omega/\partial p$, the perturbation divergence term $\hat{D}$ in the troppics can be expressed in terms of the anomalous tropical diabatic heating $\hat{Q}$:

$$\hat{D} = \frac{\partial}{\partial p}(\hat{Q}/\sigma c_p). \tag{3}$$

The anomalous divergence term is computed with (3), using an estimate of the vertical distribution of $\hat{Q}$, from observed OLR data. We have computed the forced stationary solutions of (1) in response to the total forcing, i.e. climatological relaxation forcing plus anomalous forcing.

The resulting equation is thus given by:

$$\frac{\partial\zeta}{\partial t} + J(\psi,\zeta + f) + \varepsilon\zeta = - \alpha(\zeta + f)\hat{D} + F_c, \tag{4}$$

where $\hat{D}$ is the anomalous divergence in the tropics and F_c the climatological relaxation forcing:

$$F_c = J(\psi_c,\zeta_c + f) + \varepsilon\zeta_c. \tag{5}$$

The coefficient α in equation (4) governs the strength of the anomalous forcing. It will be varied from a very small value (10^{-5}) to 1.5. Rewritting (4) with the aid of (5) results in a nonlinear equation for the vorticity anomaly $\hat{\zeta} = \zeta - \zeta_c$:

$$\underset{(a)}{\frac{\partial\hat{\zeta}}{\partial t}} + \underset{(a)}{J(\psi_c,\hat{\zeta})} + \underset{(b)}{J(\hat{\psi},\zeta_c + f)} + \underset{(c)}{J(\hat{\psi},\hat{\zeta})} + \underset{(d)}{\varepsilon\hat{\zeta}} = \underset{(e)}{-\alpha(\zeta_c + \hat{\zeta} + f)\hat{D}}. \tag{6}$$

The terms (a) and (b) are the advection of anomalous relative vorticity by the climatological mean wind and the advection of climatological absolute vorticity by the anomalous wind respectively. Term (c) describes the nonlinear interactions among the perturbations, (d) is the Rayleigh friction term and (e) the anomalous tropical forcing respectively. If $\alpha << 1$ then

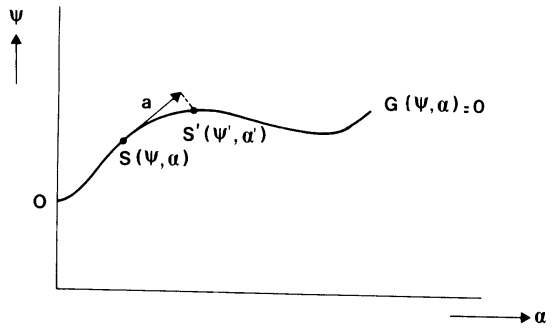

Fig. 1. Schematic picture of the pseudo-arclength method for the computation of steady states.

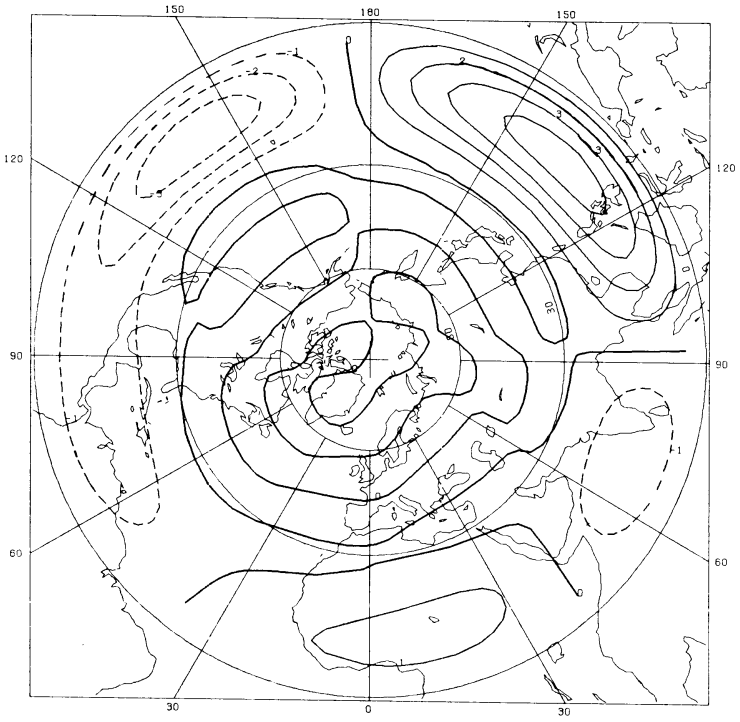

Fig. 2. The anomalous solution independent part of the tropical divergence forcing $-f\hat{D}$ at 400 mb for the winter of 1982/83. The contour interval is 10^{-11} s^{-2}.

the anomalous response is small, consequently the quadratic term (c) can be neglected; (6) then becomes linear. It must be emphasized that the anomalous divergence is prescribed, but that the anomalous forcing is dependent on the solution due to the term $\hat{\zeta}\hat{D}$.

The computations are performed with a hemispheric spectral version of (4) truncated at T13.

3. Computation of steady states

The steady states of (4) are computed using the pseudo arc-length method of Keller (1978). This method is also used and described by Legras and Ghil (1985). The pseudo-arclength method is illustrated in Fig. 1. In this figure ψ is the n-dimensional state vector of the model and α the coefficient, that determines the strength of the anomalous forcing term. C is the steady-state curve for which

$$\frac{\partial \psi}{\partial t} = G(\psi,\alpha) = 0 \qquad (7)$$

where G is the nonlinear operator. Point 0 represents the zero solution corresponding to zero anomalous forcing. Starting from a known steady state S, corresponding to a particular value of α, we computed a new steady state $S'(\psi',\alpha')$ by linear extrapolation (arrow a in Fig. 1) followed by a Newton-Raphsen interpolation procedure. Using this method, we can compute successive points of the steady-state curve C.

By solving (4) for a range of α-values we investigate the sensitivity of the response to variations in the strength of the anomalous forcing.

The anomalous steady-state responses that are presented have been normalized by $1/\alpha$. In the limit $\alpha \to 0$ the normalized response corresponds to the anomalous linear steady-state response, while for $\alpha = 1$ we have the complete nonlinear response.

The linear stability of each of the steady states is evaluated. The matrix $G_\psi = \partial G/\partial \psi$ is evaluated numerically by forward differences.

$$G_\psi = \{G(\psi + \Delta\psi) - G(\psi)\}/\Delta\psi. \qquad (8)$$

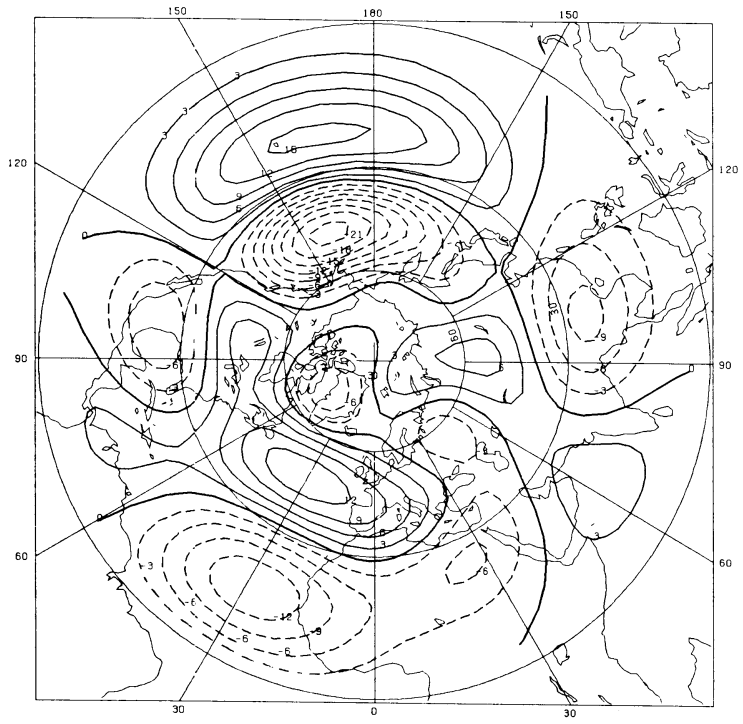

Fig. 3. Observed anomalous 400 mb streamfunction pattern for the winter of 1982-83. The contour interval is 3.10^{-6} m^2s^{-1}. The zonal components are omitted.

4. Simulation of the El-Niño winter of 1982/83

For the computation of the anomalous tropical forcing during the winter of 1982/83, we used the $\hat{Q}$ data from Arkin (1984). Assuming a linear relationship he estimated the vertically integrated $\hat{Q}$ from the anomalous OLR fields. North of 20°N the anomalies in $\hat{Q}$ are assumed to be zero and only the zonal wave numbers 1 to 6 are retained.

If we assume that the vertical scale of the heating is 400 mb and that the mean value of σ is 2.5 10^{-4} Kms^2/k_g, then it follows that a heating of 1 K/day corresponds to a divergence of 10^{-6} s^{-1}. However, this estimate for the divergence is rather uncertain. Kasahara and Da Silva (1986) demonstrated that the excitation of extratropical equivalent barotropic modes by tropical heating occurs through nonlinear coupling of the barotropic modes with the equatorial internal modes, which are directly forced by the tropical heating. The strength of this forcing depends among other things on the vertical shear of the basic state. The results of Kasahara and Da Silva Dias indicate that the magnitude of the divergence forcing may be off by a factor of two. For linear steady-state models some uncertainty in the amplitude of the anomalous forcing is acceptable, because only the amplitude of the response depends on it, while the structure remains unaffected. However, for nonlinear models the amplitude as well as the structure of the response may depend crucially on the amplitude of the anomalous forcing. Therefore it is necessary to investigate the nonlinear response over an interval in α that reflects the uncertainties in the amplitude of the anomalous forcing.

Figure 2 shows our estimate of the solution independent part of the anomalous tropical divergence forcing $(-f\hat{D})$ at 400 mb for the winter of 1982/83. The maximum and minimum over the Pacific correspond with the anomalous Walker circulation with anomalous cooling and heating over Indonesia and the Eastern Pacific respectively. The main effect of $-\zeta_c\hat{D}$ in the anomalous forcing is to counteract $-f\hat{D}$. The amplitude is reduced by about 65 percent. The structure remains relatively unaffected.

For the basic state (ψ_c) we have chosen the mean winter climatological 400 mb flow. We have used the wind climatology as derived by Oort (1983), from which we have computed the streamfunction pattern. Linear stability aanlysis of this pattern reveals that the fastest growing perturbation has an e-folding time of 20 days. By applying linear friction with the same

a

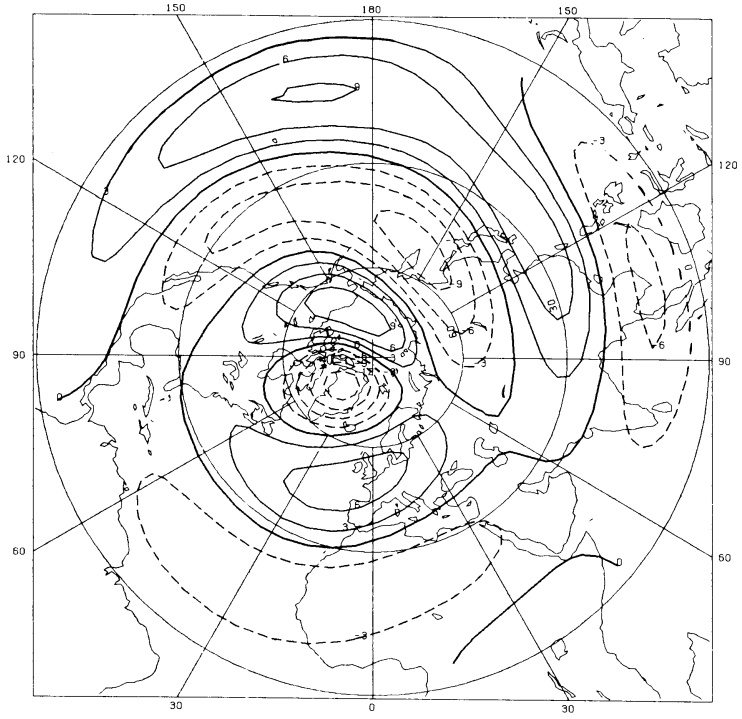

b

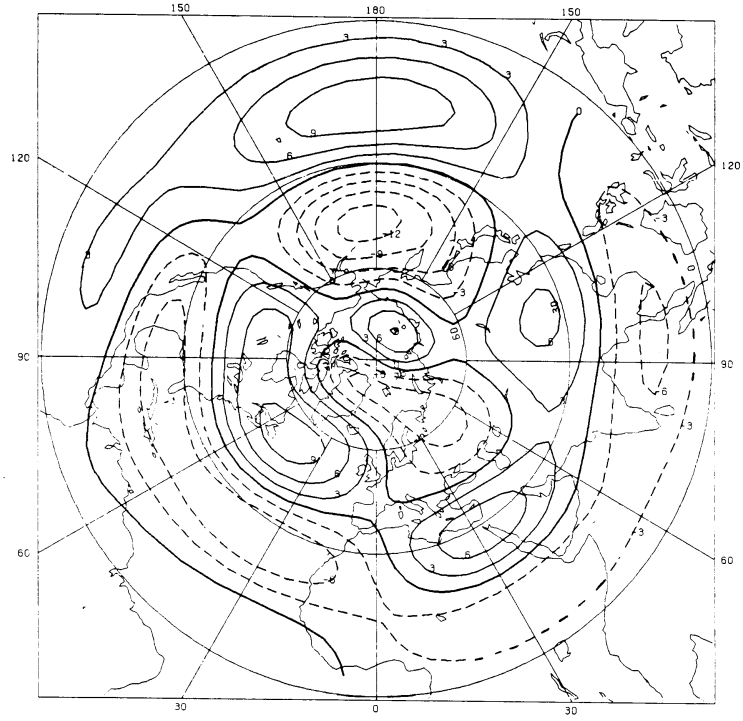

Fig. 4. Simulated anomalous linear ($\alpha = 10^{-5}$) 400 mb streamfunction pattern for the winter of 1982-83. Shown are the patterns for the zonal mean basic state (a) and for the basic state with the wave components included (b). The contour interval is 3.10^{-6} $m^2 s^{-1}$.

e-folding time, the basic state is a marginally stable stationary solution of (4) when $\hat{D}$ is zero. The choice of a marginally basic state is based on the idea that in the real atmsophere instantaneous streamfunction patterns might be unstable, but that the resulting perturbations drive the time-mean climatological flow towards a nearly stable configuration.

The observed anomalies in the 400 mb stream function pattern during the winter of 1982/83 are shown in Fig. 3. In this and subsequent figures, the zonal components in the anomalies have been omitted. This pattern was computed from daily analyses provided by the ECMWF. The most pronounced feature of the anomaly pattern is a strong dipole over the Pacific, which results in increased westerlies near 30°N. A similar weaker dipole, but with reversed sign, is found over the Atlantic.

4.1 Linear response ($\alpha << 1$)

The anomalous linear steady-state response to the observed anomalous forcing is computed by taking $\alpha = 10^{-5}$. Figure 4a shows the normalized (multiplied by $1/\alpha$) response in the streamfunction pattern when only the zonal components of the basic state ψ_c are considered. Comparison with the observed anomaly pattern (Fig. 3) shows that some of the characteristics in the observed pattern can also be found in the simulated pattern. The positive anomaly at 20°N, 165°W is rather well represented, but the negative anomaly north of it is shifted 30° towards the west. Over the Atlantic the dipole is apparent, but somewhat weaker and shifted 15° towards the east. In general, the structure of the anomalies is too elongated in zonal direction. North of 50°N the linear steady-state response is of low quality. The pattern correlation coefficient (pcc) for the whole hemisphere is 0.49. The amplitude of the normalized response is about half of the observed amplitude.

Inclusion of the wave components in the basic state improves the quality of the linear simulation significantly, as shown in Fig. 4b. The position and structure of the anomalies are in better agreement with the observations. The positions of the negative anomaly over the Central Pacific, and the dipole over the Atlantic agree much better with the observed flow. Moreover, at high latitudes the agreement is much better. The improved quality of the linear simulation is revealed by an increase of the pcc from 0.49 to 0.59. These results agree well with those of Branstator (1985).

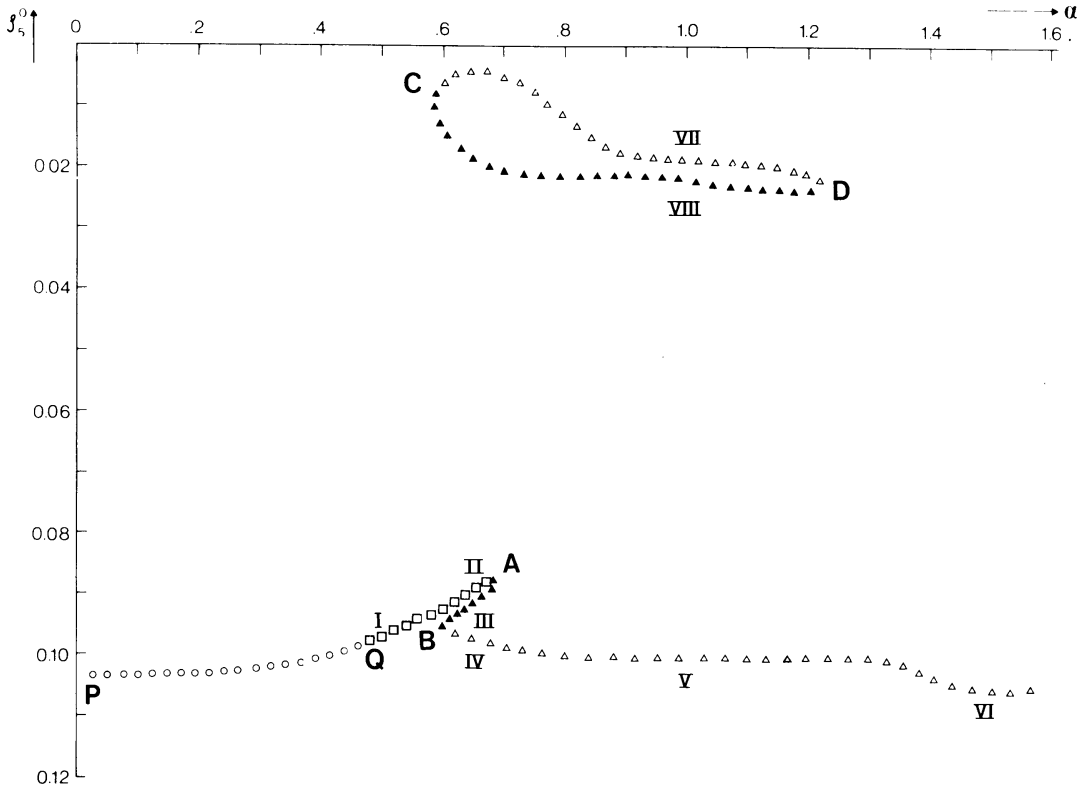

Fig. 5. Projection of the computed steady-state curve on the ζ_5^0 component for the anomalous tropical divergence forcing $-(\zeta + f)\hat{D}$ at 400 mb for the winter of 1982-83.

Symbols indicating the stability properties of the computed steady states:

x: stable

o: one pair of complex conjugated eigenvalues with positive real eigenvalue

□: two pairs of complex conjugated eigenvalues with positive real eigenvalue

Δ: three or more pairs of complex conjugated eigenvalues with positive real eigenvalue.

● o

■ as □ but with the inclusion of one purely real eigenvalue.

▲ Δ

With a linear steady-state model he simulated the anomalous circulation pattern occurring in a GCM due to a tropical SST anomaly. The presence of wave components in the basic state improved the agreement with the anomalies in the GCM considerably.

4.2 Nonlinear response

We computed the steady-states for α between 0 and 1.5. The projection of the computed steady-state curve on the ζ_5^0 component is shown in Fig. 5. By the ζ_n^m component we mean the amplitude of the projection of ζ on the spherical harmonic Y_n^m with zonal wavenumber m and total wavenumber n. This projection is arbitrarely chosen. Its only purpose is to illustrate the bifurcation diagram and to display the stability of the computed steady states. The steady-state curve deviates markedly from a straight line and displays a fold between $\alpha = 0.60$ and 0.69. In addition there exists an isolated branch for α between 0.59 and 1.23. For α just exceeding zero the solution becomes unstable; a pair of complex conjugated eigenvalues crosses the imaginary axis, giving rise to a Hopf bifurcation (point P). At $\alpha = 0.49$ a second Hopf bifurcation occurs (point Q). In general the number of complex conjugated eigenvalues with a positive real part increases for increasing α. The turning points or saddle-node bifurcations in the steady-state curve (points A, B, C and D) correspond with a change of sign of a purely real eigenvalue. All states on the isolated branch are very unstable, possessing eight or more eigenvalues with positive real part.

We will first discuss the anomalous normalized steady-state responses on the main branch. The anomalous normalized streamfunction patterns of the states on the main branch from $\alpha = 0$ up to the first saddle-node bifurcation at $\alpha = 0.69$ differ relatively little from the linear response. Figure 6 shows the streamfunction pattern for $\alpha = 0.50$, indicated by I in Fig. 5, just after the second Hopf bifurcation at $\alpha = 0.49$. The dipole over the Pacific has moved about 15 degrees eastward, in accordance with the observations. The largest differences with the linear solution are between 90°W and 30°E which is the region most remote from the forcing areas. The dipole over the Atlantic has moved westward and the anticyclone over the Middle East is weaker and has shifted toward the west. The cyclone over the North Pacific has intensified. Apart from weakening or intensification of certain highs and lows, the overall normalized amplitude of the response remains the

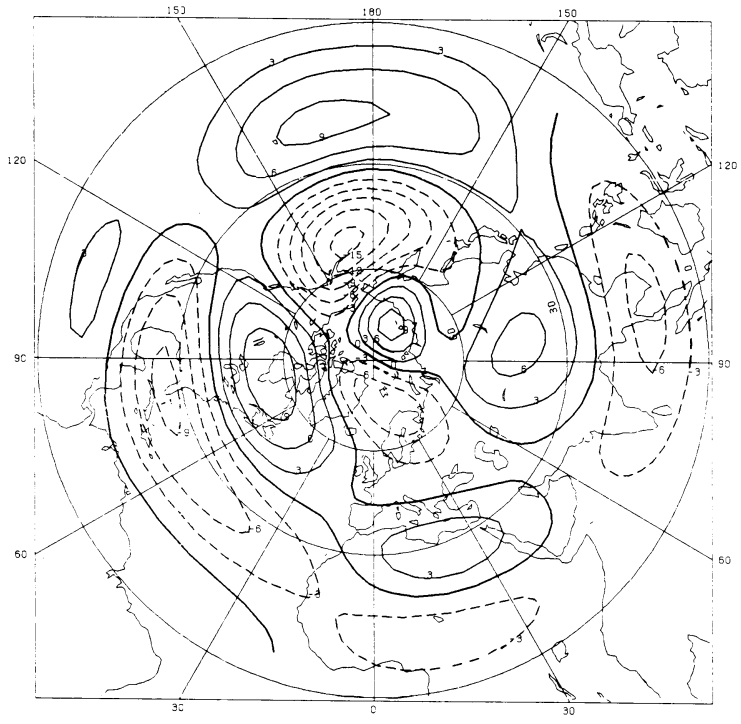

Fig. 6. Normalized anomalous streamfunction pattern of the computed steady state I at $\alpha = 0.5$. The contour interval is 3.10^{-6} $m^2 s^{-1}$.

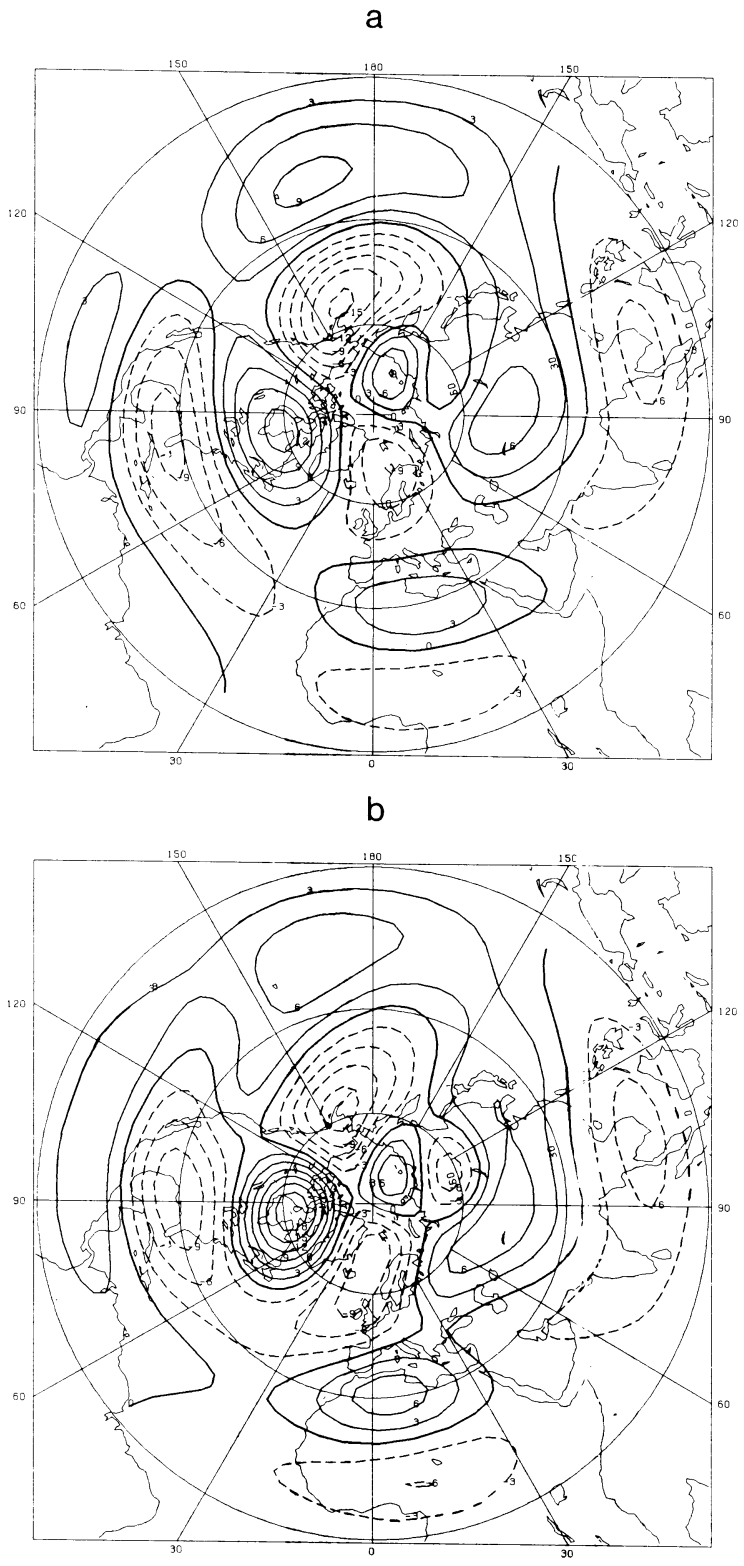

Fig. 7. As Fig. 6, but now of state II (a) and IV (b) at α = 0.65.

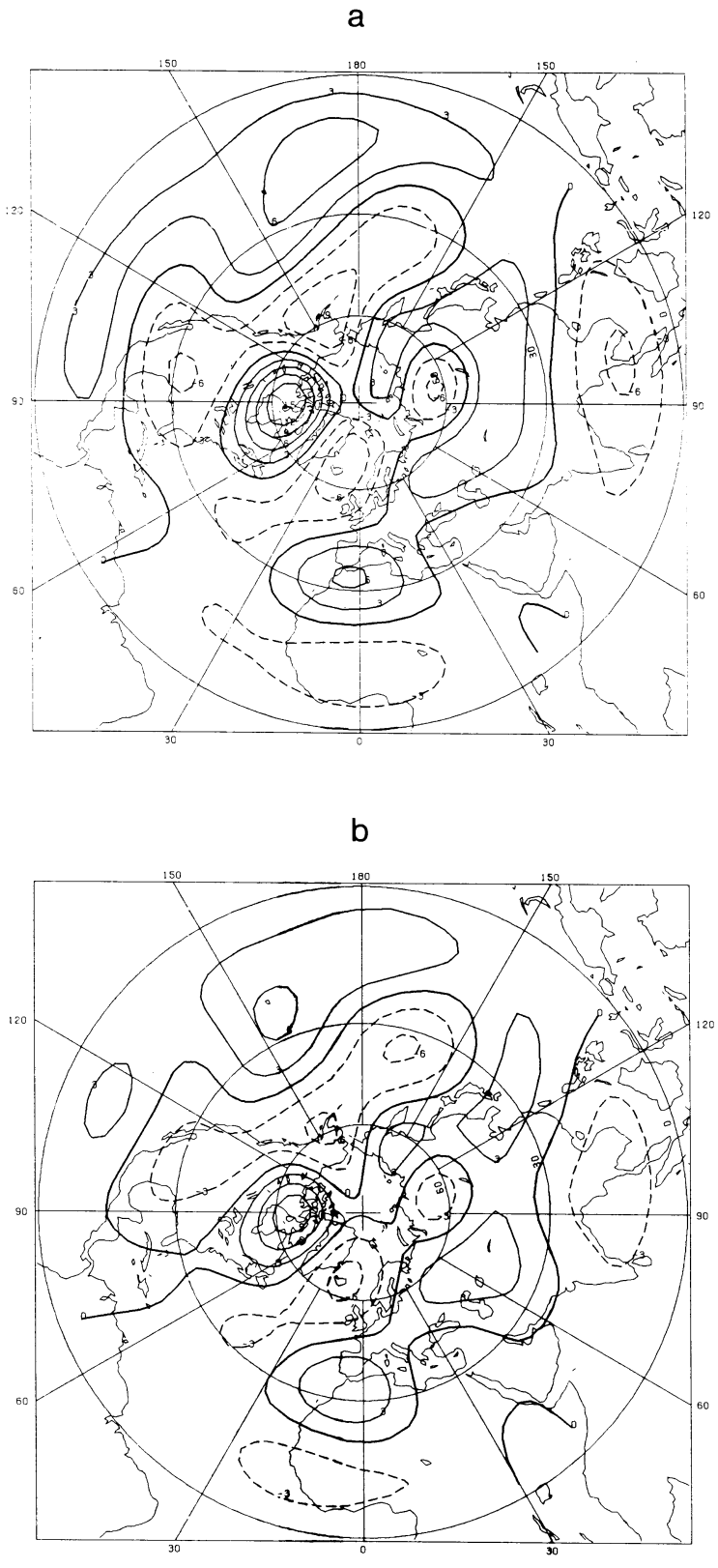

Fig. 8. As Fig. 6, but now of state V at α = 1.0 (a) and state VI at α = 1.5 (b) on the main branch.

same. The pcc is 0.58, which is approximately the same as for the linear wavy basic-state response (0.59).

The normalized anomalous streamfunction patterns of the steady states at $\alpha = 0.65$ before and after the fold, indicated by II and IV in Fig. 5, are shown in Fig. 7a and b respectively. The anomaly pattern of state II is still very similar to the linear response. The anomaly pattern of state IV on the other hand, displays significant differences. The most noteworthy changes are the strong intensification of the anticyclone over Eastern Canada and the weakening of the dipole over the Pacific. This pattern shows less correspondence with the observations. The latter fact is reflected by a drop in th pcc from 0.51 for state II to 0.29 for state IV. The anomaly pattern of state III (not shown) is not very different from that of state IV. It displays qualitatively the same changes with respect to state II. The pcc with the observed pattern is 0.39.

An increase in α after the second saddle-node bifurcation (B) decreases the amplitude of the normalized anomalies. This occurs because the anomalies themselves saturate for increasing α. Inspection of the total streamfunction patterns of the steady states reveals that the saturation of the response after the second saddle-node bifurcation is a consequence of two effects. Increasing α results in a northward displacement of the zero wind line and a strengthening of the easterly flow in the areas of strongest forcing. In addition, due to the change in $\hat{\zeta}$, the strength of the anomalous forcing $(\hat{\zeta} + \zeta_c + f)\hat{D}$ becomes slightly weaker for increasing α. The saturation of the solution is clearly seen in Fig. 8a and b showing the normalized responses for $\alpha = 1.0$ and 1.5 respectively. Without significant changes in structure, the normalized response decreases for increasing α.

Figure 9 displays the anomalous response associated with $\alpha = 1$ on the upper part of the isolated branch. This is indicated by VII in Fig. 5. It is immediately clear that this response is unrealistic, because it displays very large amplitudes. All steady states on the upper as well as the lower part of the isolated branch display this behavior. The large amplitudes are caused by the disappearance of the tropical easterly winds. This facilitates energy transport into higher latitudes. Also, due to the difference in $\hat{\zeta}$, the amplitude of the anomalous forcing is three times as large as the anomalous forcing on the main branch.

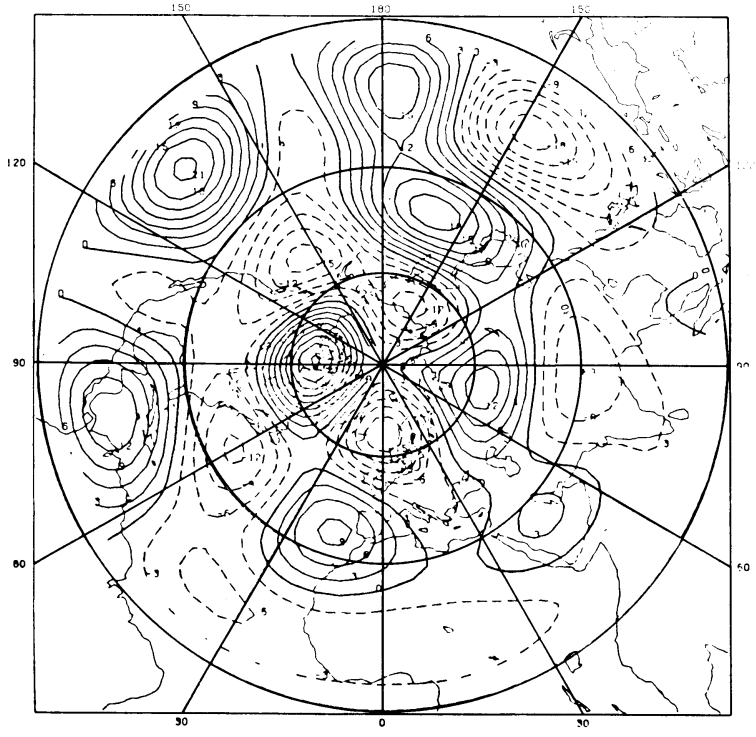

Fig. 9. As Fig. 6, but now of state VII at α = 1.0 on the upper part of the isolated branch.

5. Time integrations

In order to investigate the relation between the time-dependent behavior of the model and the computed steady states, we performed time integrations of (4) for several values of α. For time stepping we used a simple leap-frog scheme with a time step of 1 hour. In all experiments we allowed a spin up time of two years.

One way of measuring how the system evolves in time, is to compute the speed of the phase point of the model. The position of the phase point is given by the spherical harmonic coefficients of the relative vorticity. The speed of the phase point is estimated from the positions of the phase point at successive days.

Time integrations for α between the first and second Hopf bifurcation (P and Q in Fig. 5) demonstrate the existence of a stable limit cycle. The period of these limit cycles is 32 days, which is approximately the same as the period of the growing perturbations. Quasi-periodic behavior is observed after the second Hopf bifurcation. The phase point now spiralizes in a torus. This quasi-periodic behavior is clearly demonstrated by Fig. 10 which displays for $\alpha = 0.5$, just after the second Hopf bifurcation, the modulus of the speed of the phase point as well as the distance to the computed steady state. Both are shown as a function of time for a three-year time integration. Two dominant periods can be discerned with periods of approximately 34 and 170 days respectively. The first period is almost equal to the period of 33 days of the fastest growing perturbation. However, the second period does not bear a clear relationship to the period of 101 days of the second growing perturbation.

The time evolution of the projection of the phase point on the ζ_9^4 component, is shown in Fig. 11. It shows the dominant period of 34 days in which the phase point moves around the steady state, indicated by a dot, on which a weak oscillation with a longer time scale is superimposed. Inspection of daily and time-mean streamfunction patterns (not shown) reveals that the system remains in the neighborhood of the computed steady-state. The anomalous steady-state and time-mean pattern are nearly the same. The only noteworthy difference is the diminishing of the amplitude of the cyclone over the North Pacific with about 40%.

For $\alpha = 0.65$, five steady states exist simultaneously. Three of these states are situated on the main branch, the other two on the isolated

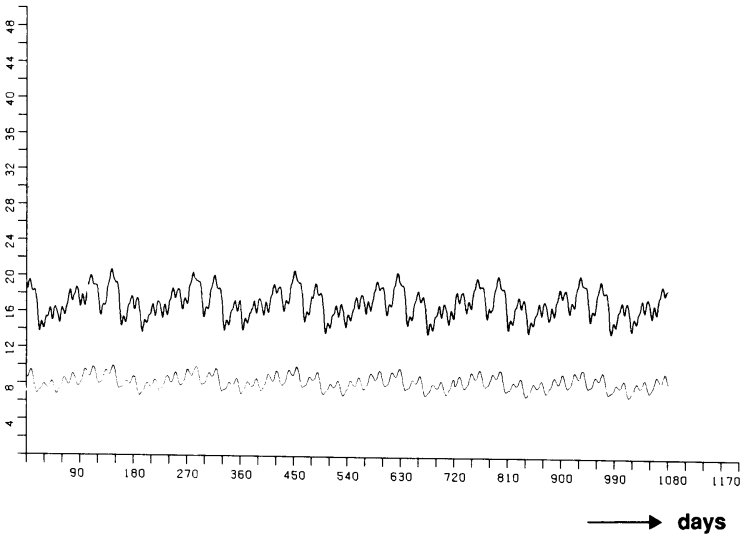

Fig. 10. Time integrations for $\alpha = 0.50$, showing the speed of the phase point (thick line) and the distances of the phase point to state I (thin line). The scale on the vertical axis is arbitrary.

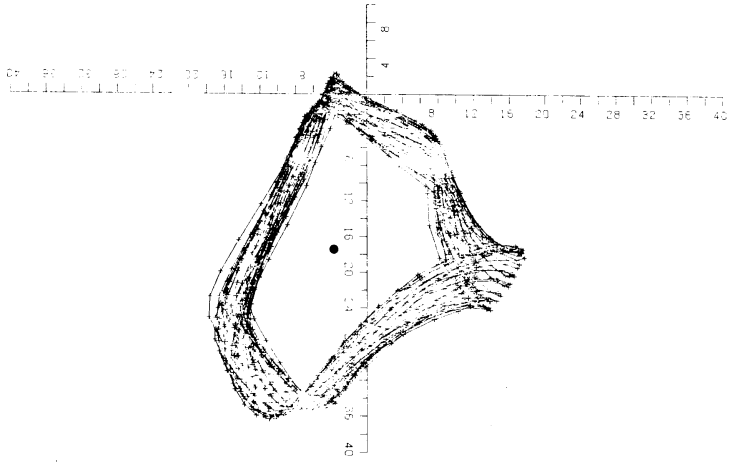

Fig. 11. Time integrations for $\alpha = 0.50$, showing the projection of the phase point on the ζ_9^4 component. The small crosses mark successive days. The computed steady state I is indicated by a dot.

branch (Fig. 5). One state, indicated by II in Fig. 5, possesses four eigenvalues with a positive real part, the other states more than five. Time integrations for $\alpha = 0.65$ starting from different points in phase space all display chaotic behavior. This is illustrated in Fig. 12 which shows the modulus of the speed of the phase point for a time series started close to state IV. The signal is dominated by large fluctuations with a characteristic time scale in the order of 30 days. These fluctuations are superimposed on variations with a longer time scale of about a year. Figure 12 also displays the distances of the phase point to states II and IV on the main branch. Both curves exhibit similar behavior. These two curves are strongly correlated with the speed of the phase point, with correlation coefficients of 0.57 and 0.48 respectively. The reason for this strong correlation is that the speed slows down when the phase point moves in the direction of the steady state along the stable manifold. Close to the steady state, the phase point is rejected along the unstable manifold increasing the speed of the phase point. The distances to the states on the isolated branch (not shown) are almost a factor of 2 larger than the distances to the states on the main branch, and are poorly correlated with the speed of the phase point, with correlations of 0.09 and 0.08 for the upper and lower state respectively. These results do not depend on the starting point in phase space. Also, time integrations starting close to one of the states on the isolated branch display the same behavior. The conclusion must be that for this value of α the states on the isolated branch are unimportant for the dynamical properties of the model, but that the dynamics is heavily influenced by the unstable steady states II, III and IV on the main branch.

Although for certain days the anomalous streamfunction patterns deviate quite strongly from those of the computed steady states on the main branch, the pattern of the normalized three-year time-mean response, shown in Fig. 13, is very similar to the patterns on the main branch, although the intensity of the time-mean circulation is less. The cyclones over the North Pacific and Mexico are about 30% weaker, while the large amplitude of the anticyclone over Eastern Canada is strongly reduced with a factor of two compared to state II. The anomaly pattern of the three-year time mean shows a better agreement with the response pattern of state II (before the fold) than with the response pattern of state IV (after the fold). The pcc's between the anomalous time-mean pattern and the steady-state responses are 0.91 and 0.81 respectively. The pcc between the anomalous time-mean and

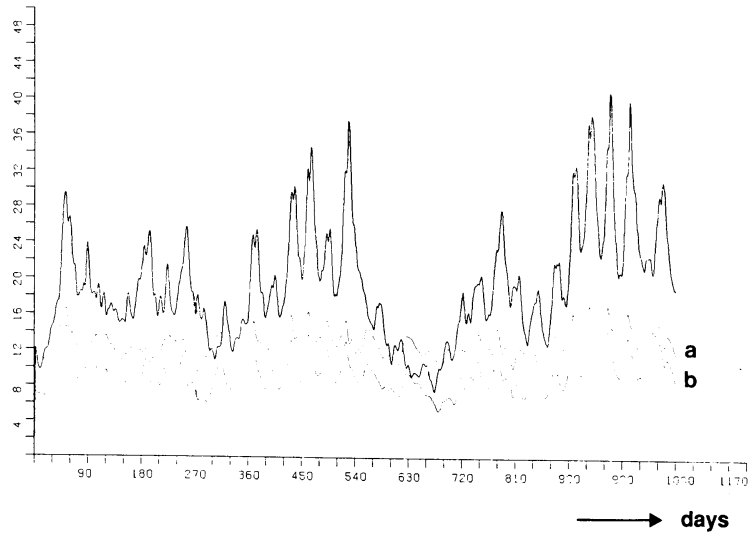

Fig. 12. As Fig. 10, but now for $\alpha = 0.65$. The distances are to state II curve (a) and state IV curve (b).

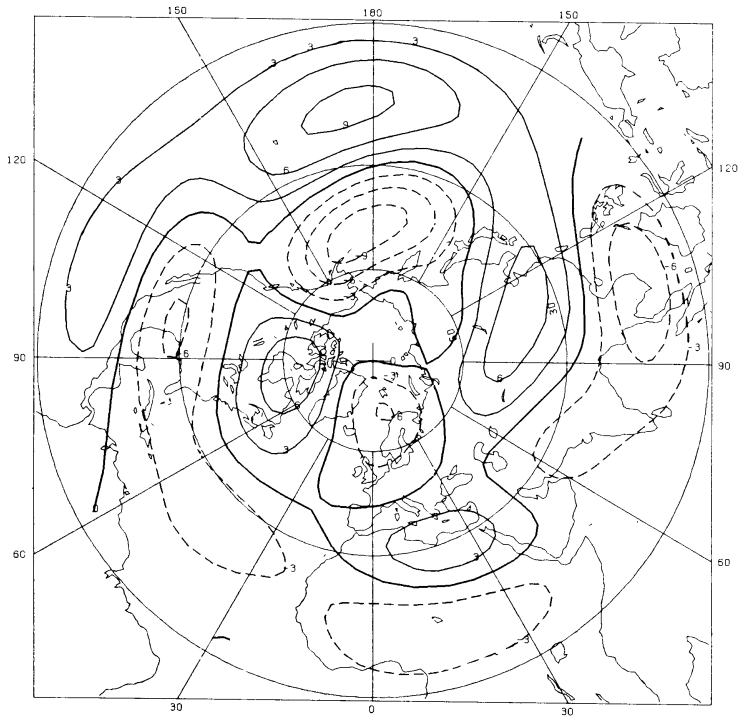

Fig. 13. Anomalous normalized time-mean streamfunction pattern of a three year time integration at $\alpha = 0.65$.

observed pattern is 0.53, which is approximately the same as the pcc for the response pattern of state II (0.52).

Time integrations were also performed for $\alpha = 1.0$, for which there exist three states simulatneously, one at the main branch and two at the isolated branch. These are indicated by V, VII and VIII in Fig. 5. All states possess more than five eigenvalues with a positive real part. Compared with the time integrations for $\alpha = 0.65$, the speed of the phase point, shown in Fig. 14, is correlated less with the distance to the main branch (state V). The correlation coefficient is 0.45. However, the correlations with the distances to the states on the isolated branch have increased, with correlation coefficients of 0.30 and 0.31 for states VII and VIII respectively.

Inspection of daily streamfunction patterns (not shown) reveals that for most days the amplitudes of the patterns are much larger than for $\alpha = 0.65$. The amplitudes are comparable to those of the steady states on the isolated branch. Also, for most days the easterlies have completely disappeared. The structure of the daily streamfunction patterns is often quite similar to the patterns of the states on the isolated branch. The correspondence between the daily streamfunction patterns and that of the state on the main branch is rather low. Compared with $\alpha = 0.65$ the variability of the streamfunction patterns is larger. The normalized anomalous time-mean pattern is shown in Fig. 15. Comparison with the anomaly patterns (Figs. 8a and 9) reveals that due to the large variability the anomaly pattern of the time mean is somewhat less intense than the response patterns of states VII and VIII on the isolated branch or the anomaly patterns on individual days, but that the amplitude is still much larger than for the response pattern of state V on the main branch. The anomalous time-mean pattern is a mixture of features of the different response patterns. For instance for the area between the date line and 30°W there is some agreement with the steady states on the main branch, whereas the strong dipole around 150°E agrees well with the solution on the isolated branch. The correspondence, as measured by the pcc, is larger for the states on the isolated branch (0.68 and 0.70), than for the state on the main branch (0.40). The pcc of the time mean with respect to the observed pattern is rather low (0.23).

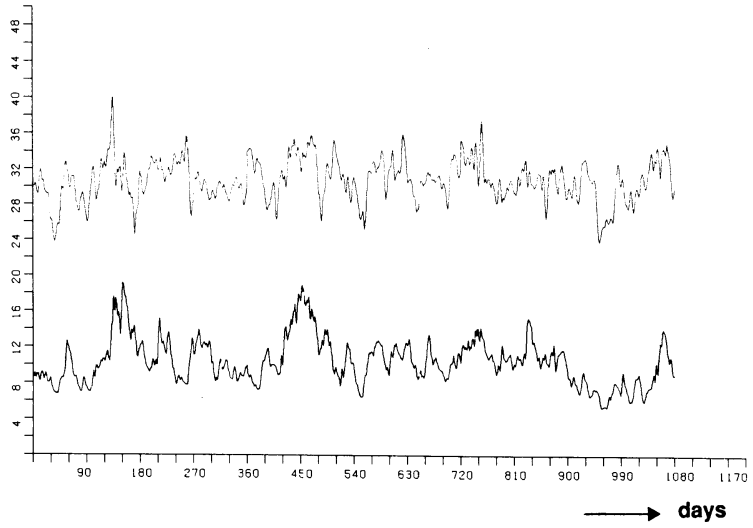

Fig. 14. As Fig. 10, but now for α = 1.0. Shown are the distances to state V on the main branch.

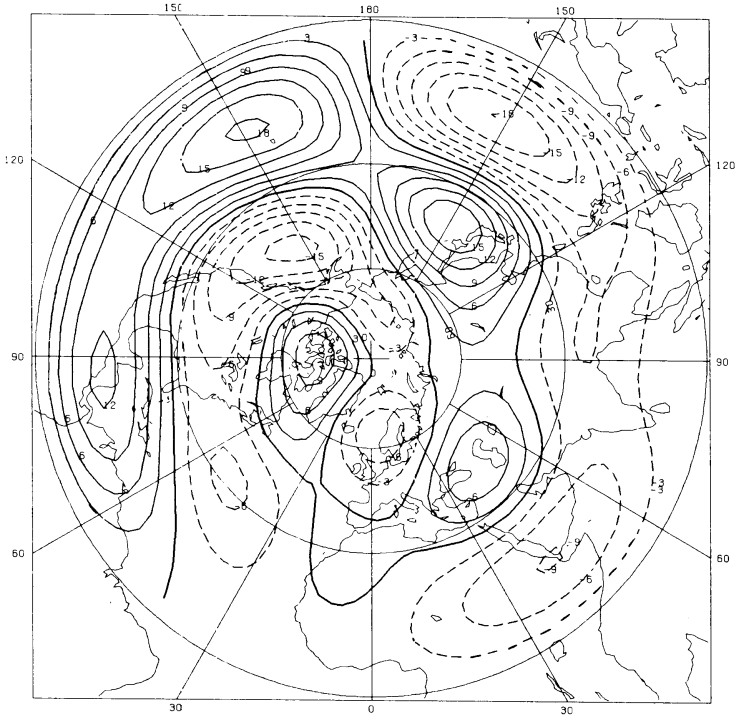

Fig. 15. As Fig. 13, but now for α = 1.0.

From these considerations we must conclude that for $\alpha = 1.0$ both the solutions on the isolated branch and on the main branch are important for the dynamics of the system.

It appears that the time mean resembles the average of the two different solutions well and that the speed of the phase point is highly correlated with the distance to the time mean with a correlation coefficient of 0.62. It is possible that the system vacillates in a complicated way between the two branches of the solution. Another possibility is that there exists an unstable limit cycle close to the time mean that has a large influence on the topological structure of the attractor.

Summarizing this section we state that for $\alpha < 0.65$ the steady-state response patterns dominate the time-mean patterns of the integrations. For larger values of α, in the fully chaotic domain, the steady states still have a large influence on the dynamics of the system. For increasing α the influence of the states on the isolated branch becomes larger relative to the states on the main branch. Consequently time mean as well as instantaneous streamfunction patterns show less agreement with the observed mean winter circulation.

6. Simplified forcing

In order to gain some insight into the importance of the circulation dependent part of the anomalous forcing in (4)

$$\hat{\zeta D} = (\zeta_c + \hat{\zeta})\hat{D}, \tag{9}$$

we computed the steady states with $\hat{\zeta D}$ neglected. For convenience we will call this experiment B and the experiment with the $\hat{\zeta D}$ term included will be referred to as A.

As already mentioned in section 4, omission of the $\zeta_c \hat{D}$ term in the forcing makes the amplitude about one and a half times larger, whereas the structure remains relatively unaffected. Consequently the linear steady-state response has increased by the same amount, without significant changes in structure.

Similarly as Fig. 5, Fig. 16 shows the projection of the computed steady states on the ζ_6^0 component for experiment B. The steady states were

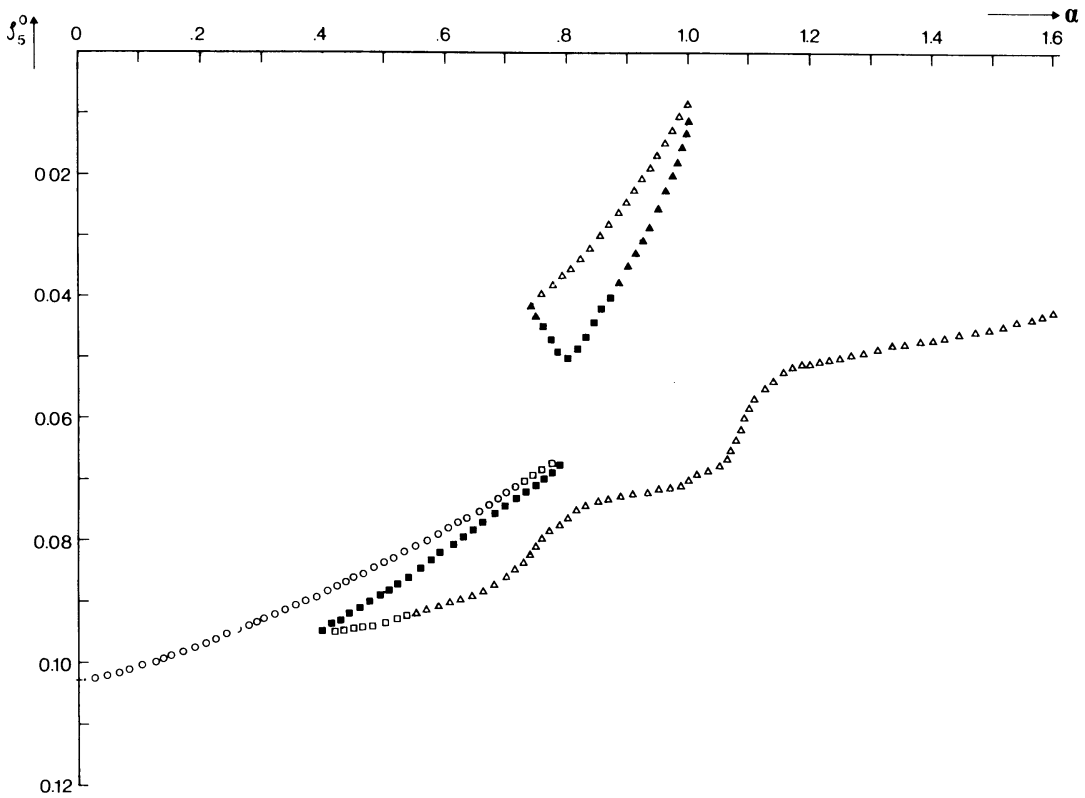

Fig. 16. As Fig. 5, but now for only the solution independent part of the forcing: $-\hat{fD}$.

computed again for α between 0 and 1.5. Comparison with Fig. 5 reveals that the fold in the main branch is much more extensive, which results in multiple steady states for α between 0.40 and 0.79. The shape of the isolated branch has changed and covers a smaller interval of α ranging from 0.74 to 1.00. Similarly as in A the number of eigenvalues with positive real part increases for increasing α.

Comparison of the anomalous streamfunction patterns of experiments A and B shows that up to $\alpha = 0.4$, before the occurrence of multiple steady states, the only important difference is in the amplitude of the pattern. It has increased by a factor of about one and a half. This is caused by the absence of the $\zeta_c \hat{D}$ term, which counteracts $f\hat{D}$ at low latitudes. Below this value of α the contribution of $\hat{\zeta}\hat{D}$ is small. The differences between the response patterns of the steady states just before and after the fold are also qualitatively the same in both experiments. In both cases the most striking feature is the intensification of the anticyclone over Eastern Canada after the fold, together with a westward shift of the dipole over the Pacific.

Figure 17a displays the anomalous normalized streamfunction patterns on the main branch after the fold for $\alpha = 0.65$. Comparison of Fig. 17a with Fig. 7b, which shows the response at $\alpha = 0.65$ for experiment A, reveals that apart from differences in amplitude the responses are still similar. Significant changes due to the $\hat{\zeta}\hat{D}$ term occur when α is further increased after the fold. In contrast to the results in A the response for $\alpha = 1.0$ (Fig. 17b) displays significant differences with the one for $\alpha = 0.65$, showing no sign of saturation yet. Most important are the increased amplitude of the anticyclone east of the date line and the dipole at 120°E. The norhtward displacement of the zero wind line, responsible for the saturation when $\hat{\zeta}\hat{D}$ is included, is absent here. There is even an opposite effect that for increasing α more of the forcing is located in the westerlies. Saturation is now observed for larger values of α. This is demonstrated by Fig. 17c, showing the rescaled response for $\alpha = 1.5$. Compared with the response for $\alpha = 1.0$ its amplitude has decreased by about a factor of one and a half, without large changes in structure.

Like in experiment A, the easterlies disappear for the states on the isolated branch. However the differences in the amplitude with respect to the states on the main branch are much less now. In A the forcing on the isolated branch is a factor of three stronger than the forcing on the main

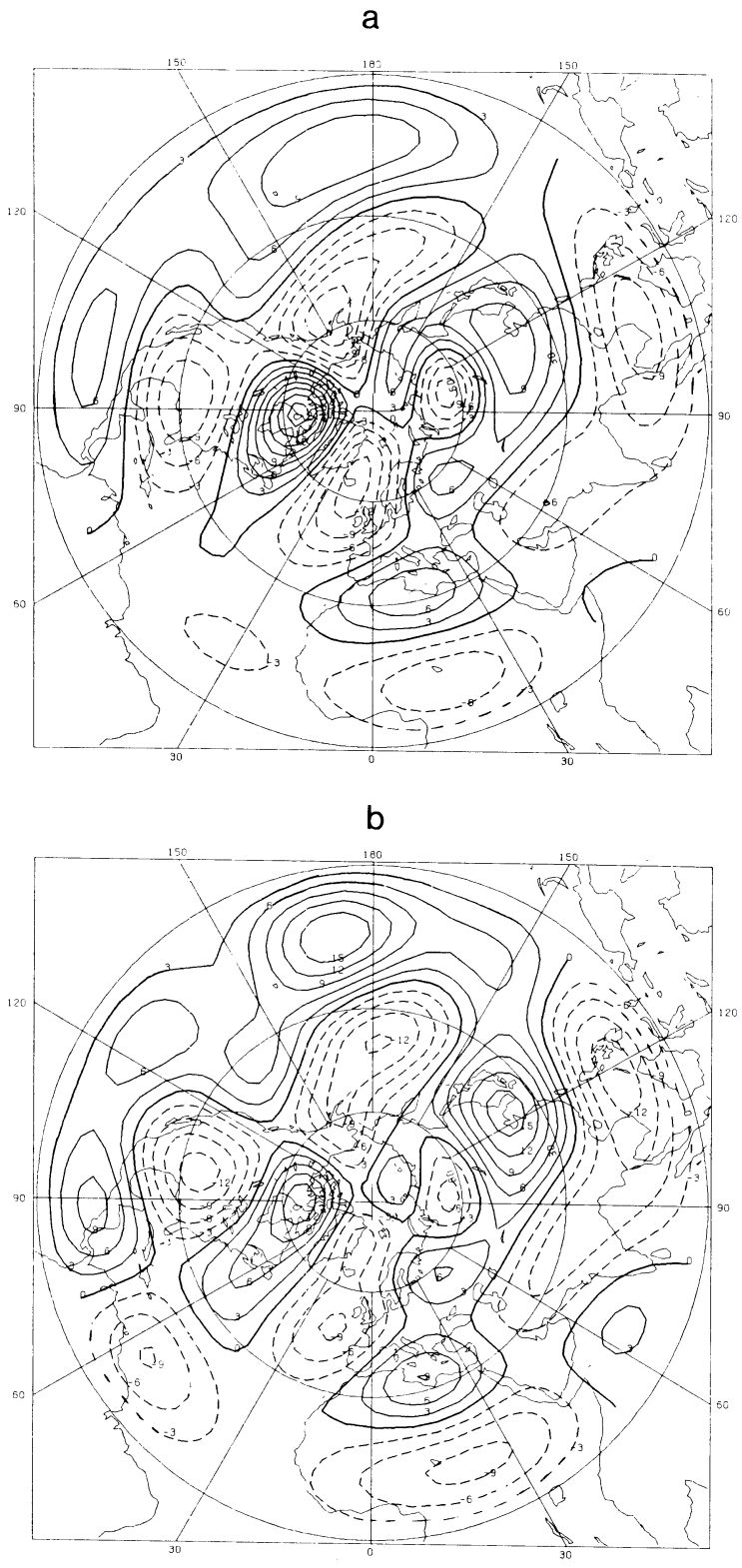

Fig. 17. Anomalous normalized streamfunction pattern of the steady states at the main branch in Fig. 16 for α = 0.65 (a), α = 1.0 (b) and α = 1.5 (c).

C

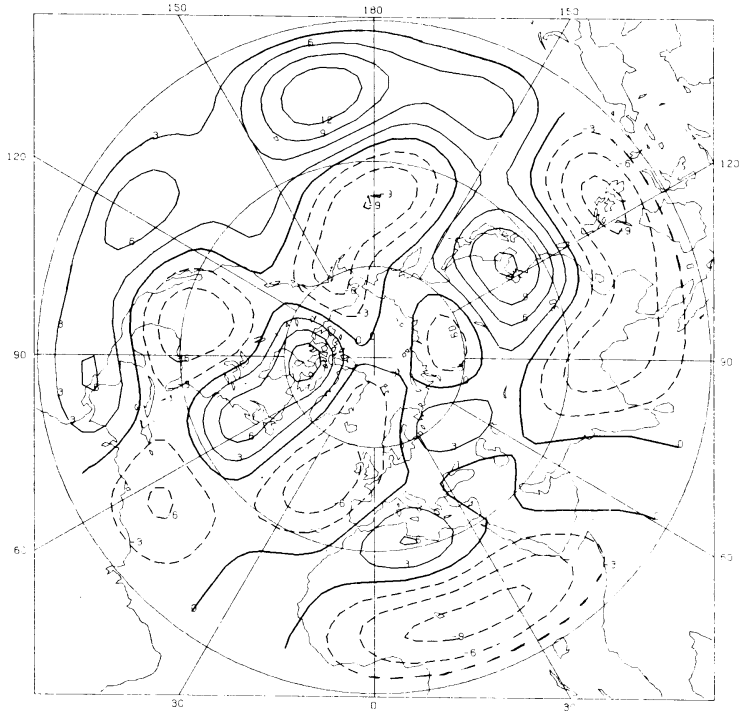

Fig. 17 (Continued)

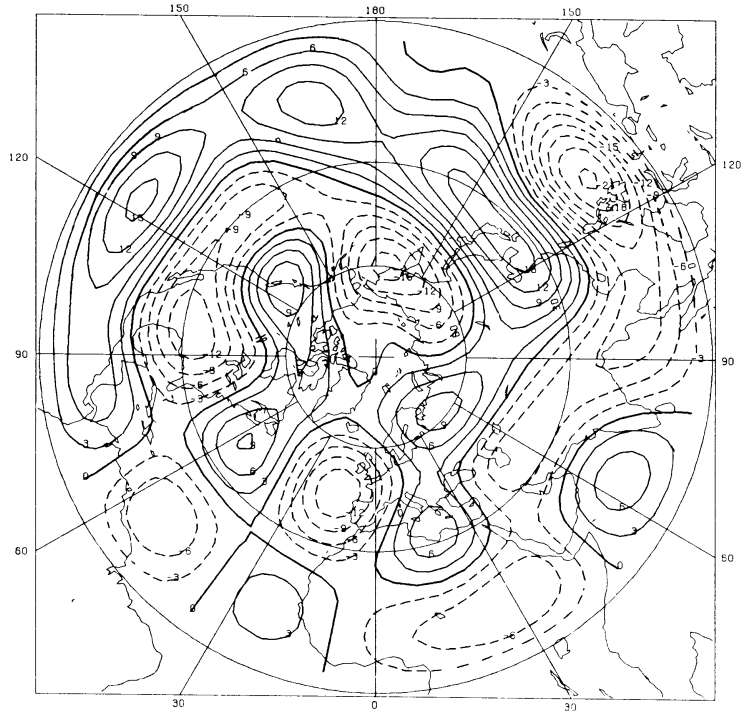

Fig. 18. As Fig. 17, but now for α = 1.0 at the isolated branch.

branch. This is due to the solution dependent part of the forcing ($\hat{\zeta}\hat{D}$). In contrast to the results in A the streamfunction patterns of the states on the isolated branch still have some resemblance to the states on the main branch after the fold. This is revealed by Fig. 18 showing the streamfunction pattern of the upper part of the isolated branch for $\alpha = 1.0$. The states on the upper and lower part of the isolated branch are again very similar to each other.

For several values of α we performed time integrations without the $\hat{\zeta}\hat{D}$ term in the forcing. For values of α below 0.4 all time integrations converge to a stable limit cycle. Between $\alpha = 0.40$ and 0.70, for which the main branch displays a fold, time integrations display chaotic ($\alpha = 0.55$) as well as periodic behavior ($\alpha = 0.70$). Just like in A, the steady states have a large influence on the dynamics of the system.

In order to investigate the effect of the isolated branch, we also performed time integrations for $\alpha = 0.90$, which is about halfway the isolated branch. The streamfunction patterns of the steady states for this value of α are only slightly different from the ones for $\alpha = 1.0$, displayed in Fig. 17b and 18 respectively. All three steady states, two at the isolated branch and one at the main branch, possess five or more positive real eigenvalues. As expected the time integrations display complete chaotic behavior. The speed of the phase point, displaying large variations, is now strongly correlated with the distance to the steady states on the isolated branch, with a correlation coefficient of 0.79, whereas the correlation with the steady state at the main branch is almost zero. This is in contrast to the results in A. In A the correlations of the speed of the phase point with the main and isolated branch are approximately 0.4 and 0.3 respectively (section 5). Due to the strong dominance of the isolated branch the time-mean pattern (not shown) is very similar to the states on the isolated branch.

Summarizing this section we have found that for small values of α the neglect of the $\hat{\zeta}\hat{D}$ term results in steady states that have a structure similar to those in experiment A. For larger values of α, when the $\hat{\zeta}\hat{D}$ term becomes important, significant differences occur both with respect to the steady-states as well as the time dependent behavior.

7. Strong friction

One of the results of the foregoing sections, is that the nonlinear terms do not improve the agreement with the observations. For $\alpha < 0.65$ the pattern correlations are more or less the same as for the linear response. For larger values of α, after the fold in the steady state curve, the agreement of both the steady-state response patterns and the anomalous time-mean patterns with the observed anomaly pattern becomes less, as revealed by a decrease in the pcc's. A possible explanation for this result might be that for the real atmosphere α is less than 0.65, instead of being equal to one. Another possible explanation is that the damping time scale is too large. The choice for ε (20 days^{-1}) was derived from the assumption of a marginally basic state. This assumption leads to a large dissipation time scale. This damping time scale may be physically unrealistic for instantaneous flows but may be appropriate for statistical time-mean flows. However, given the uncertainty in the strength of the Rayleigh friction we have investigated the sensitivity of the results to an increase in this parameter.

We computed the steady-state curve for ε = 10 days^{-1}. For this stronger Rayleigh friction the steady-state curve displays no folds, nor an isolated branch. Up to α = 1.1, for which a Hopf bifurcation occurs, all steady states are stable. New bifurcations are not observed for α between 1.1 and 1.5. Time integrations converge to the stable steady states for $\alpha < 1.1$ and result in a stable limit cycle for $\alpha > 1.1$, with a close correspondence between the time mean and the computed steady states.

The linear normalized response, shown in Fig. 19, displays a slight decrease in the amplitude over the forcing area (compare with Fig. 4b) together with a small eastward displacement of the highs and lows. Away from the forcing regions, the amplitude of the response is drastically reduced, for certain areas such as the North Atlantic by a factor of three. The pcc with the observed pattern shows a small increment from 0.59 to 0.63.

The nonlinear normalized responses for α = 1.0 and 1.5 are displayed in Fig. 20a and b respectively. The response for α = 1.0 displays only minor differences with the linear response, the most important ones being the increase response away from the forcing region. The contribution of the nonlinear terms is more significant for α = 1.5 as shown in Fig. 20b. Important differences are the intensification of the anticyclone east of the date

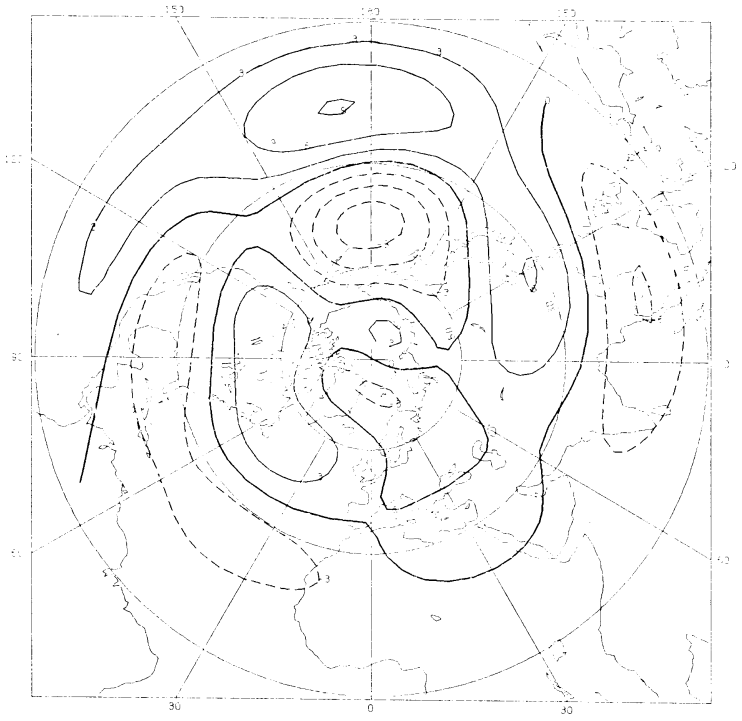

Fig. 19. As Fig. 4b, but now for $\varepsilon = 10$ days^{-1}.

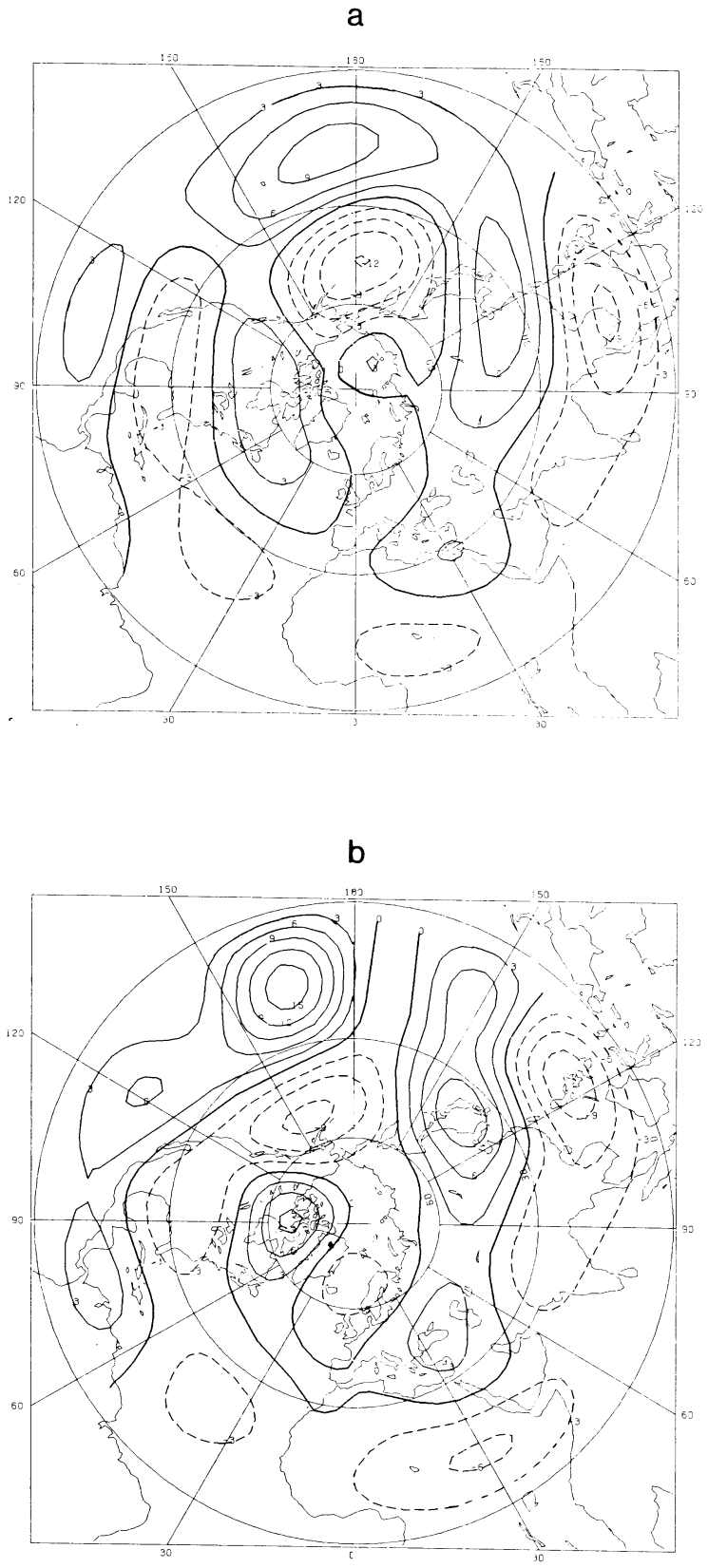

Fig. 20. Anomalous normalized streamfunction patterns of the computed steady states for $\varepsilon = 10$ days^{-1} at $\alpha = 1.0$ (a) and $\alpha = 1.5$ (b).

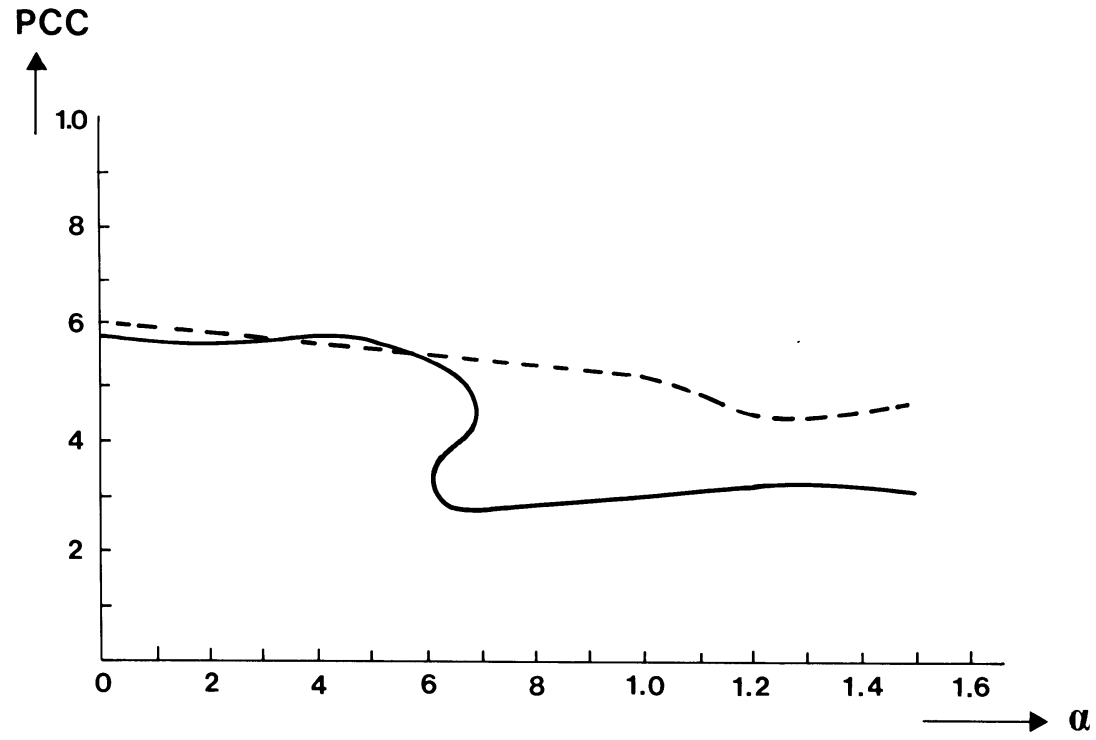

Fig. 21. Pattern correlations of the computed anomalous normalized streamfunction patterns with the observed 400 mb streamfunction for ε = 20 days^{-1} (solid line) and ε = 10 days^{-1} (dashed line) as a function of α.

line and the pattern change over eastern Canada and the North Atlantic. In contrast to the case for $\varepsilon = 20$ days^{-1} the nonlinear response does not show saturation nor a sharp drop in the pcc for increasing α. The latter fact is demonstrated in Fig. 21 which displays the pcc's of the response patterns with the observed 400 mb streamfunction pattern as a function of α for ε equal to 10 and 20 days^{-1} respectively. As mentioned in section 4 the pcc shows a sharp drop around $\alpha = 0.65$ for $\varepsilon = 20$ days^{-1}. This drop is connected to the fold in the steady state curve. The pcc for $\varepsilon = 10$ days^{-1} displays only a gradual decrease from 0.63 for the linear response to 0.53 for $\alpha = 1$. The drop in the pcc after this value of α to about 0.45, is much less dramatic and occurs for larger values of α than the drop in the pcc for $\varepsilon = 20$ days^{-1}.

Although the sharp decrease in the pcc is absent for $\varepsilon = 10$ days^{-1}, the pcc still displays a gradual decrease for increasing α. The fact that for both values of ε the responses for small α give the best results suggest that the real forcing was significantly smaller than estimated, making the nonlinear terms relatively unimportant.

8. Conclusions and discussion

In this paper we have investigated the nonlinear steady-state response of a barotropic model to an estimate of the observed anomalous tropical divergence forcing for the El-Niño winter of 1982/83. The 400 mb climatological flow was made a forced solution of the model by means of a relaxation forcing. The Rayleigh friction coefficient was chosen such that this solution is marginally stable. Using the pseudo-arclength method of Keller (1978) we computed the steady states as a function of a dimensionless parameter α, governing the strength of the anomalous forcing. For $\alpha \ll 1$ the response is linear, whereas for $\alpha = 1$ we end up with the complete nonlinear response. The computed steady-state curve deviates markedly from a straight line and displays a fold for α between 0.60 and 0.69. In addition there exists and isolated branch for α between 0.59 and 1.23. All the computed steady states turned out to be unstable. In general the number of growing perturbations increases for increasing strength of the anomalous forcing.

The normalized anomalous streamfunction pattern for $\alpha = 10^{-5}$, i.e. the linear response, compares well with the observed pattern, with a pcc of

0.59. The wave components in the basic state make a large contribution to the linear response. This agrees with the results of Branstator (1985).

Before the fold in the steady-state curve the nonlinear responses are very similar to the linear one. The response patterns of the states after the fold display large differences with the linear response. The agreement between the anomalous streamfunction patterns and the observed anomaly pattern is smaller after the fold. This is revealed by a drop in the pcc from 0.6 to about 0.3. After the fold, a further increase in α results in saturation of the response. This saturation is related to the northward shift of the zero-wind line in the region of strong forcing. The streamfunction patterns of the isolated branch display unrealistically large amplitudes. For these solutions the easterlies in the zonal mean are absent and the forcing is a factor of three stronger than the forcing of the corresponding solution on the main branch.

Time integrations for values of α smaller than 0.65 show that the steady states on the main branch strongly influence the time-mean pattern of the model despite the unstable nature of these solutions. Periodic, quasi-periodic and complete chaotic behavior are all three observed. After the emergence of the isolated branch the states on the main and those on the isolated branch both have an impact on the time-dependent behavior. The instantaneous patterns show large amplitudes, similar to those of the states on the isolated branch. The time-mean patterns show some correspondence with the states on the isolated as well as on the main branch.

In order to investigate the influence of the solution-dependent part of the forcing ($\hat{\zeta D}$) on the steady-state response patterns, we computed the steady states also without this term. The forcing is now only linearly dependent on α. The computed steady-state curve displays qualitatively the same behavior, including a fold and an isolated branch. The anomalous streamfunction patterns for the steady states on the main branch up to $\alpha \simeq 0.65$ after the fold are very similar to the ones that include $\hat{\zeta D}$, except for an increase in the amplitude by a factor of about one and a half. This is caused by the absence of the $\zeta_c \hat{D}$ term which counteracts $\hat{fD}$ at low latitudes. When α is further increased the solutions become more and more different to the ones that include $\hat{\zeta D}$. Without $\hat{\zeta D}$ saturation occurs at much larger values of α. Another effect of the omission of $\hat{\zeta D}$ is that the differences between the solutions on the main and isolated branch become smaller.

Again time integrations, for values of α before the emergence of the isolated branch, display the feature that the states on the main branch strongly govern the time-mean pattern. After the emergence of this branch the time-dependent behavior is only affected by the states on the isolated branch.

The fold as well as the isolated branch disappear when the damping time scale is decreased to 10 days. Up to $\alpha = 1$ the linear and nonlinear response are very similar. Significant changes occur only for larger values of α. Like for $\varepsilon = 20$ days^{-1} the inclusion of nonlinear terms does not improve the agreement with the observed pattern. The pcc decreases gradually for increasing α, although a dramatic drop such as observed for $\varepsilon = 20$ days^{-1} does not occur.

Summarizing we conclude that for values of α before the fold in the steady-state curve the computed steady states and the time-mean patterns differ little from the linear response. After this fold, however, the effects of the nonlinearities become larger and the patterns less realistic. Although it is hard to estimate the real strength of the forcing, the results suggest that the estimated forcing ($\alpha = 1$) is too strong. It is also likely that a stronger friction than $\varepsilon = 20$ days^{-1} is more realistic. Assuming that both the forcing and the damping time scale are too large the results suggest that the atmospheric response to even a very strong El-Niño like the one in 1982/83 is approximately linear.

In agreement with the results of studies by Sardeshmukh and Held (1984), Kang and Held (1986), Hendon (1986) and Held and Kang (1987), the main effect of the nonlinearities is to slightly modify the structure and amplitude of the planetary waves, together with relatively small changes in the position of the pressure cells.

Acknowledgements

We thank our colleagues for their critical remarks and Birgit Kok for typing the manuscript.

9. References

Arkin, P.A., 1984: An examination of the Southern Oscillation in the upper tropospheric tropical and subtropical wind field. Ph.D. Thesis, Available from University of Maryland, College Park, MD 20742, U.S.A.

Bjerknes, J., 1966: A possible response of the atmospheric Hadley circulation to the equatorial anomalies of ocean temperature. Tellus, 18, 820-829.

Blackmon, M.L., J.E. Geisler and E.J. Pitcher, 1983: A general circulation model study of January climate anomaly patterns associated with interannual variation of equatorial Pacific sea surface temperatures. J. Atmos. Sci., 40, 1410-1425.

Branstator, G., 1985: Analyses of general circulation model sea-surface temperature anomaly simulations using a linear model. J. Atmos. Sci., 42, 2225-2254.

Frederiksen, J.S., 1983: A unified three-dimensional instability theory of the onset of blocking an cyclogenesis. II: Teleconnection patterns. J. Atmos. Sci., 40, 2593-2609.

Geisler, J.E., M.L. Blackmon, G.T. Bates and S. Munoz, 1985: Sensitivity of January climate response to the magnitude and position of equatorial Pacific sea surface temperature anomalies. J. Atmos. Sci., 42, 1037-1049.

Held, I.M. and Kang, I.-S., 1987: Barotropic models of the extratropical response to El-Niño. J. Atmos. Sci., 44, 3576-3586.

Hendon, H.H., 1986: The time-mean flow and variability in a nonlinear model of the atmosphere with tropical diabatic forcing. J. Atmos. Sci., 43, 72-88.

Horel, J.D. and M.J. Wallace, 1981: Planetary scale atmospheric phenomena associated with the interannual variability of sea surface temperature in the equatorial Pacific. Mon. Wea. Rev., 109, 813-829.

Hoskins, B.J., and D.J. Karoly, 1981: The steady linear response of a spherical atmosphere to thermal and orographic forcing. J. Atmos. Sci., 38, 1179-1196.

Kang, I.-S., and I.M. Held, 1986: Linear and nonlinear models of stationary eddies in the upper troposphere during Northern summer. J. Atmos. Sci., 43, 3045-3057.

Kang, I., and N.-C. Lau, 1986: Principal modes of atmospheric variability in model atmosphere with and without anomalous sea surface temperature forcing in the tropical Pacific. J. Atmos. Sci., 43, 2719-2735.

Kasahara, A., and P.L. da Silva Dias, 1986: Response of planetary waves to stationary tropical heating in a global atmosphere with meridional and vertical shear. J. Atmos. Sci., 43, 1893-1911.

Keller, H.B., 1978: Global homotopies and Newton methods. Nonlinear Analysis, C. de Boor and G.H. Golub, Eds., Academic press, 73-94.

Kok, C.J. and J.D. Opsteegh, 1985: Possible causes of anomalies in seasonal mean circulation patterns during the 1982-83 El Niño event. J. Atmos. Sci., 42, 677-694.

Lau, K.M., and H. Lim, 1984: On the dynamics of equatorial forcing of climate teleconnection. J. Atmos. Sci., 41, 161-176.

Lau, K.M., and J.S. Boyle, 1987: Tropical and extratropical forcing of the large-scale circulation: A diagnostic study. Mon. Wea. Rev., 115, 400-428.

Lau, N.-C., 1981: A diagnostic study of recurrent meteorological anomalies appearing in a 15-year simulation with a GFDL general circulation model. Mon. Wea. Rev., 109, 2287-2311.

Legras, B., and M. Ghil, 1985: Persistent anomalies, blocking and variations in atmospheric predictability. J. Atmos. Sci., 42, 433-471.

Manabe, S., and D.G. Hahn, 1981: Simulation of atmospheric variability. Mon. Wea. Rev., 109, 2260-2280.

Mo, K.C., and R.E. Livezey, 1986: Tropical-extratropical geopotential height teleconnections during the northern hemispheric winter. Mon. Wea. Rev., 114, 2488-2515.

Oort, A.H., 1983: Global atmospheric circulation statistics 1958-73. NOAA Professional Paper 14, NOAA (U.S. Government Printing Office), Washington, DC 20402, 180 pp 47 microfiches.

Opsteegh, J.D., and H.M. van den Dool, 1980: Seasonal differences in the stationary response of a linearized primitive equation model: Prospects for long-range forecasting? J. Atmos. Sci., 37, 2169-2185.

Reinhold, B.B., and R.T. Pierrehumbert, 1982: Dynamics of weather regimes: Quasi-stationary waves and blocking. Mon. Wea. Rev., 110, 1105-1145.

Sardeshmukh, P.D., and I.M. Held, 1984: The vorticity balance in the upper atmosphere of a general circulation model. J. Atmos. Sci., 41, 768-778.

Sardeshmukh, P.D., and B.J. Hoskins, 1985: Vorticity balances in the tropics during the 1982-83 ENSO event. Quart. J. Roy. Meteor. Soc., 111, 261-278.

Simmons, A.J., J.M. Wallace, G.W. Branstator, 1983: Barotropic wave propagation and instability and teleconnection patterns. J. Atmos. Sci., 40, 1363-1392.

Webster, P.J., 1982: Seasonality in the local and remote atmospheric response to sea surface temperature anomalies. J. Atmos. Sci., 39, 41-52.